



TECHNISCHE
UNIVERSITÄT
WIEN
Vienna University of Technology

DISSERTATION

Oxygen Exchange Pathways of Platinum Model Electrodes on Yttria-stabilized Zirconia

ausgeführt zum Zwecke der Erlangung des akademischen Grades eines
Doktors der technischen Wissenschaften
unter der Leitung von

Univ.Prof. Dipl.-Phys. Dr. rer. nat. Jürgen Fleig
E164

Institut für Chemische Technologien und Analytik
Fachbereich Elektrochemie

eingereicht an der Technischen Universität Wien
Fakultät für Technische Chemie

von

Dipl.-Ing. Alexander Karl Opitz
0125652
Saxen 110, A-4351 Saxen

Wien, am 12. Mai 2011

Vorwort

Jetzt ist schon wieder was passiert [129]! Man glaubt's ja nicht wie schnell sowas geht, aber wenn man sich dann anschaut, wie der Stapel Papier Tag für Tag immer dicker wird, dann denkt man sich, bald ist es soweit, dass man damit einen erschlagen kann. Da ist dann auch der Punkt erreicht, wo man sich sagt, jetzt lass ich's in einen Einband picken und aufs Dekanat damit – so richtig mit Kaszettel ausfüllen, Amtschimmel und so.

Dass es überhaupt so weit kommen konnte, da hatten ja auch ein paar andere Leute die Finger im Spiel. Weil der eigentliche Sinn von so einem Vorwort ist ja nicht der, dass der Autor über Gott und die Welt sudert, sondern der, dass er sich bei denen mit den Fingern im Spiel bedankt.

Ein besonders großes Danke geht dabei an meine Gudrun, dass ich immer wenn es von „besonderer wissenschaftlicher Notwendigkeit“ ist, meine Verrücktheiten ausleben darf. (Und es ist IMMER von besonderer wissenschaftlicher Notwendigkeit!)

Außerdem möchte ich mich bei meinen Eltern bedanken, dass sie mir – obwohl ich formal ja zu den Berufstätigen gezählt werden kann – die eine oder andere Unterstützung zukommen ließen. Für ein gemeinsames entspannendes Hobby zum Kopf abschalten sei auch meinem Bruder Michael gedankt – keiner entzündet den Smoker so gut wie du ;-)

Ganz besonders bedanken möchte ich mich natürlich bei meinem Doktorvater Jürgen Fleig für die hervorragende Betreuung, für die Freiheit, den Weg meiner Arbeit selbst zu bestimmen, für die Möglichkeit zahlreicher Tagungsteilnahmen und dafür, dass seine Tür immer offen steht, wenn guter Rat teuer ist!

Danken möchte ich weiters allen, die in irgendeiner Form an der Entstehung dieser Arbeit beteiligt waren: Den Studenten und Diplomanden Adnan, B-lex, Christoph, Klaus, Michi, Philipp, Steffi, Tobi, Tobias und Tschisi für die tatkräftige Unterstützung und dafür, dass ihr nicht müde wurdet, mich mit Fragen zu löchern. Vor allem freut es

mich, dass ich einige von euch auch mit dem Stromchemie-Virus anstecken konnte. Ein riesengroßes Dankeschön geht an Prof. Hörby Hutter und Arno – tof simst! Herzlich bedanken möchte ich mich auch bei Elisabeth Eitenberger für die unzähligen REM Aufnahmen, beim Kristallographie-Team Prof. Kubel, Prof. Halwax und Frau Pantazi für das Beugen von Röntgenstrahlen, bei Andreas Steiger-Thirsfeld vom USTEM für die FIB-Schnitte und bei unserem Udo für eigentlich alles sowie für die Unterstützung am Konfokalmikroskop. Weiters möchte ich Prof. Günter Fafilek und Prof. Hermann Kronberger für spannende und hilfreiche Diskussionen sowohl elektrochemischer als auch nicht-fachlicher Natur danken.

Ein großes Danke geht auch an die gesamte Arbeitsgruppe – Andreas, Arno, B-lex, Can, Edvinas, Elmar, Gerald, Judith, Lukas, Markus, Martin, Matthias, Michele, Michi, Mr. Snoot, Philipp, Roland, Sandra, Steffi, Till, Tobi und Tschisi für das super Arbeitsklima, die vielen Diskussionen, erheiternde Kaffeerunden und dafür, dass ihr gelegentlich Pucks auf mich schießt. Vor allem meinen „Büromitinsäßen“ Markus und Tobi sei gedankt, dass ich euch jederzeit mit sämtlichen Unklarheiten elektrochemischer, physikalischer und was-sonst-auch-immer-welcher Natur quälen darf – es ist mir ein Volksfest!

Schließlich möchte ich auch Judge Kurt für seine segensreiche Schoko Lade danken und Carina dafür, dass sie die Kaffeeregentschaft mit eiserner Hand führt. Ihr habt wesentlich zur Erkenntnis beigetragen, dass der tiefere Sinn einer Doktorarbeit die Transformation von Koffein und Schokolade in geschriebenes Wort ist.

Weil man alte Traditionen ja bekanntlich pflegen soll, hab' ich mir gedacht der Beneédict bekommt – für seine „Telefonseelsorge“ – wieder eine extra Seite. Wegen zeitverzögertem Erscheinen und so; Gewohnheitsrecht sozusagen.

Leider musste ich in den Jahren, die diese Doktorarbeit in Anspruch genommen hat, auch erfahren, was es bedeutet, zwei liebe Menschen zu verlieren – meinen Großvater und meinen Schwiegervater.

Ihnen möchte ich diese Seiten widmen.

Kurzfassung

Die elektrochemische Sauerstoff-Austauschreaktion an Platinelektroden auf Yttrium-stabilisiertem Zirconiumdioxid (YSZ) ist sowohl eine hochinteressante Modellreaktion für grundlegende Untersuchungen der Elektrodenkinetik an Festkörperionenleitern, als auch von großem technologischen Interesse, da sie in einer Vielzahl an elektrochemischen System eine entscheidende Rolle spielt (z.B. in Lambda-Sonden, Hochtemperatur-Brennstoffzellen, Hochtemperatur-Elektrolysezellen oder bei der elektrochemischen Modifikation der katalytischen Aktivität von Katalysator Oberflächen). In der vorliegenden Arbeit wurde die Kinetik der Sauerstoff-Austauschreaktion mit Hilfe von geometrisch wohldefinierten, dichten Pt (111) Mikroelektroden auf YSZ (100) Einkristallen untersucht. Die Elektroden wurden durch Abscheidung dünner Pt Filme mittels Kathodenzerstäubung („sputtern“) auf dem YSZ Elektrolyt und nachfolgender Mikrostrukturierung mittels Fotolithographie hergestellt. Die elektrochemische Charakterisierung erfolgte mittels Impedanzspektroskopie, Strom-Spannungs Messungen und spannungsunterstütztem ^{18}O -Tracer-Einbau in Kombination mit Flugzeit-Sekundärionen-Massenspektrometrie (time of flight secondary ion mass spectrometry, ToF-SIMS).

Anhand von Impedanzmessungen bei hohen Temperaturen (550 – 900 °C) an Mikroelektroden unterschiedlicher Größe konnte auf einen Reaktionsmechanismus über einen Pt Oberflächenpfad mit einem ratenbestimmenden Schritt an der Dreiphasengrenze geschlossen werden. Bei niedrigeren Temperaturen (< 400 °C) hingegen konnte ein Volumenpfad durch die Pt Elektrode hindurch identifiziert werden, welcher parallel zum Oberflächenpfad abläuft. Der reziproke Polarisationswiderstand bei niedrigen Temperaturen skalierte infolgedessen mit der Elektrodenfläche. Als ratenbestimmender Schritt des Volumenpfads wurde Diffusion einer Sauerstoffspezies entlang der Pt Korngrenzen diskutiert.

Mit Hilfe von ^{18}O -Einbau in Kombination mit ToF-SIMS war es möglich die elektrochemisch aktive Zone (d.h. der Bereich, in dem Sauerstoff in YSZ eingebaut wird) abzubilden. Bei ~320 °C war die Einbauzone rahmenförmig und ihre Position und laterale Ausbreitung war von der Polarisation der Elektrode abhängig. Bei moderaten

Überspannungen wurde Sauerstoff ausschließlich unter der Pt Elektrode eingebaut, bei hoher Polarisation hingegen breitete sich die Einbauzone auch auf die freie YSZ Oberfläche aus. Darüber hinaus ließen diese Experimente einen flächenbezogenen Pfad parallel zum Oberflächenpfad vermuten. Dieser flächenbezogene Pfad wird als jener Volumenpfad angesehen, der auch in elektrochemischen Impedanzmessungen identifiziert wurde.

Mittels Gleichstrommessungen bei Temperaturen zwischen 600 und 720 °C wurde das Strom-Spannungs-Verhalten der Pt Modellelektroden im Oberflächenpfad-Regime untersucht und der dreiphasenbezogene Polarisationswiderstand bei Gleichgewichtsbedingungen konnte als Diffusionsprozess identifiziert werden. Ein möglicher Elementarprozess, der dieses Verhalten erklären könnte, wäre Diffusion von Sauerstoff durch eine Verunreinigungsphase an der Dreiphasengrenze. Bei sehr hohen kathodischen Überspannungen wurde ein weiterer Reaktionspfad parallel zum diffusionslimitierten Dreiphasenpfad beobachtet. Dessen Reaktionsrate war exponentiell von der Überspannung abhängig und als wahrscheinlichste Interpretation dieses Verhaltens wurde Stöchiometrie-Polarisation des Elektrolyten diskutiert. In diesem Falle läuft die Sauerstoffreduktion auf der YSZ-Oberfläche ab, wobei die Elektronenversorgung über den Elektrolyten ratenbestimmend ist. Darüber hinaus handelt es sich beim dreiphasenbezogenen Prozess, der in den Tracer-Experimenten abgebildet wurde, höchstwahrscheinlich ebenfalls um diesen Reaktionspfad.

Insgesamt kann somit gesagt werden, dass diese Arbeit einen substantiellen und neuen Beitrag zum tieferen Verständnis von Reaktionspfaden und Reaktionsmechanismen des Sauerstoffaustausches an Pt|YSZ leistet.

Abstract

The electrochemical oxygen exchange on yttria-stabilized zirconia (YSZ) is both a highly interesting model reaction for fundamental investigations in solid state ionics and of high technological interest due to its crucial importance in many electrochemical devices (such as lambda-sensors, solid oxide fuel cells, solid oxide electrolysis cells, electrochemically promoted surface catalysis). In the present thesis the kinetics of the oxygen exchange reaction on the system Pt | YSZ was investigated by means of geometrically well-defined, dense Pt (111) microelectrodes on YSZ (100) single crystals. The electrodes were prepared by sputter-deposition of Pt thin films onto the YSZ electrolyte and subsequent micro-patterning of the film. The electrochemical characterization of these model electrodes was performed by impedance spectroscopy, current-overpotential measurements, and voltage assisted ^{18}O tracer incorporation experiments combined with time of flight secondary ion mass spectrometry (ToF-SIMS) analysis.

Impedance measurements on differently sized microelectrodes at high temperatures (550 – 900 °C) revealed a reaction mechanism via a Pt surface path with a rate determining step at the three phase boundary (TPB). At lower temperatures (< 400 °C), however, a bulk path through the Pt electrode could be identified, which is connected in parallel to the surface path. Consequently, the polarization resistance at low temperatures was related to the area of the electrodes. The rate limiting step of the bulk path was discussed to be diffusion of an oxygen species along Pt grain boundaries.

By means of a ^{18}O tracer study in combination with ToF-SIMS analysis it was possible to visualize the electrochemically active region (i.e. where oxygen is incorporated into YSZ). At ~320 °C the incorporation zone at the TPB was shown to be frame-shaped and its position and lateral extension depended on the polarization of the electrodes. At moderate polarization the oxygen incorporation solely took place underneath the electrode whereas at high polarization the active zone also extended along the free YSZ surface. Moreover, these experiments also gave evidence for an area-related path in parallel to the surface path. It is believed that this path is identical to the bulk path which was found in low temperature impedance measurements.

In dc measurements at temperatures between 600 and 720 °C the current-overpotential characteristics of the Pt model electrodes in the surface path regime were investigated and the TPB related polarization resistance under equilibrium conditions (and moderate polarization) was shown to be caused by a diffusion process. A reasonable elementary process responsible for this behavior would be diffusion of an oxygen species through an impurity phase at the TPB. At very high cathodic polarization values a further reaction path in parallel to the diffusion limited one was identified. Its reaction rate was found to depend exponentially on the overpotential and hence the corresponding process was discussed to most likely be related to stoichiometry polarization of YSZ. In this case the oxygen reduction occurs on the YSZ surface and with a rate limiting electron supply via the YSZ electrolyte. Moreover, the TPB related process visualized in tracer experiments is believed to be attributed to this elementary process.

In summary this work significantly improved the knowledge on reaction pathways and the understanding of reaction mechanisms of oxygen exchange on Pt|YSZ.

Content

1	Introduction and Status of Research	1
1.1	Oxygen exchange kinetics and electrochemical reaction pathways	2
1.2	Platinum electrodes – research history and present relevance	5
1.3	Analysis of the TPB width	8
1.4	Goals of this thesis	12
2	Experimental	14
2.1	Sample preparation.....	14
2.1.1	High temperature deposition of Pt	14
2.1.2	Low temperature deposition of Pt	15
2.2	Electrochemical measurements.....	16
2.2.1	Two-point impedance measurements.....	16
2.2.2	Pseudo four-point impedance measurements.....	17
2.2.3	DC measurements	22
2.3	¹⁸ O tracer incorporation experiments	24
2.3.1	Experimental setup for ¹⁸ O incorporation	24
2.3.2	Two-point impedance measurements with dc bias	25
2.4	ToF-SIMS measurements	26
3	Results of Sample Characterization	27
3.1	Scanning electron microscopy.....	27
3.1.1	High temperature deposited Pt films	27
3.1.2	Low temperature deposited Pt films.....	29

3.2	X-ray Diffraction	31
3.2.1	High temperature deposited Pt films	31
3.2.2	Low temperature deposited Pt films.....	31
4	Results and Discussion of Impedance Measurements.....	35
4.1	Measurements on high temperature deposited electrodes	35
4.1.1	The bulk resistance of YSZ	37
4.1.2	Parameterization of the electrode impedance	39
4.1.3	Electrochemical interpretation of the fit parameters	47
4.2	Measurements on low temperature deposited electrodes.....	52
4.2.1	Results of Impedance Measurements	52
4.2.2	Kramers Kronig test	53
4.2.3	Parameterization	55
4.2.4	The geometry dependence of the electrode polarization resistance.....	59
4.2.5	Mechanistic discussion of oxygen exchange.....	64
5	Results and Discussion of Tracer Incorporation Experiments	74
5.1	Electrochemical experiments.....	74
5.1.1	Impedance results without dc bias.....	74
5.1.2	Impedance measurements under cathodic dc bias	75
5.1.3	Electrochemical tracer incorporation experiments	77
5.2	ToF-SIMS results	80
5.2.1	Lateral ¹⁸ O distribution and the location of the electrochemically active zone	80
5.2.2	Diffusion of the tracer in YSZ	83
5.2.3	Determination of lateral profiles from ¹⁸ O-distribution images	84
5.2.4	The width of the electrochemically active zone (“TPB width”)	87
5.2.5	Bulk path versus surface path.....	89

6	Results and Discussion of dc Measurements.....	93
6.1	Parameterization of dc data.....	93
6.2	Diffusion limited kinetics.....	97
6.3	Exponential current-voltage relationship.....	103
6.3.1	Stoichiometry polarization.....	105
6.3.2	Polarization due to charge transfer and low electron concentration in YSZ.....	107
6.4	Consequences of dc results for the CNLS-fitting of impedance spectra.....	108
6.5	Consequences of dc results on the interpretation of ¹⁸ O tracer experiments.....	114
7	Complete Picture of Reaction Paths.....	117
8	Summary of Scientific Achievements.....	119
8.1	Sample preparation and measurement techniques.....	119
8.2	Electrochemical impedance measurements.....	120
8.3	Tracer incorporation experiments.....	121
8.4	Current-overpotential characteristics.....	122
9	List of Symbols.....	124
10	List of Figures.....	127
11	List of Tables.....	136
12	References.....	137

1 Introduction and Status of Research

The mechanism of the oxygen exchange reaction $O_2 + 4 e^- \rightleftharpoons 2 O^{2-}$ on the system platinum|solid oxide electrolyte is a highly important topic in solid state electrochemistry since it plays a fundamental role in several electrochemical devices and research areas: i) In voltammetric oxygen sensors (often called lambda probes) this reaction is essential for the electrochemical equilibration of the gas phases and the oxide ion conducting electrolyte. Therefore oxygen exchange between surrounding gas and electrolyte is inevitable for the generation of the Nernst potential [1-3]. ii) In solid oxide fuel cells (SOFCs) the relatively slow kinetics of O_2 reduction can cause a substantial cathodic overpotential, which to a significant part contributes to the total polarization of a SOFC and thus limits its efficiency [4-6]. The same is true for the reverse situation of O^{2-} oxidation in solid oxide electrolysis cells (SOECs). Even though Pt is not used as a typical cathode material in such devices, a potential future application are thin film micro-SOFCs containing Pt electrodes [7, 8]. Moreover, Pt|YSZ offers an excellent model system for fundamental investigations in SOFC/SOEC research. iii) Anodic oxide ion oxidation at (noble) metal electrodes often leads to spill-over of adsorbed oxygen species across the metal surface thus causing a change of the work function of the metal. This phenomenon – usually referred to as non-faradaic electrochemical modification of catalytic activity (NEMCA) – can strongly change the catalytic properties of the metal and is a highly interesting effect in the field of surface catalysis [9-12]. (Please note: Since in equilibrium both O_2 reduction and O^{2-} oxidation occur with equal reaction rates these terms as well as the term oxygen exchange are used synonymic throughout the text. The same is true for adsorption and desorption as well as for oxygen incorporation and release.)

Accordingly, similar to aqueous electrochemistry an in-depth understanding of the reaction mechanism of oxygen reduction on Pt is a major goal of fundamental research in solid state ionics. In aqueous systems a large knowledge base has been established and many though definitely not all details of the reaction mechanism could be clarified [13-17]. On solid electrolytes, on the other hand, reaction mechanisms are still under intensive discussion.

1.1 Oxygen exchange kinetics and electrochemical reaction pathways

A significant difference between electrode reactions of (gas) molecules in aqueous and solid state electrochemistry lies within the different electrochemically active phase boundaries. In case of liquid electrolytes the relevant reaction steps (e.g. adsorption, charge transfer) are restricted to the two phase boundary between electrode and electrolyte. This is also true for gas electrodes with available three phase boundaries (TPBs) since the gas dissolves in the liquid electrolyte to become electrochemically available at the electrode surface. In solid state electrochemistry, however, the picture is somewhat more complex since not only the electrode|electrolyte interface is electrochemically relevant but also the electrode|gas two phase boundary and the TPB where O_2 , electrode, and electrolyte meet. Consequently at least three different reaction pathways for oxygen exchange between gas phase and YSZ are possible – a sketch is given in Fig. 1.

The first possible reaction path is commonly referred to as electrode surface path, since most of the electrochemically relevant elementary steps are restricted to the surface of the electrode – cf. Fig 1a. In this case the electrochemically active zone of oxygen incorporation into YSZ is generally assumed to be the TPB and its close vicinity [4, 18, 19]. Reasons for a “broadening of the TPB width” are discussed in Sec. 1.3. Owing to the very low oxygen solubility in bulk platinum of a few ppm [20] Pt|YSZ is generally assumed to be a surface path system [4, 18, 19, 21-23]. Recently reported high surface diffusion coefficients for oxygen on Pt surfaces [19] suggest that not only regions close to the TPB, but also larger parts of the Pt surface might be involved in the oxygen exchange reaction. However, this is not in contradiction to a final incorporation step close to the TPB. The rate limiting reaction step of surface path kinetics can either be an elementary step at the surface of the electrode or a process close to the TPB. Consequently the geometry dependence of the polarization resistances of such electrodes can be area related or TPB length related. Hence, a variation of the electrode geometry can give valuable information on the mechanism and the location of the rate limiting elementary step [18, 22, 24].

A modified version of the surface path – namely the electrolyte surface path (cf. Fig. 1b) – only includes processes on the electrolyte (adsorption, dissociation, ioniza-

tion, incorporation) and requires some electron conduction in the electrolyte [4, 18]. Strong indication for such an electrolyte surface path was found for BiCuVO_x electrolytes [25] as well as for stabilized ceria in reducing atmospheres [26].

The third reaction path is usually called bulk path, owing to the fact that the oxygen flux from the gas phase into the electrolyte passes the bulk of the electrode. In Fig 1c a schematic bulk path in case of mixed ionic electronic conducting (MIEC)

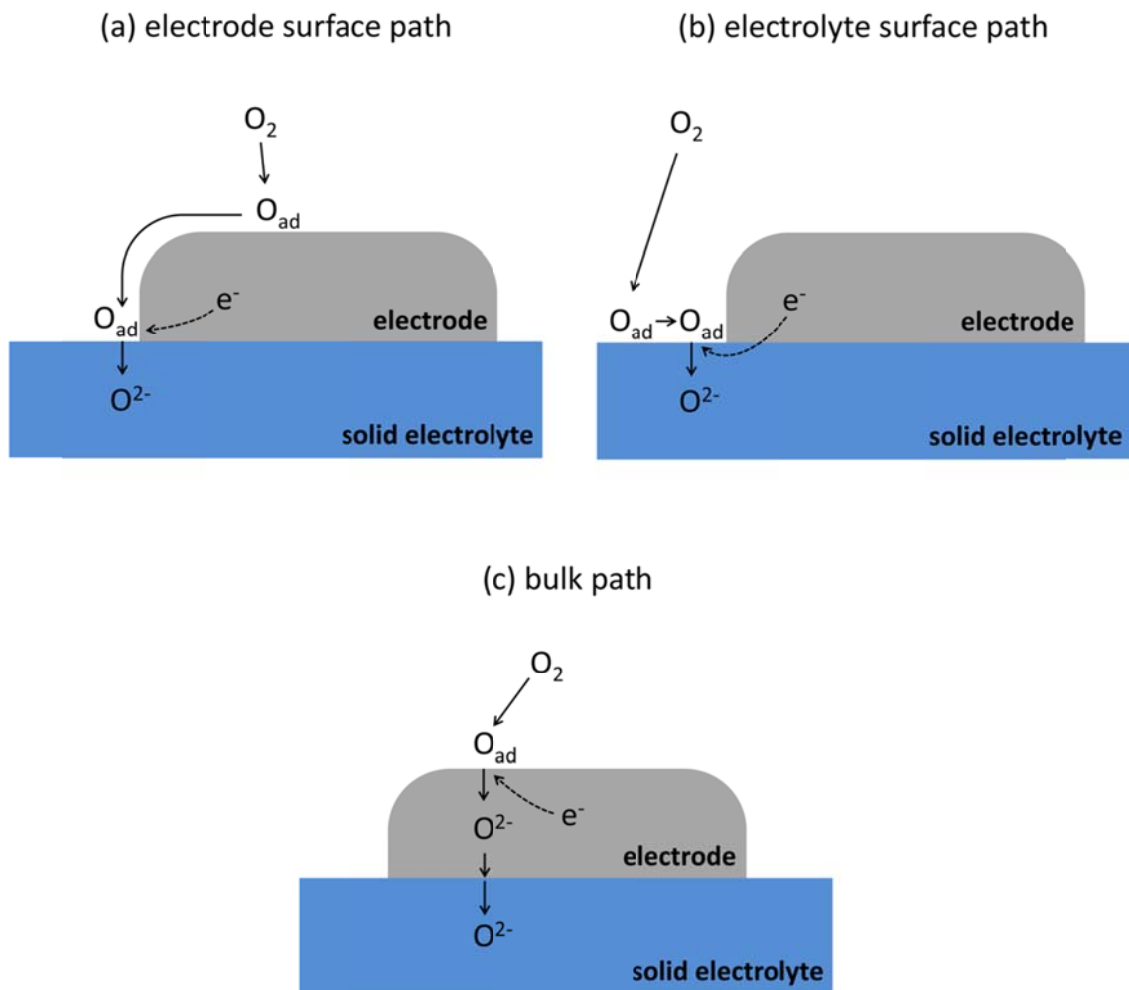


Figure 1: Three possible reaction pathways of oxygen exchange on solid oxide ion conductors. (a) Electrode surface path with oxygen adsorption on the electrode surface, diffusion along the surface to the TPB, and reduction as well as incorporation of oxygen into YSZ at the TPB. (b) Electrolyte surface path with adsorption and diffusion on the electrolyte surface. The electron transfer occurs via the electrolyte. (c) Bulk path in case of a mixed ionic electronic conducting electrode with the elementary steps adsorption and charge transfer on the electrode surface, diffusion of oxide ions through the electrode bulk and oxygen incorporation along the entire electrode\electrolyte interface.

electrodes is given. In the special case of MIEC electrodes the oxygen reduction reaction (i.e. the charge transfer) – after adsorption of oxygen on the electrode surface – proceeds on the electrode surface. The resulting oxide ions diffuse through the electrode bulk and are incorporated into the electrolyte at the entire two phase boundary between electrode and electrolyte [18, 27, 28]. Typical electrode materials exhibiting such a mechanism are lanthanum strontium cobaltite (LSC), lanthanum strontium ferrite (LSF), or barium strontium cobaltite ferrite (BSCF) [29-32]. However, the oxygen reduction in case of a bulk path is not necessarily restricted to the electrode surface. Silver electrodes, owing to the high solubility of atomic oxygen in the bulk of this material, also exhibit a bulk path. In contrast to MIEC electrodes the oxygen species diffusing through the silver bulk is an atomic instead of an ionic one and ionization can be assumed to take place at the electrode|electrolyte interface [23].

Also for Pt thin film electrodes some evidence for an additional bulk path in parallel to the commonly accepted surface path was reported in literature. An Auger electron spectroscopy study on sputter-deposited Pt thin films (10 – 100 nm thick) indicated that thin polycrystalline Pt films were not as impermeable for oxygen as generally assumed [33, 34]. Moreover, ab-initio calculations revealed that oxygen preferentially diffuses along Pt grain boundaries [35] and in a very recent study the possibility of a Pt bulk path and its consequences on the electrochemical behavior of Pt electrodes were discussed [36]. However, these studies do not contain conclusive results on the electrochemical relevance of this suggested Pt bulk path. In case of a dominating bulk path the electrochemical exchange rate should be proportional to the electrode surface rather than to the TPB length, at least for thin film electrodes. Conclusive data on the geometry dependency of the polarization resistance of a possible Pt bulk path are also lacking.

In principle simultaneous oxygen reduction via surface and bulk path is also possible and it is already known that on some electrode materials the oxygen exchange is not only restricted to either bulk or surface path; rather both electrochemical pathways significantly contribute to the total oxygen exchange current. Such a situation can be found for lanthanum strontium manganite (LSM) electrodes [4, 24, 37, 38]. A possible Pt bulk path would further increase the relevance of Pt electrodes as a model system in fundamental research.

1.2 Platinum electrodes – research history and present relevance

Because of their outstanding importance in fundamental research and technological applications the kinetics of oxygen exchange on solid oxide ion conductors was investigated from the beginnings of solid state electrochemistry [39]. However, despite this long history of research the reaction mechanism of oxygen reduction on the system platinum|yttria stabilized zirconia (YSZ) is still not as well understood as in aqueous systems. Hence, Pt(O₂)|YSZ is still a highly interesting system for fundamental electrochemical research [4, 7, 19, 21, 22, 26, 40-69]. The lack of quantitative understanding of the oxygen exchange reaction is partly due to the fact that in the past very often porous Pt electrodes were investigated [4, 26, 44, 46, 48, 53, 54, 58, 60, 63, 67, 70]. Even though porous electrodes prepared by deposition of Pt paste exhibit the advantage of being realistic from a technological point of view (e.g. in oxygen sensors), they suffer from an ill-defined geometry and the unknown chemical composition of commercial Pt pastes. A systematic and defined variation of three phase boundary length and surface area is thus hardly possible. As a consequence the results obtained in these studies are often not fully conclusive. For example, in Refs. [53, 67, 71] an adsorption step of oxygen on Pt is suggested to be rate limiting whereas in Refs. [47, 58, 70, 72] a rate limiting surface diffusion of adsorbed oxygen is discussed. On the basis of these results, also co-limited kinetics of adsorption and surface diffusion were suggested [4] which means that neither adsorption nor surface diffusion alone, but both together are responsible for the limitation of the electrochemical reaction rate. Moreover, in some studies a charge transfer reaction was discussed to significantly contribute to the polarization resistance of Pt electrodes on YSZ [67, 68, 71, 73].

In an attempt to eliminate the problems with porous paste electrodes Pt point contacts were pressed onto the electrolyte surface [40-42, 64, 68, 69]. In Ref. [41] it was demonstrated that this method allows a meaningful comparison of the electrochemical activity of different electrode materials – one among them being Pt. In Refs. [42] and [69] this type of model electrodes was employed to investigate the electrochemical effect of an assumed PtO_x “phase”. The separation of effects supposedly related to PtO_x from other electrochemical phenomena was shown to be much easier than in case of porous paste electrodes and thus these experiences further supported the importance

of model electrodes for a fundamental understanding of oxygen exchange kinetics on Pt|YSZ. Moreover, interesting observations regarding chemical and morphological changes of the Pt|YSZ interface as well as the TPB region during electrochemical measurements were reported in studies on point contact electrodes [40, 69]. However, a defined variation of the electrode geometry was again difficult to realize with this type of model electrodes. As a consequence previous data obtained on porous and on point electrodes are still not completely conclusive regarding the question where the rate determining step is located. For example the normalized polarization resistance caused by the kinetically slowest step strongly varied from one study to the other. At 600 °C a TPB length related polarization resistance of $10^6 \Omega\text{cm}$ was obtained in Ref. [40] whereas $2 \cdot 10^4 \Omega\text{cm}$ were reported for the same temperature in Ref. [42]. Thus oxygen reduction kinetics of Pt electrodes seems to be strongly affected by unknown parameters which are not understood yet.

A possibility to overcome many shortcomings of porous electrodes is the use of dense and geometrically well-defined microelectrodes or micro-patterned electrodes prepared by thin film deposition and photolithographic micro-structuring. An important advantage of such electrodes, provided that the thin film is gas-tight, is their well-defined shape and thus a defined TPB length and surface area. Furthermore a large number of electrodes with varying shape and size can be prepared in a single run, which is attractive from a practical point of view. Especially in the case of surface path kinetics with a rate limiting step close to the three phase boundary the use of geometrically well-defined microelectrodes is beneficial compared to macroscopic thin films when using impedance spectroscopy as electrochemical characterization method. Two reasons for this should briefly be mentioned in the following.

i) In case of a rate limiting elementary step close to the TPB the electrochemical exchange rate and thus the inverse polarization resistance $1/R_{ode}$ of the electrode reaction depends on the TPB length. In case of circular electrodes with diameter d_{ME} it thus holds

$$\frac{1}{R_{ode}} \propto d_{ME} \cdot \quad (1)$$

The interfacial capacitance C_{int} of a predominantly electronically conducting electrode on a solid oxide ion conductor can be assumed to be established along the entire two phase boundary and consequently

$$C_{\text{int}} \propto d_{\text{ME}}^2 \quad (2)$$

can be assumed. To achieve impedance measurements within an acceptable time, the characteristic angular frequency ω^* of the electrodes' impedance feature should be above ~ 10 mHz. For a parallel connection of the dominating resistive and capacitive process (which is a reasonable simplification for most electrodes) the angular frequency is given by

$$\omega^* = \frac{1}{R_{\text{ode}} \cdot C_{\text{int}}} \quad (3)$$

Inserting Eqs. 1 and 2 into 3 yields

$$\omega^* \propto \frac{1}{d_{\text{ME}}} \quad (4)$$

Consequently on microelectrodes at equal temperature the same information can be gained within a smaller time or even more information about the electrode impedance can be gained within the same frequency range than in case of dense macroscopic electrodes.

ii) A second substantial advantage of microelectrodes compared to macroscopic electrodes is the possibility to avoid reference electrodes [74, 75]. Owing to the tremendous difference in size between extended counter- and microelectrode the electrochemical response is almost exclusively attributed to the microelectrode [31] (see also Sec. 4.1).

In previous work of several authors lithographically micro-structured thin film electrodes were successfully applied as a powerful tool for the investigation of bulk as well as electrode properties [19, 21, 22, 24, 30, 31, 45, 49-51, 62, 65, 74, 76-80]. However, preparation of micro-patterned Pt electrodes on YSZ staying dense also at high temperatures turned out to be difficult [21, 22]. Only recently Pt thin film elec-

trodes were prepared by pulsed laser deposition (PLD) in such a way that they remained dense and geometrically (TPB) stable even during high temperature treatment [21, 54]. Experiments on such dense Pt model electrodes revealed numerous new insights into the reaction mechanism of oxygen exchange kinetics: In Refs. [19] and [66] electrode processes on Pt|YSZ were investigated by means of photoelectron microscopy. In these studies it was possible for the first time to in situ observe the spill-over of electrochemically released oxygen from the TPB across the entire Pt surface. In another study on micro-patterned sputter-deposited electrodes the geometry dependence of the polarization resistance was investigated [22]. However, these electrodes suffered from pores, which evolved during the electrochemical characterization at elevated temperatures. The results – suggesting a TPB-related polarization resistance at temperatures between 650 and 800 °C – were thus not completely conclusive. Consequently a study which unambiguously proves the geometry dependence of the electrochemical oxygen exchange reaction on Pt|YSZ is still missing.

1.3 Analysis of the TPB width

In case of a dominating Pt surface path, another question on the oxygen exchange kinetics of Pt|YSZ systems, which is still not answered satisfactorily, deals with the width and exact location of the electrochemically active zone. This oxygen incorporation zone is hardly a one-dimensional line along the TPB. Oxygen surface diffusion, ionic conductivity along interfaces, and electron conduction in the electrolyte are only three examples resulting in a certain spatial extension of the electrochemically active zone. This broadening of the three phase boundary (“TPB width”) is also an important parameter in numerical modeling of electrode behavior in SOFCs and its knowledge would help improving the reliability of simulation results. Because of the lack of experimental data its value was often simply estimated in the past [43, 62, 81]. Three situations of lateral extension of the electrochemically active zone have to be considered [38, 49, 82]: First, an extension along the free YSZ surface, which means that the incorporation of oxide ions takes place on the free surface of the electrolyte (cf. Fig. 2a). This situation can be expected for a spill-over of an oxygen species from the Pt-surface to YSZ or for a finite electronic conductivity with oxygen adsorption and ionization on the

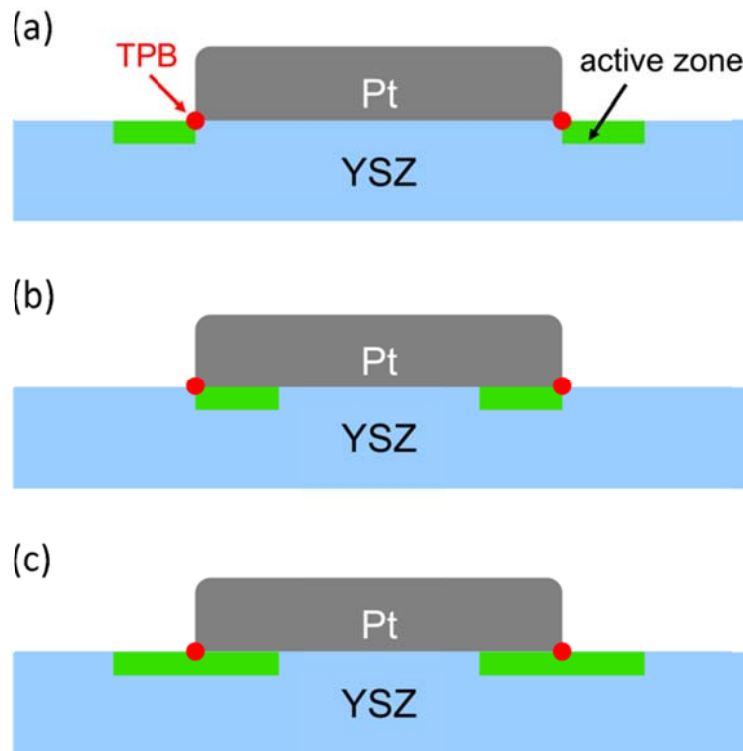


Figure 2: Three possible locations of the electrochemically active zone of oxygen incorporation into YSZ: (a) Incorporation zone only extends along the free electrolyte surface. (b) Active zone sited beneath the platinum electrode (at the Pt|YSZ interface). (c) Situation combining the zones in (a) and (b).

YSZ surface (electrolyte surface path). This also means that the Pt|YSZ interface is either inaccessible for the oxygen species available at the TPB or exhibits a much lower diffusivity/conductivity compared to the free YSZ surface. The second case (Fig. 2b) is an exclusive extension of the incorporation zone along the electrode|electrolyte interface. For this pathway sufficient solubility of an oxygen species in the interfacial region is essential and its interfacial mobility has to be high. The third scenario (Fig. 2c) combines both situations resulting in a (possibly asymmetric) lateral broadening of the active zone in both directions, along the Pt|YSZ interface as well as along the free YSZ-surface.

One possibility to experimentally obtain information on the lateral extension of the active zone is based on the analysis of the current constriction resistance of the electrolyte [62, 83, 84]. However, this method is not very precise and also does not give any information on the lateral direction of the TPB broadening. A pretty smart approach to visualize O_2 reduction sites makes use of oxygen tracer incorporation [37, 44, 45, 85,

86]. This technique was the first time successfully applied in the study in Ref. [44] where ^{18}O was electrochemically incorporated at porous Pt paste electrodes and the spatial distribution of the tracer in YSZ was subsequently analyzed by secondary ion mass spectrometry (SIMS). This technique allowed to distinguish between oxygen, which was incorporated during the electrochemical experiment (^{18}O) and native lattice oxygen in YSZ (almost entirely ^{16}O) and can thus visualize electrochemically active zones. Moreover, these measurements suggested an oxygen incorporation beneath the Pt particles at the Pt|YSZ interface rather than on the free YSZ surface. In an attempt to determine the width of the electrochemically active zone the authors also employed micro-patterned Pt and Au electrodes with geometrically well-defined triple phase boundaries [45, 86]. On both electrode materials a significant increase in tracer concentration at the TPB could be observed in these studies.

Moreover, this technique was also applied to image the oxygen reduction sites at LSM electrodes [37, 85]. In these studies ^{18}O isotope was electrochemically incorporated into the electrolyte at photolithographically patterned LSM thin film electrodes. From these measurements conclusions regarding the diffusion of the tracer in the electrode, oxide ion transfer at the LSM|YSZ interface, and tracer diffusion in YSZ were obtained. Similarly to Pt and Au electrodes an increased tracer concentration at the TPB of the electrodes was observed. However, owing to the relatively high experimental temperatures of 500 -700 °C the TPB-width could not be quantified neither in the LSM nor in the Pt and Au studies. The reason for that is discussed in the following.

A major challenge of this experimental approach is related to the fact that the lateral extension of the resulting tracer profile in the electrolyte not only reflects electrocatalytic effects at the surfaces or TPBs, but is also caused by mass transport of $^{18}\text{O}^{2-}$ in the electrolyte. This additional mass transport could either be tracer concentration driven or field driven and may strongly distort the mapping of the electrochemical activity close to the TPB. In Refs. [87, 88] it was discussed, to which extent tracer motion in electrolytes under voltage is field driven or concentration driven. As a main result it was found that the contribution of field driven $^{18}\text{O}^{2-}$ migration in the bulk is small compared to diffusional contributions as long as ^{18}O concentrations in YSZ are kept below approximately 10%. Hence, in the lower concentration range only tracer diffusion in the electrolyte has to be controlled or minimized in order to avoid an unintentional broadening of the incorporation zone.

A promising strategy for limiting the systematic error caused by this bulk tracer diffusion is keeping the temperature – and thus the thermally activated tracer diffusion coefficient D^* – as low as possible. In case of one dimensional semi-infinite diffusion the tracer diffusion length L_{diff} within a given time t can be calculated by

$$L_{\text{diff}} = \sqrt{D^* \cdot t} \quad (5)$$

and some numerical values are given in Tab. 1 to point out the tremendous effect of temperature T on the diffusion length and thus on a diffusive profile broadening. The substantial diffusion length of $5 \mu\text{m}$ already within ten seconds at $700 \text{ }^\circ\text{C}$ already explains why quantification of the TPB width was not possible in the experiments mentioned above: The tracer profile of an incorporation experiment of 10 seconds already broadens solely by bulk diffusion to about $10 \mu\text{m}$ ($2 \times L_{\text{diff}}$) even for an ideally line shaped incorporation zone. In Tab. 1 the tracer diffusion coefficient of $^{18}\text{O}^{2-}$ in YSZ was calculated from conductivity data measured on YSZ single crystals containing 9.5mol% Y_2O_3 and the relationship

$$\frac{D^*}{k_B T} = \frac{\sigma_{\text{ion}}}{n_{\text{ion}} \cdot 4 \cdot e_0^2} \cdot f_C \quad (6)$$

between tracer diffusion coefficient and ionic conductivity σ_{ion} [89]. In Eq. 6 n_{ion} denotes the number of oxygen ions in YSZ per unit volume ($5.7 \cdot 10^{22} \text{ cm}^{-3}$ in case of 9.5 mol% YSZ), e_0 the elementary charge, k_B Boltzmann's constant and f_C the correlation factor which is approximately 0.65 for a simple cubic anion sub-lattice [90]. A comparison of

Table 1: Influence of temperature and time on the diffusion length of ^{18}O tracer in YSZ.

T [°C]	σ_{ion} [$\Omega^{-1}\text{cm}^{-1}$]	D^* [cm^2s^{-1}]	t [s]	L_{diff} [μm]
300	$2.5 \cdot 10^{-6}$	$2.2 \cdot 10^{-12}$	10	0.05
			300	0.25
			600	0.36
700	$1.7 \cdot 10^{-2}$	$2.5 \cdot 10^{-8}$	10	5.0

the results in Tab. 1 for 300 and 700 °C further emphasizes the importance of a rather low temperature during such oxygen incorporation experiments. However, low temperatures strongly increase polarization resistances and thus relatively high voltages might be necessary to pump sufficient tracer ions into the electrolyte. Such measurements were not available so far.

1.4 Goals of this thesis

The aim of the present thesis was the investigation of the electrochemical oxygen exchange mechanism and the reaction pathways on the system Pt|YSZ in a broad range of temperatures and overpotentials by using novel approaches and combining several techniques. In the first part the resistances and capacitances caused by electrochemical oxygen exchange and its elementary processes at Pt electrodes on YSZ was investigated. Experiments were carried out on dense and geometrically well-defined Pt (111) thin film microelectrodes on YSZ (100) single crystals. The electrodes were investigated by electrochemical impedance spectroscopy between 300 and 900 °C. By variation of the microelectrode size the location of resistive and capacitive processes could be analyzed. Also information on the existence or non-existence of a reaction pathway of oxygen exchange through the Pt thin film (in parallel to the Pt surface path) was gained from the geometry dependence of the resistance related to the rate determining step.

The goal of the second part – a ^{18}O tracer study – was the visualization and quantification of the electrochemically active zone of platinum electrodes on YSZ using voltage driven ^{18}O tracer incorporation. Experiments were again conducted on Pt thin film microelectrodes on YSZ single crystals. To minimize the critical diffusive broadening of the tracer profiles, temperatures as low as 300 – 330 °C were chosen. Investigation of the spatial ^{18}O distribution was performed by time-of-flight secondary ion mass spectrometry (ToF-SIMS). The effects of polarization on the shape and the lateral extension of the electrochemically active zone were studied and mechanistic conclusions were drawn.

In the third part the steady-state current-voltage characteristics of Pt electrodes on YSZ in a temperature range between 600 and 750 °C were explored. The temperature was chosen such, that the oxygen exchange mechanism close to equilibrium can

safely be assumed to predominantly proceed via the surface path with a rate limiting step close to the TPB. From the measured current-overpotential curves additional information on the nature of the rate limiting step around equilibrium condition and low cathodic polarization was obtained.

Altogether these studies based on different methods lead to many new insights into oxygen exchange on Pt|YSZ and to a significant progress in understanding the reaction mechanisms and electrochemical pathways of this important model reaction on a solid electrolyte.

2 Experimental

2.1 Sample preparation

2.1.1 High temperature deposition of Pt

The high temperature deposition of platinum thin films was done by a procedure similar to that presented in Ref. [21] where high substrate temperatures were shown to lead to an improved temperature stability of pulsed laser deposited (PLD) Pt films: Platinum (99.95 % pure, ÖGUSSA, Austria) was sputter-deposited (MED 020 Coating System, BAL-TEC, Germany) onto polished (100)-oriented YSZ single crystals (9.5 mol% Y₂O₃, Crystec, Germany) which were held at a temperature of ~700 °C; the argon pressure in the sputter chamber was $5 \cdot 10^{-2}$ mbar. The film thickness of about 500 nm was determined by ex-situ calibration using a quartz micro-balance. The platinum films were micro-structured by standard photolithography (ma-N 1420 negative photoresist and ma-D 533 S developer for photoresist, both: micro resist technology, Germany) using a photomask (Rose, Germany) which allowed preparation of numerous circular-shaped microelectrodes with different diameters on each sample. The required etching process was performed in hot aqua regia. The samples were subsequently annealed at 700 – 750 °C for 48 h in air.

Further sample characterization was performed by scanning electron microscopy (SEM) on a FEI Quanta 200 (FEI Company, The Netherlands) and by X-ray diffraction (XRD) on an X'Pert PRO Diffractometer (PANalytical, Almelo/NL), PW 3050/60 goniometer with para-focussing Bragg-Brentano arrangement, copper anode (long fine focus, Cu-K_{α1} and Cu-K_{α2} wavelength), divergence slit 0.5°, Soller collimator with an axial divergence of 2.3° on primary and secondary side, secondary sided Ni-K_β filter and X'Celerator detector. For results see Secs. 3.1.1 (REM) and 3.2.1 (XRD).

For electrochemical measurements a counter electrode was attached to the back side of the samples by depositing porous paste electrodes. In the first experiments silver paste (Heraeus, Germany) was used for this purpose. Despite no indication of Ag

contamination on the free YSZ surface was found in SIMS experiments, Pt paste electrodes (Gwent Electronic Materials, UK) were used as counter electrodes on all other samples.

2.1.2 Low temperature deposition of Pt

Low temperature sputter-deposition of platinum was also carried out by sputtering of Pt onto YSZ (100) single crystals. In contrast to the high temperature process the YSZ substrate was not externally heated during the deposition and the chamber pressure was set to $2.0 \pm 0.1 \cdot 10^{-2}$ mbar argon. The nominal film thickness of 350 nm was

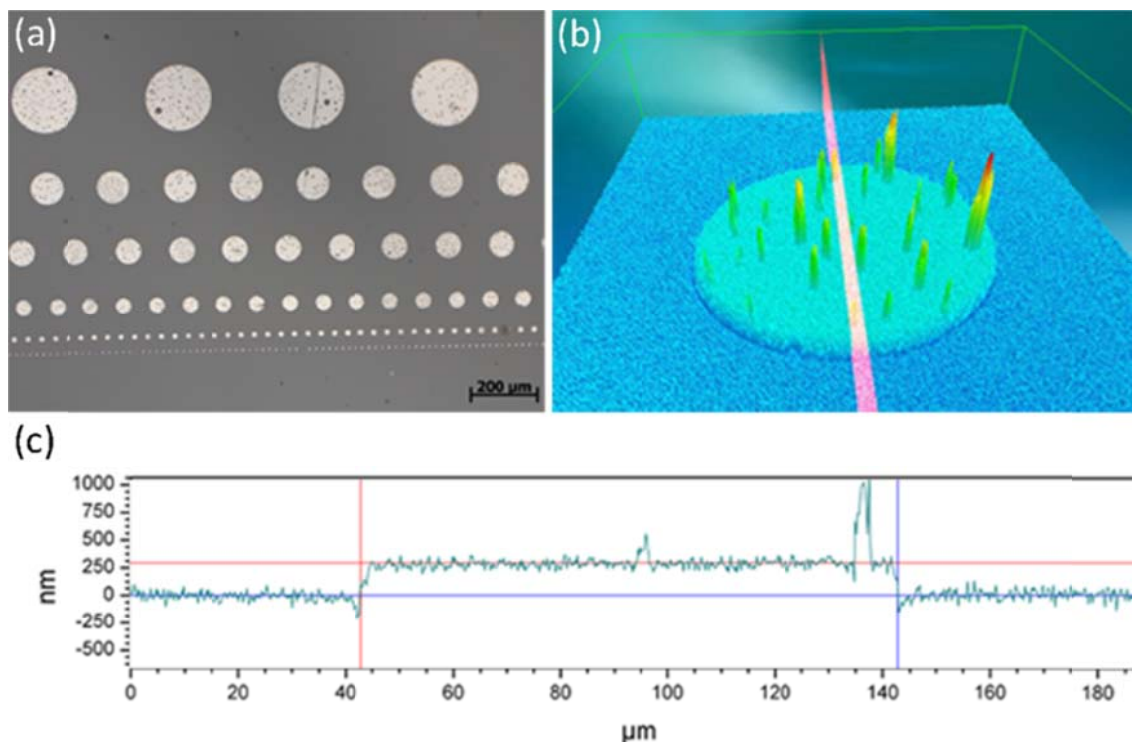


Figure 3: (a) Optical micrograph of circular Pt thin film electrodes on a YSZ (100) single crystal. Nominal electrode sizes are (from top to bottom): 200, 100, 80, 50, 20, and 10 μm. The dark dots on the surface of the Pt electrodes were neither pores nor pinholes but bubbles which evolved during the annealing process (see also Figs. 14d and e). (b) 3D image of a 100 μm electrode measured by confocal microscopy; the height information is color-coded with blue indicating low and red indicating high values (note that the height axis is strongly exaggerated). The “spikes” in the image were bubbles. The red plane across the electrode indicates the cross section plane for height profiling – the corresponding height profile is given in (c).

controlled during the sputter process by means of a quartz micro-balance. Microstructuring of the Pt films was performed by lift-off photolithography. As a counter electrode Pt paste was applied onto the back side of the YSZ single crystals. The samples were subsequently annealed at 750 °C for two hours. An optical micrograph after the annealing step is shown in Fig. 3a. The film thickness of the microelectrodes was also measured by means of a confocal microscope (AXIO CSM 700, Zeiss, Germany) – a 3D image of a 100 µm electrode is shown in Fig. 3b. A height profile along the cross section plane (indicated as transparent red plane in Fig. 3b) is given in Fig. 3c. From this height profile an electrode diameter of 100.2 µm and a thickness of the Pt film of about 300 nm were determined. Also the diameters of other microelectrode sizes were always very close to the nominal values and height measurements yielded values between 300 and 380 nm. These results are in acceptable agreement with the nominal thickness of 350 nm obtained by means of the quartz micro-balance during the sputter process.

High resolution SEM investigations of the low temperature deposited Pt thin films were performed on a Quanta 200 FEG with Schottky emitter (FEI Europe, The Netherlands). Results of these SEM measurements are shown in Sec. 3.1.2. Additionally XRD-patterns were measured directly after deposition of the Pt and after the 2h annealing step at 750 °C – for results see Sec. 3.1.2.

2.2 Electrochemical measurements

2.2.1 Two-point impedance measurements

A schematic drawing of the setup used for two-point impedance measurements is shown in Fig. 4a. The sample was placed onto a heating stage (Linkam, UK) which allowed measurements at set temperatures up to 1000 °C. To prevent the porous counter electrode from sticking on the heating stage a 0.33mm thin sapphire disc (Crystec, Germany) was introduced between them. Electrical contact was established under a microscope (Mitutoyo, Japan) using Pt/Ir tips (Süss MicroTec, Germany) in case of high temperatures or gold-coated steel tips (acupuncture needles, Pierenkemper, Germany) in case of temperatures below ~600 °C. The tips could be accurately positioned by mi-

romanipulators (Mitutoyo, Japan). Fig. 4b displays a view through the microscope while contacting a microelectrode. Impedance spectra were typically recorded in a frequency range between 1MHz and 50mHz with a resolution of at least 5 points per decade using an Alpha-A High Resolution Dielectric Analyzer (Novocontrol, Germany). The ac voltage was 0.01 V (rms) and all measurements were performed in ambient air.

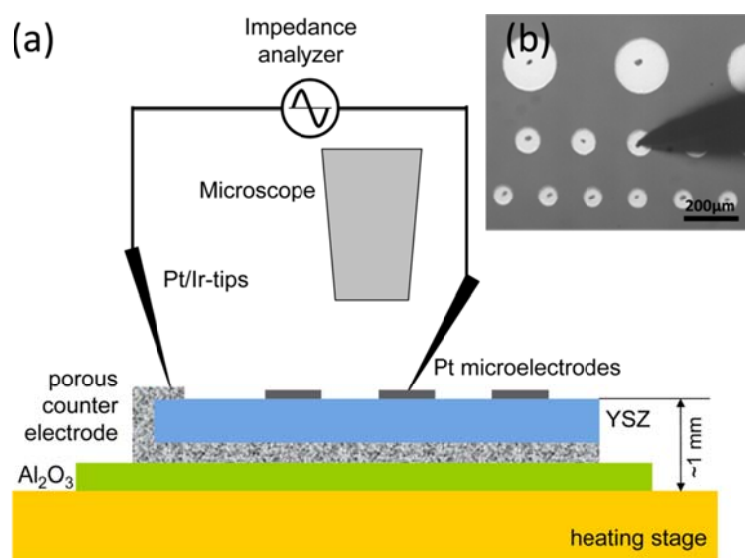


Figure 4: (a) Sketch of the experimental setup for two-point impedance measurements. (b) View through the microscope with one 100 μm electrode being contacted. The spots on the other electrodes were caused by the contacting tip during earlier measurements.

2.2.2 Pseudo four-point impedance measurements

Some of the electrochemical experiments were conducted in a pseudo 4-wire setup instead of a conventional 2-wire setup (POT/GAL 30V 2A test interface together with an Alpha-A High Resolution Dielectric Analyzer, both: Novocontrol, Germany). The spectra were recorded in a frequency range of 1 MHz – 10 mHz with a resolution of 10 frequency points per decade and an ac voltage of 0.01 V (rms).

In addition a variable capacitor was connected in series during measurement (see Fig. 5). Reasons for these modifications should be explained in the following: Owing to

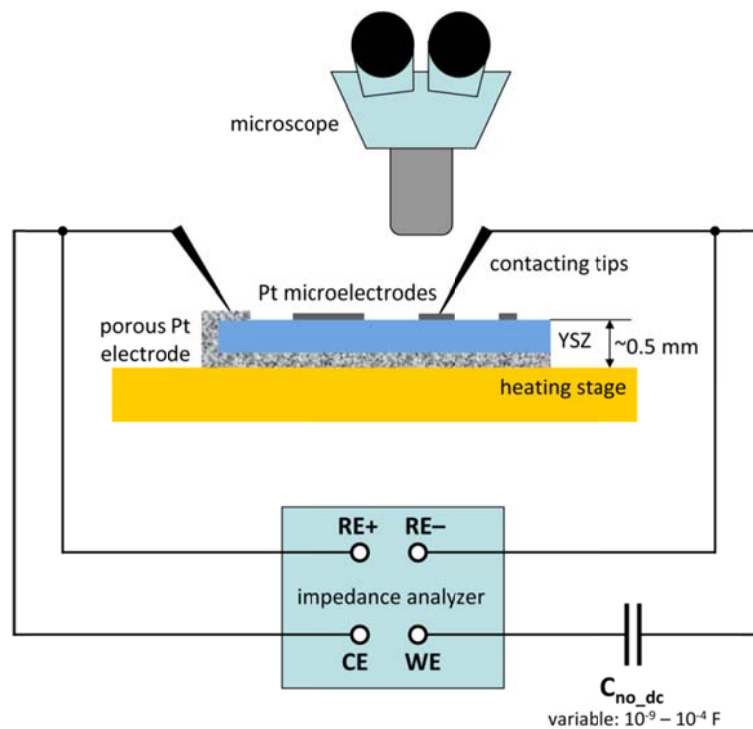


Figure 5: Sketch of the setup used for pseudo four-point impedance measurements. The notations of the connectors of the impedance analyzer CE, WE and RE denote counter electrode, working electrode and reference electrode, respectively. The meaning of capacitor C_{no_dc} is explained throughout the text (Sec. 2.2.2).

the asymmetrical heating of the sample on the heating table and an additional cooling effect of the contacted microelectrode by the tip, a temperature gradient across the sample was generated. This temperature gradient is believed to be responsible for a thermovoltage between micro- and counter electrode [91, 92]. On the one hand, the temperature gradient in the YSZ itself generates a voltage due to its thermoelectric power of ~ 0.5 mV/K [91]. On the other hand, the different temperatures of the contact points (clamp/tip, tip/electrode or electrode/electrolyte) could also contribute to a thermovoltage. In Fig. 6 a plot of the voltage, measured between $100\ \mu\text{m}$ electrodes and the counter electrode under open circuit conditions, versus the set temperature is shown. Since the input resistance of the counter electrode (CE) connector versus the working electrode (WE) connector of the test interface is specified as virtually zero ohms, the thermovoltage was short circuited by the impedance analyzer. Hence, the resulting current – despite no external bias voltage was applied – led to a polarization

of the electrode and consequently the impedance measurements could not be done at equilibrium conditions. To overcome this effect, the above mentioned capacitor (denoted as $C_{\text{no_dc}}$ in Fig. 5) in series to analyzer and sample was introduced into the measurement setup. In a conventional 2-wire setup this capacitor would of course change the resulting impedance response (resulting in a vertical line in the low frequency part of the Nyquist plot). In the pseudo 4-wire measurement shown in Fig. 5, however, this capacitor would not be “visible” in the measured spectrum (and neither are the inductances of the cables). A short circuiting of the thermovoltage via the reference electrode connectors could be ruled out due to their input resistance of $> 10^{12} \Omega$. Since the connection of the capacitor $C_{\text{no_dc}}$ in series to the resistance of the sample R_{samp} acted as a filter for low frequency ac signals, the value of $C_{\text{no_dc}}$ had to be individually adjusted for each measurement. It was chosen such that the characteristic angular frequency of the measuring system $\omega^* \approx 1/(R_{\text{samp}} \cdot C_{\text{no_dc}})$ was about one order of magnitude below the lowest measured point. Consequently, before any impedance measurements a delay time $\tau > 1/\omega^*$ was waited to charge the capacitor.

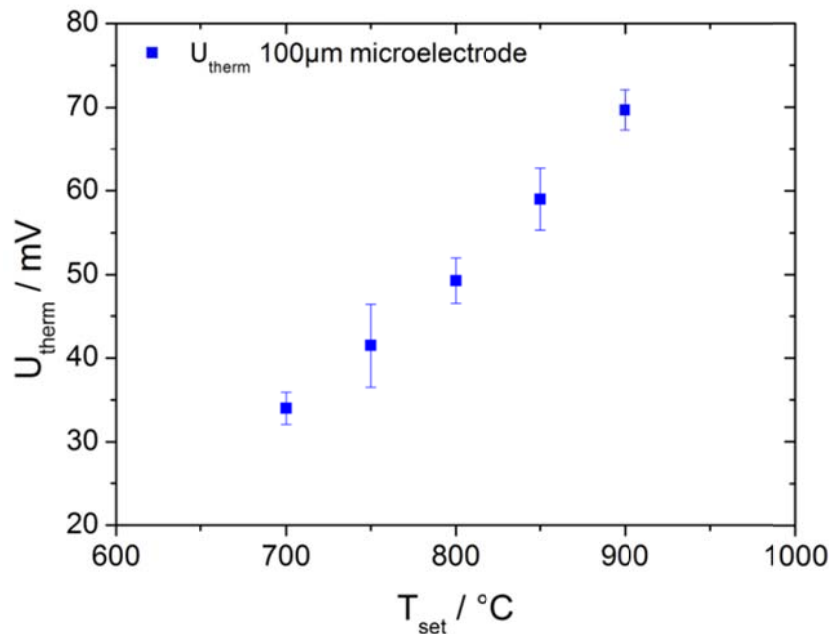


Figure 6: Plot of the thermovoltage measured between a $100 \mu\text{m}$ microelectrode and the counter electrode versus the set temperature.

The effect of the blocking capacitor on the impedance measurements is demonstrated in Fig. 7, where spectra recorded with and without C_{no_dc} are shown. In Fig. 7a the low frequency features of the impedance spectra are compared. In case of measurements without the blocking capacitor the electrode polarization resistance is about 20% larger than with $C_{no_dc} = 10 \mu\text{F}$. A temperature effect can definitely be excluded since all of the measurements exhibited the same spreading resistance of the YSZ electrolyte as can be seen from the coincident high frequency axis intercepts in Fig. 7b. The behavior, however, can be explained by the polarization of the electrode due to the short circuiting of a thermovoltage as already mentioned above. Reasons why a polarized electrode (measurement without blocking capacitor C_{no_dc}) exhibits a higher differential resistance than an electrode in equilibrium (measurement with C_{no_dc}) should be explained briefly in the following: In Fig. 8 a steady-state dc measurement on the same Pt electrode is shown (see also Sec. 2.2.3). The $I-\eta$ curve is shifted to more positive overpotentials due to the mentioned thermovoltage, which was 10 mV in the present case. Impedance spectroscopy without the blocking capacitor provides the differential resistance (i.e. the inverse slope of the $I-\eta$ curve) in the point indicated by the black arrow, whereas impedance measurements with C_{no_dc} yield the differential resistance of the point indicated by the red arrow. Since the slope of the $I-\eta$ curve is higher at equilibrium conditions (red arrow, $I = 0$) the polarization resistance measured with C_{no_dc} is lower (~20 % in that case). A detailed discussion of the $I-\eta$ characteristics as well as reasons for not exhibiting Butler-Volmer-like kinetics will be given in Sec. 6.

In addition the spectra recorded without a blocking capacitor exhibit indication for a degradation process: the electrode arc is obviously increasing from measurement to measurement. Introduction of C_{no_dc} into the setup also stopped this growing of the electrode semicircle. One possible explanation for this degradation process might be polarization induced changes of the electrodes – e.g. accumulation of impurities at the TPB [56, 93, 94]. Another reason might be related to polarization induced changes of possibly existing PtO_x at the surface of the electrodes or at the Pt|YSZ interface [42, 95]. (Both kinds of changes may either be irreversible or reversible on a much larger time-scale than the charging of the electrodes interfacial capacitor.)

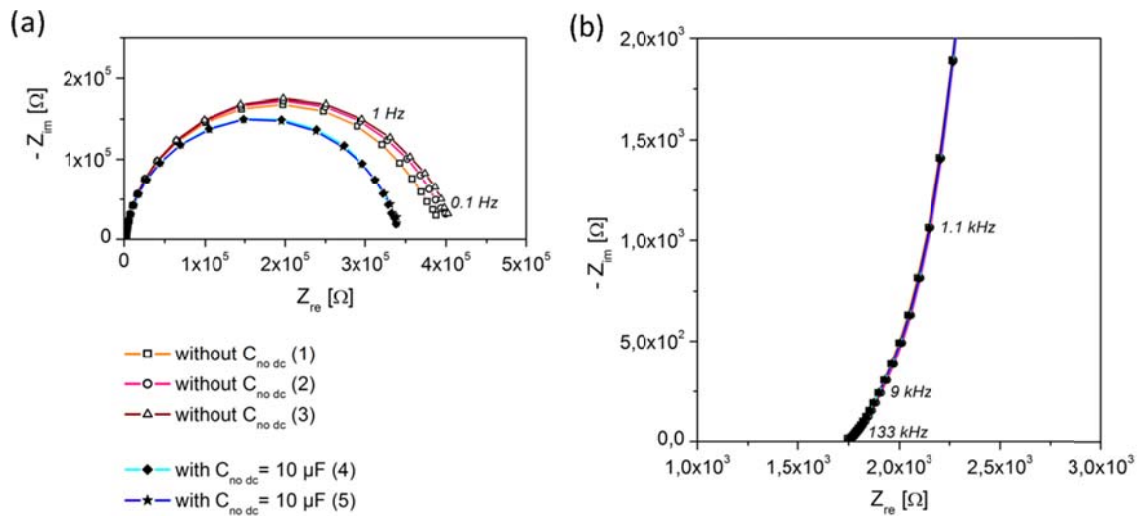


Figure 7: Impedance spectra (Nyquist plot) measured on one single circular 200 μm Pt electrode (686 $^{\circ}\text{C}$). The numbers in brackets in the caption denote the chronological order of the respective measurement. (a) The dominating electrode feature is clearly affected by introducing the blocking capacitor C_{no_dc} (which was 10 μF in this case): The measurements done without C_{no_dc} yield a polarization resistance $\sim 20\%$ larger than the measurements done with the blocking capacitor. (Please note that the absolute values are not really comparable to the results in Sec. 4 since these test electrodes had quite different thermal history) (b) Magnification of the high frequency part of the spectrum exhibiting the same YSZ bulk resistance value for all measurements.

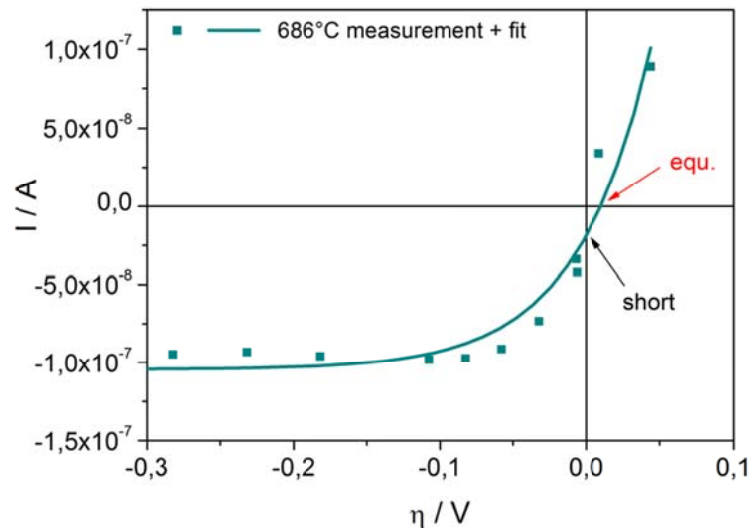


Figure 8: Current-voltage measurements obtained on the same electrode as the impedance spectra in Fig. 7 together with a fit curve (see Sec. 6.1). The voltage shift of the curve is caused by a thermovoltage (10 mV in this case). The red and the black arrow indicate the point of impedance measurements in equilibrium (with C_{no_dc}) and of short circuited impedance measurements (without C_{no_dc}), respectively. The difference in the slope at these two-points is about 20 %.

2.2.3 DC measurements

A sketch of the dc setup is shown in Fig. 9a; in Fig. 9b a view through the microscope is depicted. To minimize deteriorating electrical effects of the heating stage during electrochemical measurements a thin Pt sheet was introduced as shielding between sample and heating stage. The shielding was set to ground potential of the analyzer. To prevent shorts of the sample to ground a thin sapphire disc was used to separate sample and shielding.

The current-voltage measurements were performed on an Alpha-A High Performance Frequency Analyzer with POT/GAL 30V 2A test interface in dc mode (control software: Winchem, Novocontrol, Germany) on high temperature deposited $100\ \mu\text{m}$ Pt electrodes (cf. Sec. 2.1.1) between set temperatures of 700 and 850 °C in 25 °C steps. Owing to the asymmetric heating, the Pt shield and the sapphire disk beneath the sample, as well as the contact with the Pt/Ir tip the true electrode temperature differed

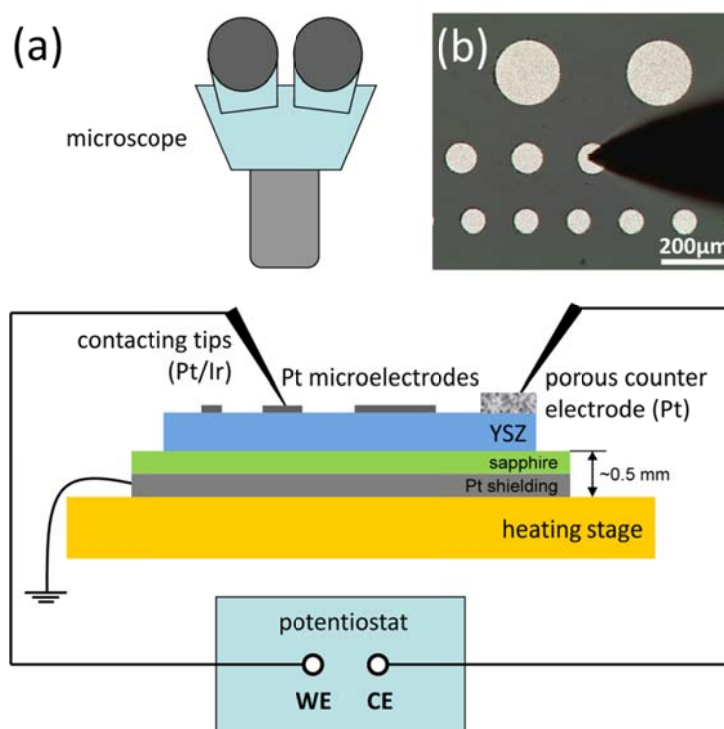


Figure 9: (a) Sketch of the dc-measurement setup. The labels of the connectors on the potentiostat denote working electrode and counter electrode, respectively. (b) View through the microscope with a $100\ \mu\text{m}$ microelectrode contacted by a tip (black wedge on the right hand side).

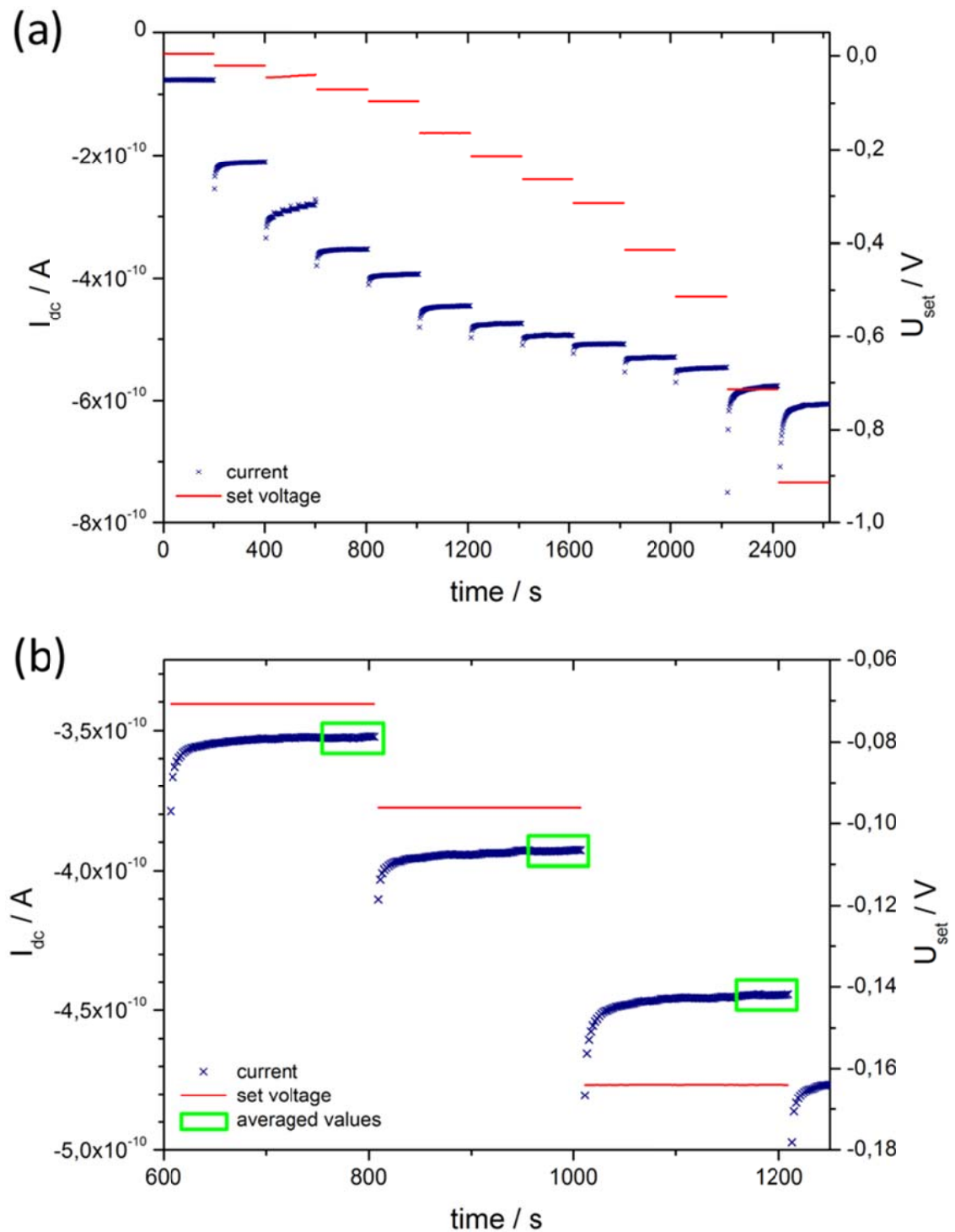


Figure 10: Measured current (left y-axis) and voltage (right y-axis) plotted as a function of time for a corrected temperature of 681 °C. (a) Interval between the start of the experiment and a cathodic polarization of -0.9 V. The holding time at each set voltage was 200 s. (b) Magnification of three I-t characteristics (at three voltage set points) showing the typical relaxation characteristics of R-C elements (i.e. charging of the interfacial capacitance). The green boxes denote the current values, which were averaged to obtain I- η curves.

from the set temperature by about 120 °C. The effective electrode temperature was calculated from the spreading resistance of ion conduction in YSZ (which was obtained by impedance measurements) by Eq. 9 (Sec. 4.1.1). For measurements of the I- η curves the set voltage was held constant for 200 s and the corresponding current was recorded every second. Between +0.1 and -1.5 V 22 voltage values were applied and the corresponding current was recorded. The voltage steps were between 25 and 200 mV with smaller step widths close to equilibrium. An exemplary curve showing the measured current as a function of measurement time is given in Fig. 10a. The I-t curves at each voltage set point show the typical relaxation characteristics of R-C elements. In order to exclude this charging current of the interfacial electrode capacitor, only the last 25 points (which almost exclusively reflect the faradaic current at the respective voltage) were averaged and taken into account for further analysis – cf. Fig. 10b. The voltage range was not only passed through once, but voltage cycling was performed to check for any irreversible changes of the system upon polarization.

2.3 ¹⁸O tracer incorporation experiments

2.3.1 Experimental setup for ¹⁸O incorporation

The setup for the ¹⁸O incorporation experiments and the way of establishing electrical contact was essentially the same as for the two-point impedance measurement. As a tracer gaseous ¹⁸O₂ (97% isotopic enrichment, Cambridge Isotope Laboratories, UK) was locally supplied to the contacted microelectrode by means of a quartz capillary which could be accurately positioned by a micromanipulator; a sketch of the setup for these dc-experiments is depicted in Fig. 11. The set temperature was 350 °C leading to effective electrode temperatures of about 300 - 330 °C. For incorporation of the tracer into YSZ cathodic dc voltages of -2.00 V, -2.10 V, -2.20 V, -2.25 V, and -2.50 V were applied to the microelectrode. Such rather high voltages were required to achieve sufficiently high dc currents in the tracer experiments (see Sec. 5.1.3). Voltage supply and current measurement were performed with a source-measure unit (Keithley 2611, USA). The first 100 - 200 seconds of the polarization experiments were carried out in

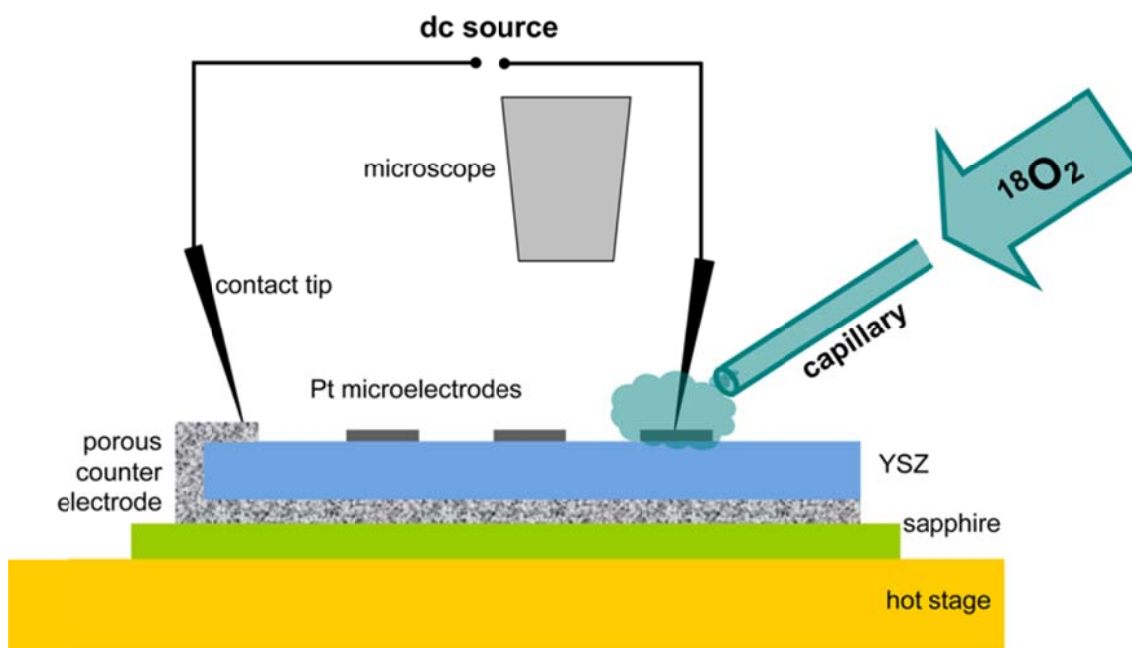


Figure 11: Sketch of the setup used for ^{18}O incorporation experiments. The thickness of the YSZ was 0.5 mm; the total thickness of the samples (YSZ + counter electrode + sapphire) was in the range of 1 mm.

ambient air to charge the electrochemical double layer capacitor of the microelectrode. After this equilibration period $^{18}\text{O}_2$ was provided to the polarized electrode for 600 s with a gas flow rate of about 1.5 ml/min. The time was chosen such that the integrated charge flow was sufficiently high to yield an easily detectable ^{18}O signal. Only in case of the highest polarization (-2.50 V) the exposure time was reduced to 300 s due to a significantly higher current. After the incorporation procedure the contact was removed from the electrode and the sample was quenched to room temperature by removing it from the hot stage and putting it onto a metal block.

2.3.2 Two-point impedance measurements with dc bias

To investigate the influence of cathodic polarization on the electrochemical properties of the platinum electrodes impedance measurements were additionally carried out at different polarization voltages. Five different cathodic bias voltages were applied: -2.00 V, -2.10 V, -2.20 V, -2.25 V, and -2.50 V. These measurements were performed in the 2-wire setup in Sec. 2.2.1. The impedance analyzer was an Alpha-A High

Performance Frequency Analyzer with ZG2 test interface. The frequency range of the impedance measurements was between 1 MHz and 50 mHz with 5 frequency points per decade resolution; the ac voltage was 0.01 V (rms).

2.4 ToF-SIMS measurements

The ToF-SIMS measurements were done on a TOF.SIMS⁵ instrument (ION-TOF, Germany). 2D element distribution images were recorded with a measuring mode commonly called “burst alignment mode” (Bi_1^+ primary ions, 25 keV beam energy, 200 nm beam diameter) with 120 nsec pulse width. The measurement raster was 512×512 pixels per area-scan in case of $200 \mu\text{m} \times 200 \mu\text{m}$ images and 256×256 pixels per area-scan in case of $30 \mu\text{m} \times 30 \mu\text{m}$ images. Depth profiles were acquired by sequential sputtering with 2 keV Cs^+ ions ($500 \times 500 \mu\text{m}^2$ area, ~ 170 nA sputter beam current). For charge compensation a low energy electron shower (20 V) was employed. The determination of the oxygen isotope ratios was done by integration of the $^{18}\text{O}/^{16}\text{O}$ signal intensities within an increment of 20 nsec and the single peak correction procedure suggested in Ref. [96] was applied to minimize the error due to dead time effects of the detection system.

On each electrode used in a tracer incorporation experiment two subsequent ToF-SIMS measurements were carried out. A first one was performed with the Pt microelectrode still remaining on the YSZ and a second measurement followed after removing the Pt thin film electrode by wet chemical etching in hot nitrohydrochloric acid. In addition, measurements with focus on positive secondary ions were performed to obtain information on the distribution of typical contaminants such as Si and alkali earth elements on the surface of YSZ.

3 Results of Sample Characterization

3.1 Scanning electron microscopy

3.1.1 High temperature deposited Pt films

Fig. 12 shows scanning electron microscopy (SEM) images of the Pt microelectrodes on a YSZ single crystal. The somewhat wavy edge of the 100 μm electrode observable in Fig. 12b is caused by the harsh chemical etching process during electrode preparation; the central hole is a result of the contact procedure. The tightness of the electrodes was checked by optical microscopy as well as SEM and Fig. 12c demonstrates that only grain boundaries but no pores are visible. Only during measurements at 950 $^{\circ}\text{C}$ the formation of several pinholes was observed (cf. Fig. 12b). Hence, the temperature range for electrochemical investigations was limited to temperatures below 900 $^{\circ}\text{C}$.

In Fig. 13a a SEM image of the rectangular shaped Pt microelectrodes, which were used in ^{18}O tracer experiments, is shown. To obtain the highest possible information content in lateral tracer profiles, only the electrodes with the straightest edges were used for ^{18}O incorporation experiments. Ion beam etching would lead to sharper edges but easily damages the surface-near region of YSZ and could thus potentially distort the electrochemical incorporation of oxygen at the TPB and on the free YSZ surface. Apart from very few pinholes (with diameters in the range of micrometers) the Pt thin films were dense which was tested by means of higher magnified SEM images – see Fig. 13b.

The thin film electrodes were also characterized by X-ray diffraction (XRD) – cf. Sec. 3.2.1. The diffraction patterns in Fig. 15 show that almost solely reflexes corresponding to Pt (111) orientation could be detected and thus highly textured films were obtained. However, the platinum thin film electrodes were not single crystalline since

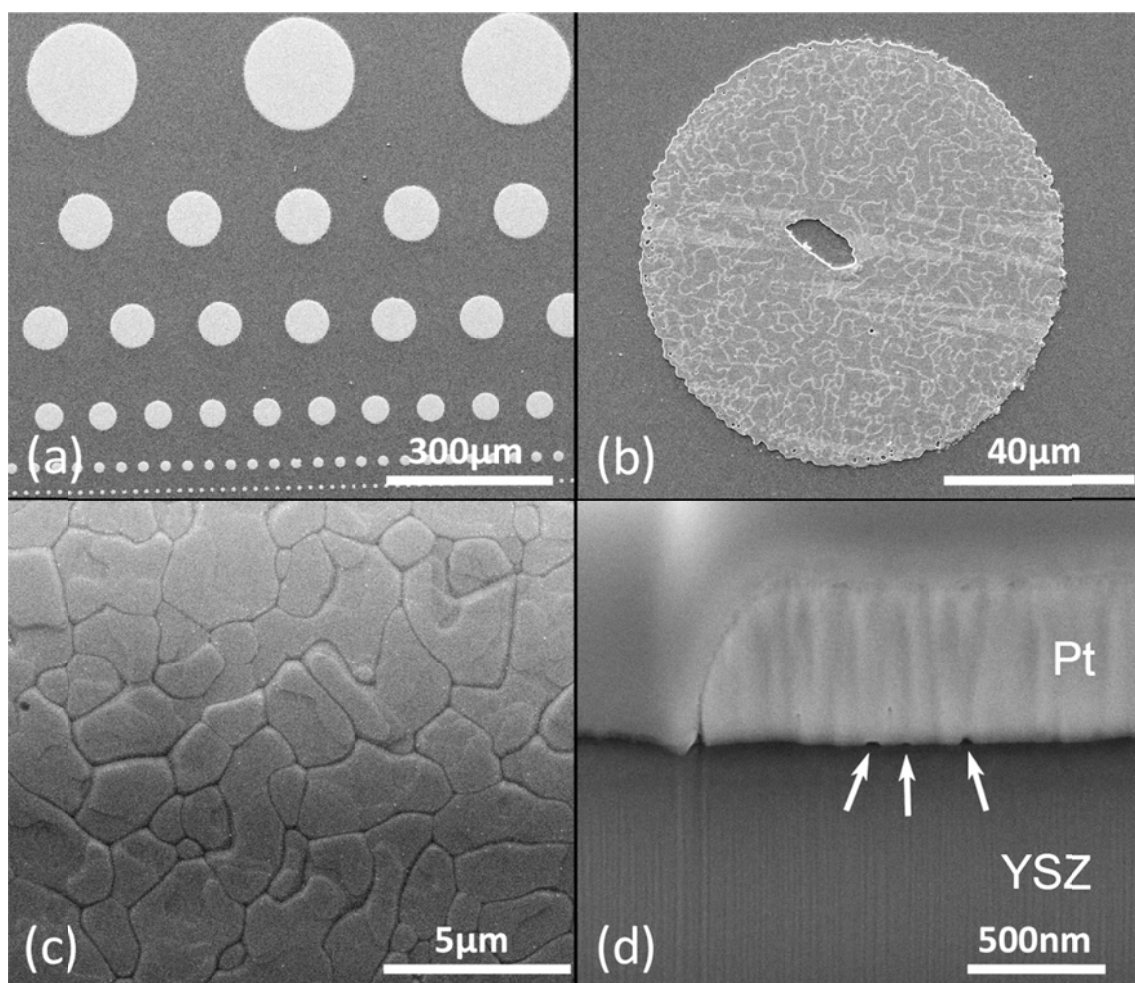


Figure 12: SEM images of high temperature deposited circular Pt thin film electrodes on YSZ. (a) Electrodes with varying diameters after preparation (48 h annealing at 700 °C). Nominal diameters (from top to bottom): 200, 100, 80, 50, 20, and 10 μm – due to experimental reasons only the four upper rows were used in electrochemical measurements. (b) 100 μm electrode after measurements at temperatures up to 950 °C; the pinholes evolved only at the highest temperature of 950 °C, the damage in the center was caused by the contact tip. (c) Higher magnification of the platinum surface after electrode preparation; grain boundaries but no pores are visible. (d) Cross-section of an electrode (before electrochemical measurements) prepared by a focused ion beam. Cavities at the interface of Pt and YSZ are marked with arrows. The vertical grooves are artifacts due to preparation.

Pt grain boundaries were clearly visible in SEM investigations (cf. Figs. 12b and c). These findings are in very good agreement with results given in Ref. [21] for Pt electrodes prepared by pulsed laser deposition.

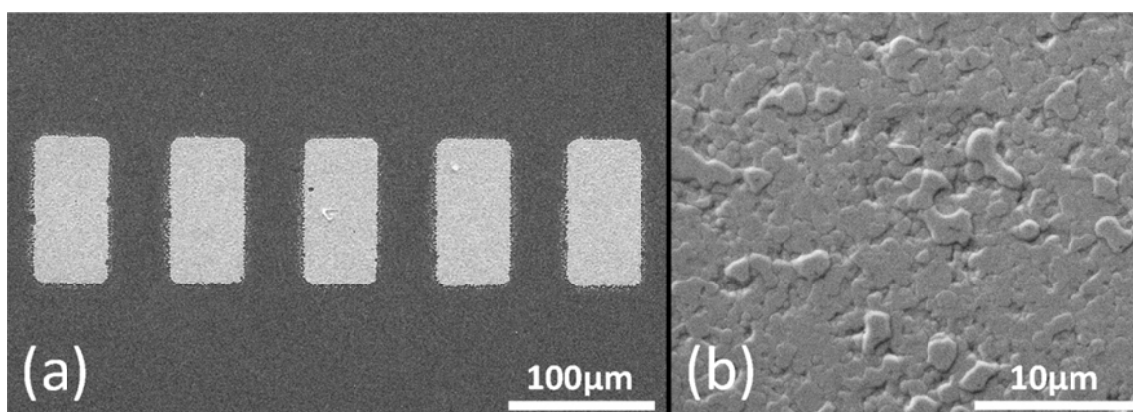


Figure 13: SEM images of the high temperature deposited Pt electrodes used in ^{18}O tracer experiments: (a) Rectangular shaped ($50 \times 100 \mu\text{m}^2$) electrodes. (b) Higher magnification of the surface of a Pt electrode in (a). Neither cracks nor pores but grain boundaries are visible.

3.1.2 Low temperature deposited Pt films

SEM micrographs of low temperature sputtered Pt thin films are shown in Fig 14. An image of the virgin Pt film (after sputter-deposition, without any thermal treatment) is given in Fig. 14a. The virgin films exhibited a very homogeneous micro-structure with an average grain size between 20 and 30 nm. No indication of pores or pinholes was found. After the first heat treatment (750°C , 2 h) a significant increase in grain size could be observed (cf. Fig. 14b). Additionally the annealing step led to the formation of bubble-like structures within the thin film (see Figs. 14d and e). They were found to be hollow since they collapsed when touched by the contact tip in electrochemical measurements (cf. Fig. 14f). Bubble formation was also observed in Ref. [49], but under anodic polarization of the Pt thin film electrodes. A possible speculation is, that the bubble formation in this case was caused by the release of oxygen from YSZ due to a slight increase in non-stoichiometry at higher temperatures ($\text{nil} \rightleftharpoons \frac{1}{2} \text{O}_2 + \text{V}_\text{O}^{\bullet\bullet} + 2\text{e}'$) [97]. However, no indication was found that the intact bubbles affected the gas tightness of the thin films and hence a noteworthy influence on geometrical properties such as electrode surface area and TPB length was excluded.

After the electrochemical experiments the thin film electrodes were again investigated by SEM to control their stability in terms of gas tightness during these measurements. In Fig. 14c the corresponding micrograph is shown. Further grain growth and some surface roughening, but again no indication for any formation of gas leakage (like pores, pinholes, or cracks) was found.

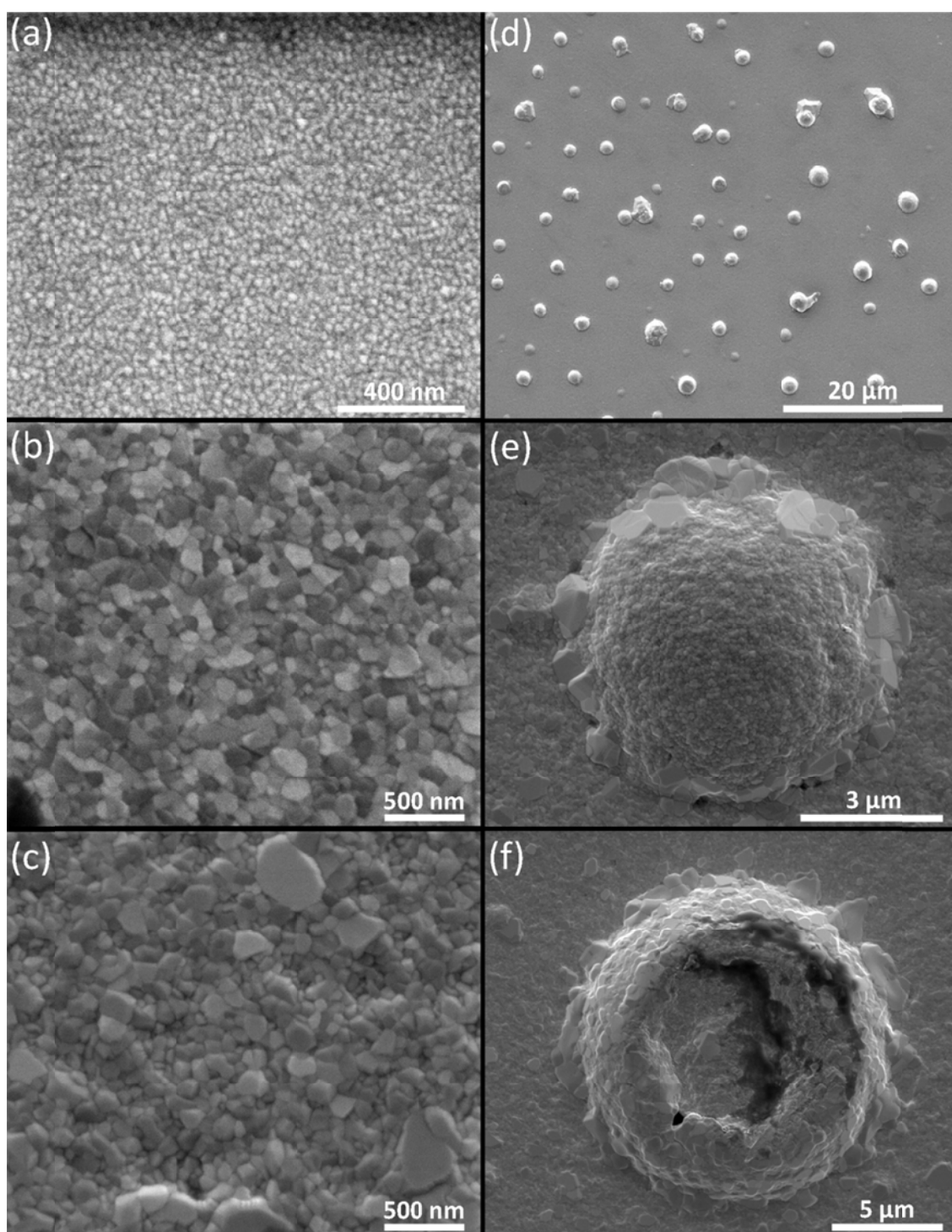


Figure 14: (a) SEM image of the virgin low temperature sputter-deposited Pt film on YSZ (100). The average crystallite size was between 20 and 30 nm. (b) Pt film after a two hour heat treatment at 750 °C. The crystallite size was increased but neither cracks nor pores were visible. (c) Pt film after electrochemical measurements. Further crystal growth and some surface roughening were obvious. (d) Lower magnification of a Pt film comparable to that in (c) indicating bubble formation. The bubbles persisted also during electrochemical experiments. (e) Higher magnification of one single bubble. (f) Collapsed bubble.

3.2 X-ray Diffraction

3.2.1 High temperature deposited Pt films

X-ray diffraction (XRD) patterns of a freshly high temperature deposited Pt thin film and of electrodes after 48 h annealing at 700 °C are shown in Fig. 15. Neglecting signals from K_{β} -radiation the platinum films almost exclusively show reflexes corresponding to YSZ (100) and Pt (111) orientation which demonstrates that highly textured films were obtained. After annealing for 48 h at 700 °C some very small additional reflexes emerged which could not be identified unambiguously.

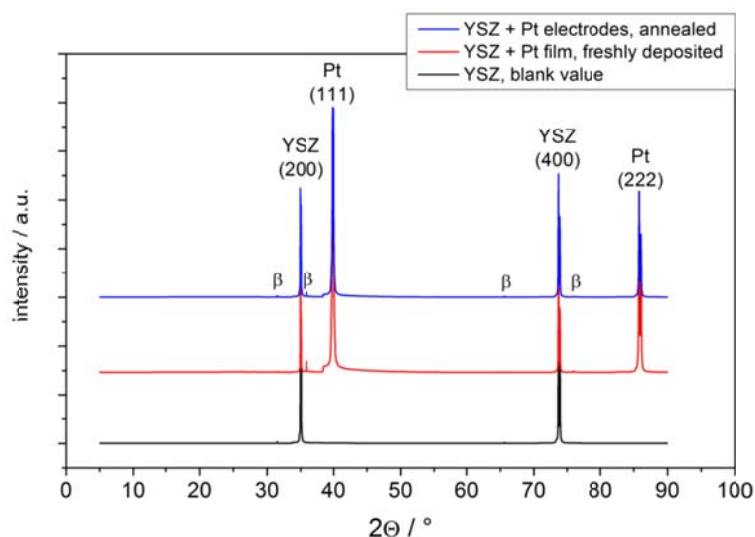


Figure 15: Diffraction patterns of Pt films/electrodes on a YSZ (100) substrate directly after high temperature sputtering and after annealing for 48 h at 700 °C. Neglecting K_{β} reflexes almost only signals corresponding to Pt (111) and YSZ (100) orientation were detected. The blank measurement was performed on an identical YSZ single crystal without platinum electrodes.

3.2.2 Low temperature deposited Pt films

Results of XRD measurements on low temperature sputter-deposited Pt films are depicted in Fig. 16a where a comparison of measured data with the Rietveld calcula-

tions (software: Topas 4.2) for a virgin sample is shown. On this Pt thin film without any thermal treatment primarily reflexes corresponding to YSZ (100) and Pt (111) orientation could be observed. In addition a very weak signal according to Pt (100) was found. In Fig. 16b the diffraction pattern of the Pt film on YSZ after an annealing step (2 hours at 750 °C) together with its Rietveld refinement is shown. On these films the Pt (100) reflex could not be detected, the Pt thin films were exclusively (111) textured. Obviously the (100) oriented Pt was transformed into (111) oriented Pt during the annealing step. The peak heights as well as the peak integrals obtained on the virgin films were significantly lower than in case of annealed films. This might possibly be attributed to a slight inclination of the Pt columns in the film right after sputter-deposition [98]. In Fig. 17b simulated diffraction patterns of ideal (111) textured Pt (upper orange curve) and slightly inclined Pt (111) (lower light blue curve) are compared. The lattice parameters and the crystallite sizes in this simulation were the same as in case of the real samples. Obviously the simulation obtained a comparable intensity ratio of the two Pt species as the measurements (compare Fig. 19a and b). In addition to the (111)-textured Pt, traces of an unknown impurity phase were found on the annealed Pt film (with an intensity being orders of magnitude smaller than the strongest Pt reflexes). In the Rietveld analysis the impurity phase refined with strongly distorted textured copper, which might be an impurity of the sputter target. However, due to the very small amount of this impurity its nature could not be identified unambiguously. The crystallite sizes (Lorentzian) as well as the lattice parameters of the platinum films obtained by the refinement are summarized in Tab. 2. The crystallite sizes were in good agreement with the results from SEM investigations (cf. Fig. 14). The somewhat larger lattice parameter of the virgin Pt thin film might be attributed to internal strain caused by the small crystallites. Rietveld calculations indeed yielded a significantly higher strain for the Pt films without a thermal treatment.

Table 2: Crystallite sizes and Pt lattice parameters of low temperature sputtered and annealed platinum films.

thermal treatment	crystallite size [nm]	lattice parameter [Å]
none	40	3.936
2 h at 750 °C	160	3.922

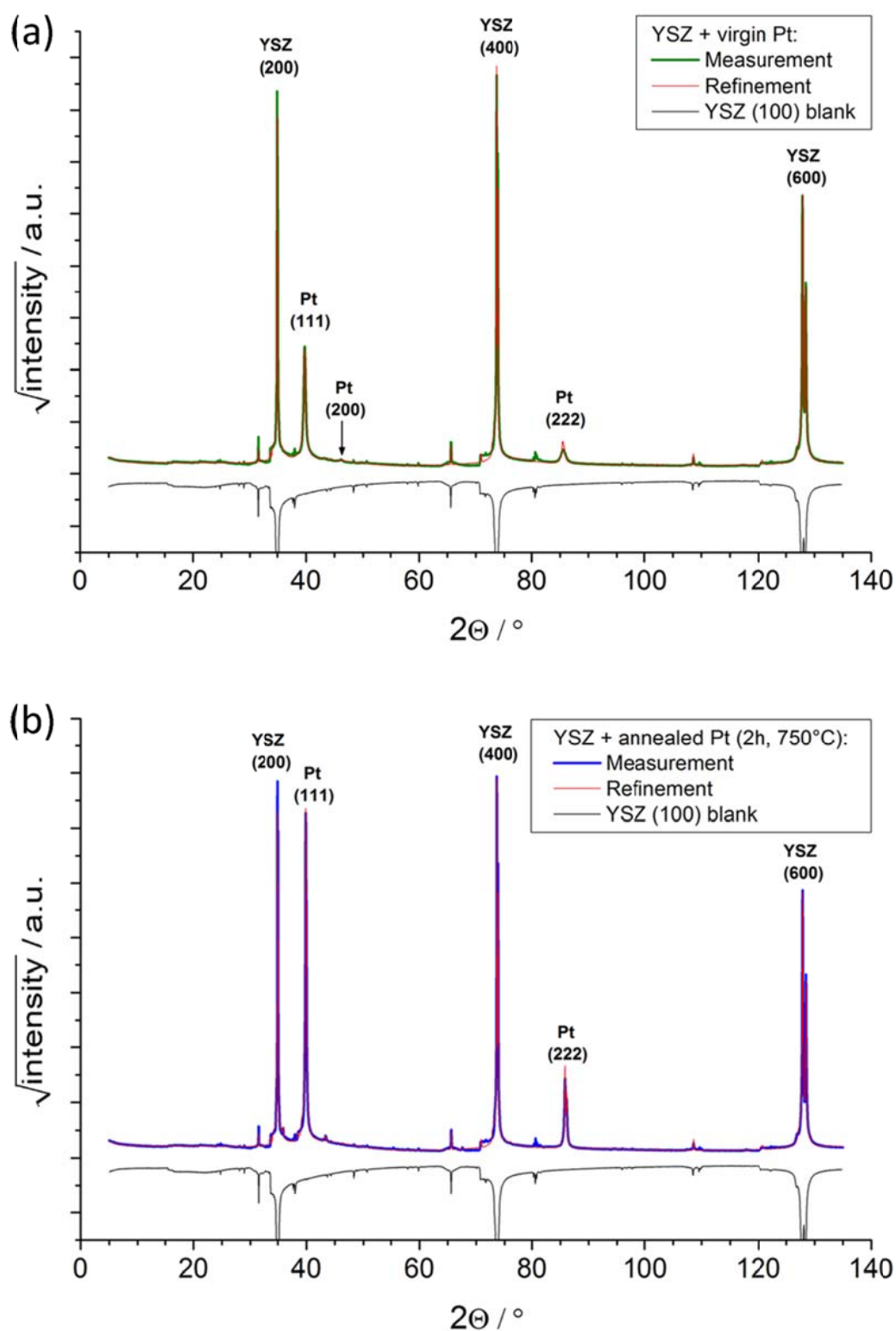


Figure 16: (a) Diffraction pattern of the virgin low temperature deposited Pt thin film (without any thermal treatment) and the corresponding Rietveld refinement as well as the pattern of the YSZ blank (mirrored). (b) Diffraction pattern of the annealed Pt film together with its Rietveld refinement and the pattern of the blank YSZ (mirrored).

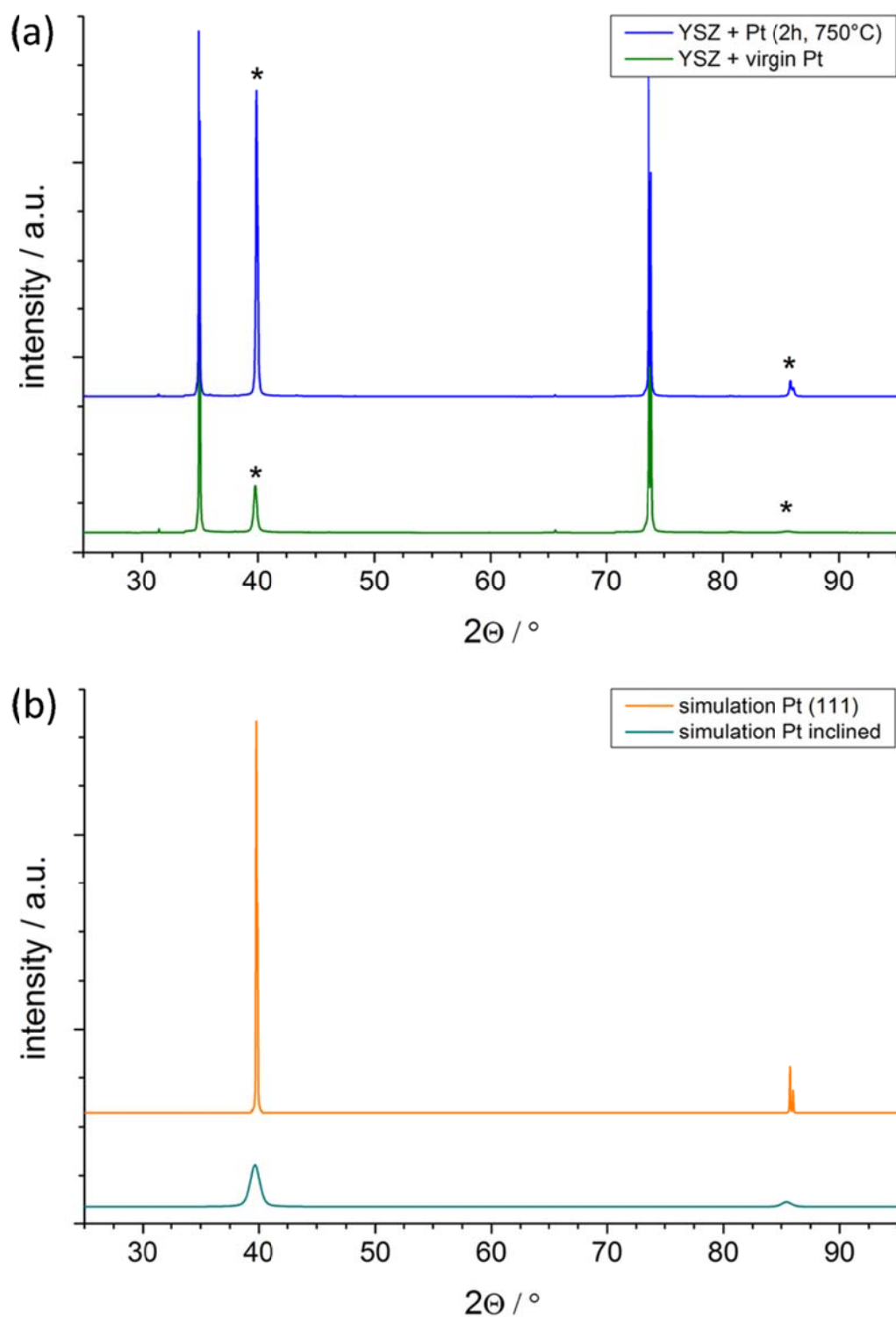


Figure 17: (a) Comparison of the measurements shown in Fig. 16. The reflexes corresponding to the Pt thin film are indicated by an asterisk. (b) Comparison of two simulated diffraction patterns: The simulation of an ideal Pt (111) diffraction pattern is shown by the upper orange graph, whereas the lower light blue graph depicts the simulated pattern of slightly inclined Pt (111).

4 Results and Discussion of Impedance Measurements

4.1 Measurements on high temperature deposited electrodes

The electrochemical impedance measurements on high temperature prepared electrodes were done in the two-wire setup described in Sec. 2.2.1. In order to keep irreversible changes of the microelectrodes (e.g. morphological changes or accumulation of impurities which may be caused by a thermovoltage – cf. Fig. 6) as small as possible, only one impedance spectrum was recorded on each microelectrode. Rather, spectra on at least five different electrodes of the same size were measured at one set temperature for testing reproducibility and obtaining a reasonable statistics. The nominal temperature of the heating stage was varied between 700 and 900 °C and true temperatures were determined from the measured YSZ bulk resistance (R_{YSZ}) by the algorithm described in Sec. 4.1.1. The temperature range was not only investigated once, but thermal cycling was performed to test the electrochemical stability of the electrodes. The polarization resistance did not show significant changes even after measurements at 900 °C indicating acceptable geometrical stability of the electrodes (cf. Sec. 4.1.2).

Impedance spectra measured on microelectrodes with a diameter of 100 μm are shown in Fig. 18a for five different temperatures. Each spectrum consists of at least three characteristic parts: a high frequency axis intercept, a high frequency shoulder (both visible in the zoom insert below), and a huge semicircle in the lower frequency range. The elementary process responsible for the resistance of this low frequency arc is the rate determining step of the electrochemical oxygen exchange reaction. Parameterization of the impedance spectra was carried out by the complex nonlinear least square (CNLS) fit program Z-View (Scribner, USA). The equivalent circuit used to fit

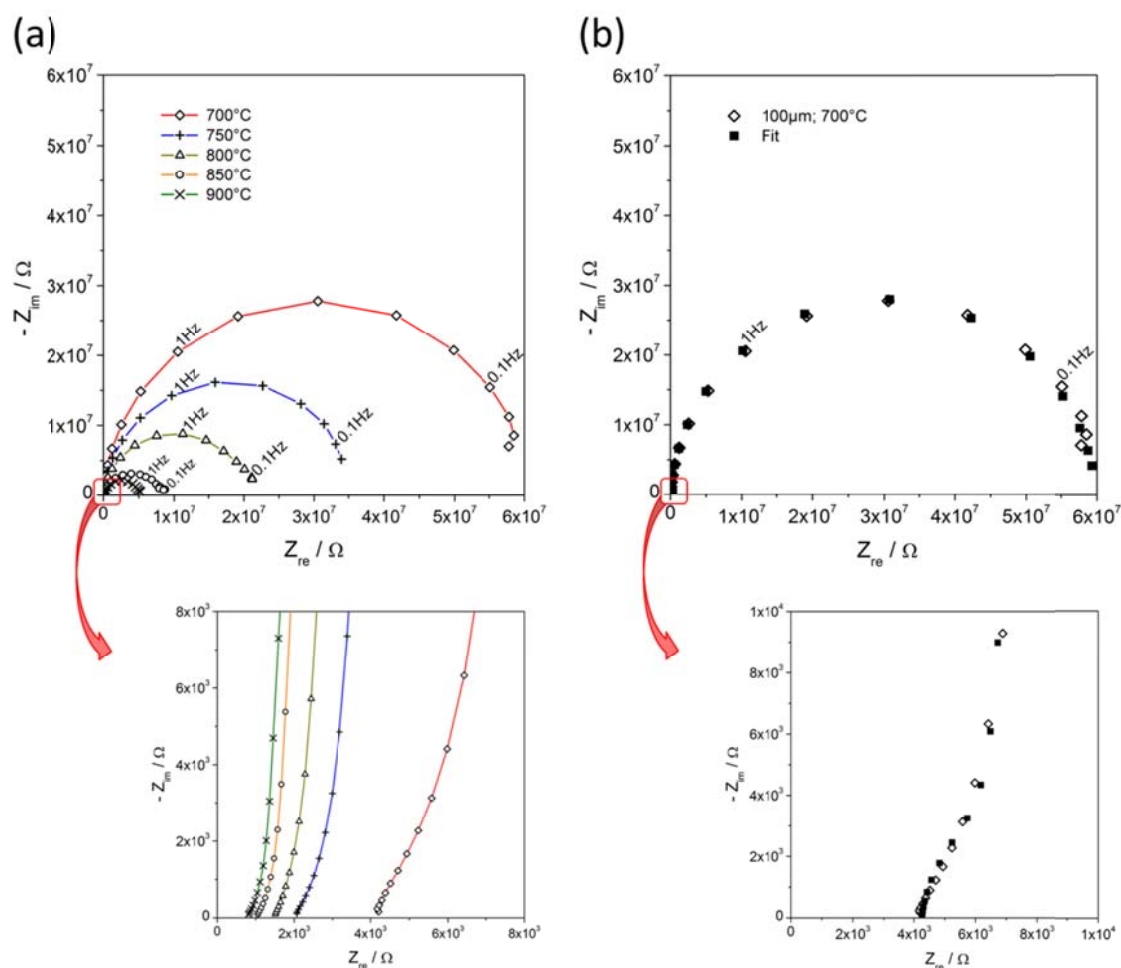


Figure 18: (a) Impedance spectra (Nyquist plots) measured on $100\ \mu\text{m}$ electrodes at five different set temperatures. The magnification below shows the high frequency part of the spectra and visualizes the axis intercept due to the electrolyte spreading resistance and a shoulder-like feature. (b) Comparison of the $700\ \text{°C}$ spectrum from (a) with the fit result using the equivalent circuit in Fig. 19 (filled symbols).

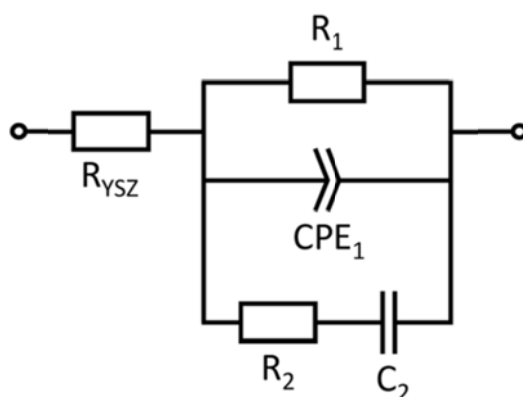


Figure 19: Equivalent circuit used for the CNLS fits of impedance measurements between 700 and $900\ \text{°C}$ on high temperature deposited Pt microelectrodes. The fit elements are explained throughout the text (cf. Sec. 4.1.3).

the experimental data is shown in Fig. 19 (CPE denotes a constant phase element) and will be discussed in Sec. 4.1.3. It allowed a good CNLS-fit to the measured data as can be seen in Fig. 18b. The physical meaning of the elements and the reason for not using two serial R-CPE elements will also be discussed in Sec. 4.1.3. Based on further experiments, particularly dc current-voltage measurements and the related mechanistic conclusions, a slightly refined circuit will be suggested and tested in Sec. 6. This circuit can even avoid the minor deviations between measurement and fit data visible in Fig. 18b at medium and higher frequencies. However, it does not affect the analysis and conclusions drawn in this section.

4.1.1 The bulk resistance of YSZ

In earlier studies with oxide microelectrodes on YSZ [24, 31] it was shown, that the high frequency intercept (denoted R_{YSZ} in the equivalent circuit) is the spreading resistance of ion conduction in YSZ (provided that the electronic conductivity in the electrode is sufficiently high) [74]. This bulk resistance between a circular microelectrode and an extended counter electrode is related to the ionic conductivity σ_{ion} by

$$\sigma_{\text{ion}} = \frac{1}{2d_{\text{ME}}R_{\text{YSZ}}} \quad (7)$$

where d_{ME} denotes the microelectrodes diameter [99-101]. Since the ionic conductivity of the YSZ single crystals was also determined in a conventional setup with symmetrical extended Pt electrodes (cf. Fig. 20), R_{YSZ} and Eq. 7 can be used to determine the true temperature of each microelectrode. The deviation of the true microelectrode temperature from the set temperature of the heating stage had two reasons. First, the heating of the sample was performed in an asymmetric way as can be seen in Fig. 4a. As a consequence a temperature gradient from the bottom to the top of the sample can be expected. Second, the contacted microelectrode is cooled by the tip which is clamped at much lower temperature. Owing to its "large" volume, compared to the microelectrodes (cf. Fig 3b), the contact needle acts as a heat sink and leads to a decrease of the effective electrode temperature. According to the conventional impedance measure-

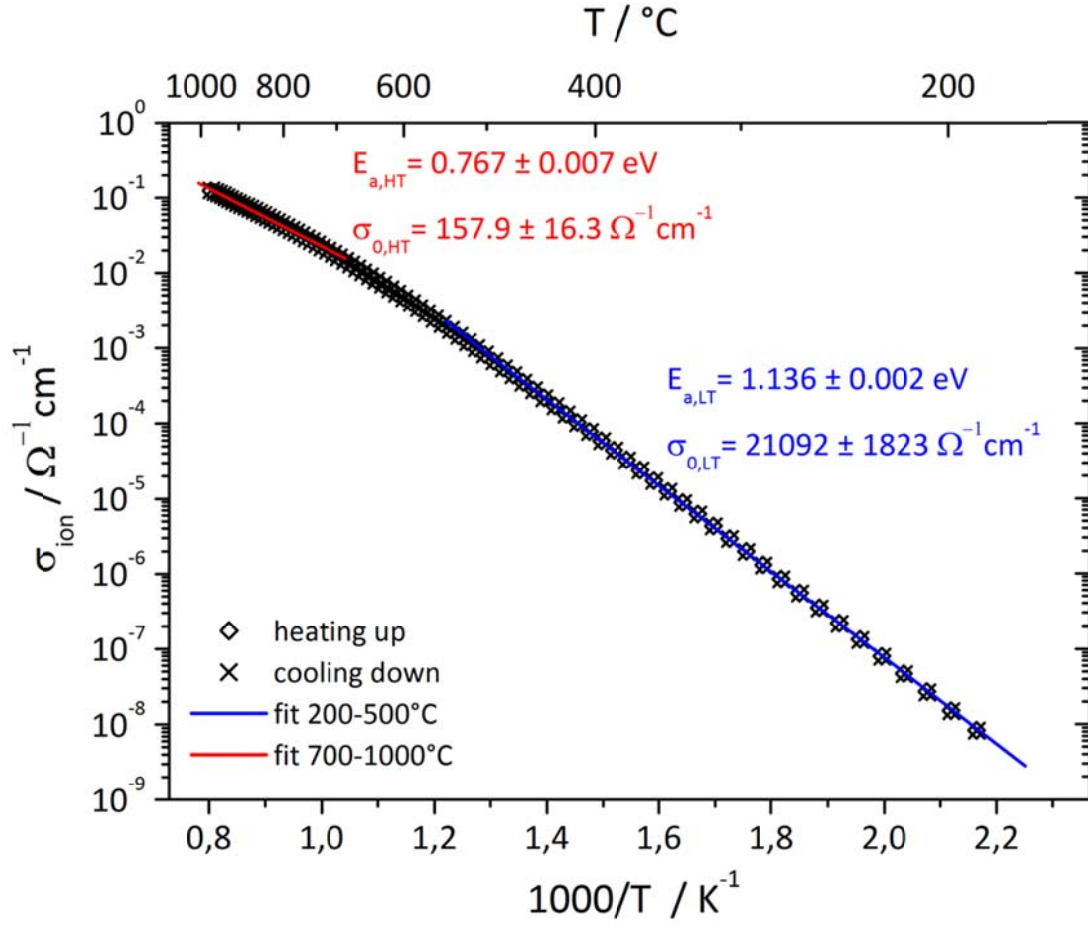


Figure 20: Arrhenius plot of the ionic conductivity of an YSZ (100) single crystal. The measurement was performed with “conventional” i.e. extended, symmetric Pt electrodes. The red line represents an Arrhenius fit of the linear region at high temperatures (denoted HT) and the blue line represents an Arrhenius fit of the linear region at low temperatures. The fit results ($E_{a,HT}$ and $\sigma_{0,HT}$ as well as $E_{a,LT}$ and $\sigma_{0,LT}$) are given within the figure and the activation energy values are in acceptable agreement with data from literature [97, 102].

ments in the relevant temperature range of 700 – 1000 °C (red fit line in Fig. 20) the ionic conductivity σ_{ion} of the single crystals is given by

$$\sigma_{\text{ion}} = \sigma_0 \cdot e^{-\frac{E_a}{k_B T}} \quad (8)$$

with σ_0 and activation energy E_a being $157.9 \pm 16.3 \Omega^{-1} \text{cm}^{-1}$ and $0.767 \pm 0.007 \text{ eV}$, respectively. Combining Eqs. 7 and 8 leads to the true electrode temperature

$$T = \frac{E_a}{k_B \cdot \ln(\sigma_0 \cdot 2d_{ME} R_{YSZ})}. \quad (9)$$

In the following analysis of the experimental data the true temperature of each measured microelectrode was calculated from Eq. 9. Typical differences between these corrected temperatures and the set temperature were between almost 0 °C (200 μm) and about 60 °C (50 μm). However, despite microelectrode measurements only depend on a small volume of YSZ, their “field of vision” still contains a slight temperature gradient. Hence, the values of σ_{ion} and the effective electrode temperature are averaged values over the YSZ volume probed by the microelectrode. Therefore, this temperature correction (Eq. 9) is still more an estimation than an exact calculation. As already mentioned, owing to the temperature gradient in the sample a thermovoltage is generated between counter- and microelectrode (cf. Fig. 6). Effects of this thermovoltage on the impedance measurements will be discussed in Sec. 4.1.3.1.

4.1.2 Parameterization of the electrode impedance

Since the YSZ electrolyte was single crystalline, grain boundaries can be excluded as a source of any impedance feature and the high frequency shoulder as well as the predominant semicircle have to be related to electrode processes. Owing to the very large difference between the size of a microelectrode and that of the counter electrode, the entire electrode impedance was attributed to the Pt microelectrode [75] and the data presented in the following also support this interpretation. The main focus of the present work is the analysis of the geometry dependence of all fit elements of this electrode impedance. In principle this only requires direct comparison of fit parameters obtained on different electrode sizes at a given temperature. However, the cooling effect discussed above and thus the deviation of the true electrode temperature from the set temperature depends on the microelectrode size. Hence, a simple comparison of data obtained for one set temperature was not reasonable. To cope with this problem the comparison of electrode fit parameters was carried out over a wider temperature range. The fit data were plotted in Arrhenius diagrams and data points of each electrode size were correlated by linear regression. The resulting regression lines were then

used for analyzing the geometry dependence of each fit element. In Figs. 21, 22, 23, and 24 the fit results (i.e. R_1 , R_2 , C_1 , and C_2) are plotted as raw data (a), normalized to the TPB length (b) and normalized to the surface area (c), respectively. Since specific (geometry-independent) values should result for each parameter, such diagrams directly show which parameter is related to the TPB length and which one is related to the area of the microelectrodes: In the appropriate plot all regression lines fall together and thus reflect the true geometry dependence.

Please note: The actual diameters (d_{meas}) of the electrodes were determined from optical micrographs by means of length measuring software (Olympus, Germany) and turned out to be slightly smaller than the nominal values defined by the photolithographic mask (200, 100, 80, and 50 μm). Moreover, the wavy edge of the electrodes (due to the etching process cf. Sec. 3.1.1) lead to an increase of the true TPB length by a factor of about 1.2 which was determined from SEM-images by attaching a thread along the electrode edge and measuring its length. The exact results of electrode area A_{ME} and TPB length L_{TPB} are listed in Tab. 3. For the sake of simplicity nominal sizes are used throughout the text.

Table 3: Geometrical properties of the circular microelectrodes used.

$d_{\text{ME,set}} [\mu\text{m}]$	$d_{\text{ME,meas}} [\mu\text{m}]$	Circumference [μm]	$L_{\text{TPB}} [\text{cm}]$	$A_{\text{ME}} [\text{cm}^2]$
200	192 ± 2	603	$7.24 \cdot 10^{-2}$	$2.90 \cdot 10^{-4}$
100	91 ± 3	286	$3.43 \cdot 10^{-2}$	$6.5 \cdot 10^{-5}$
80	70 ± 2	220	$2.64 \cdot 10^{-2}$	$3.9 \cdot 10^{-5}$
50	41 ± 2	129	$1.55 \cdot 10^{-2}$	$1.3 \cdot 10^{-5}$

4.1.2.1 Resistive electrode processes

Data analysis of the polarization resistance caused by the rate determining step of oxygen exchange (i.e. resistance R_1) is shown in Fig. 21 where the inverse of R_1 (i.e. the conductance) is logarithmically plotted versus $1000/T$. Each point in the diagram represents the arithmetic mean value of at least five individual measurements on

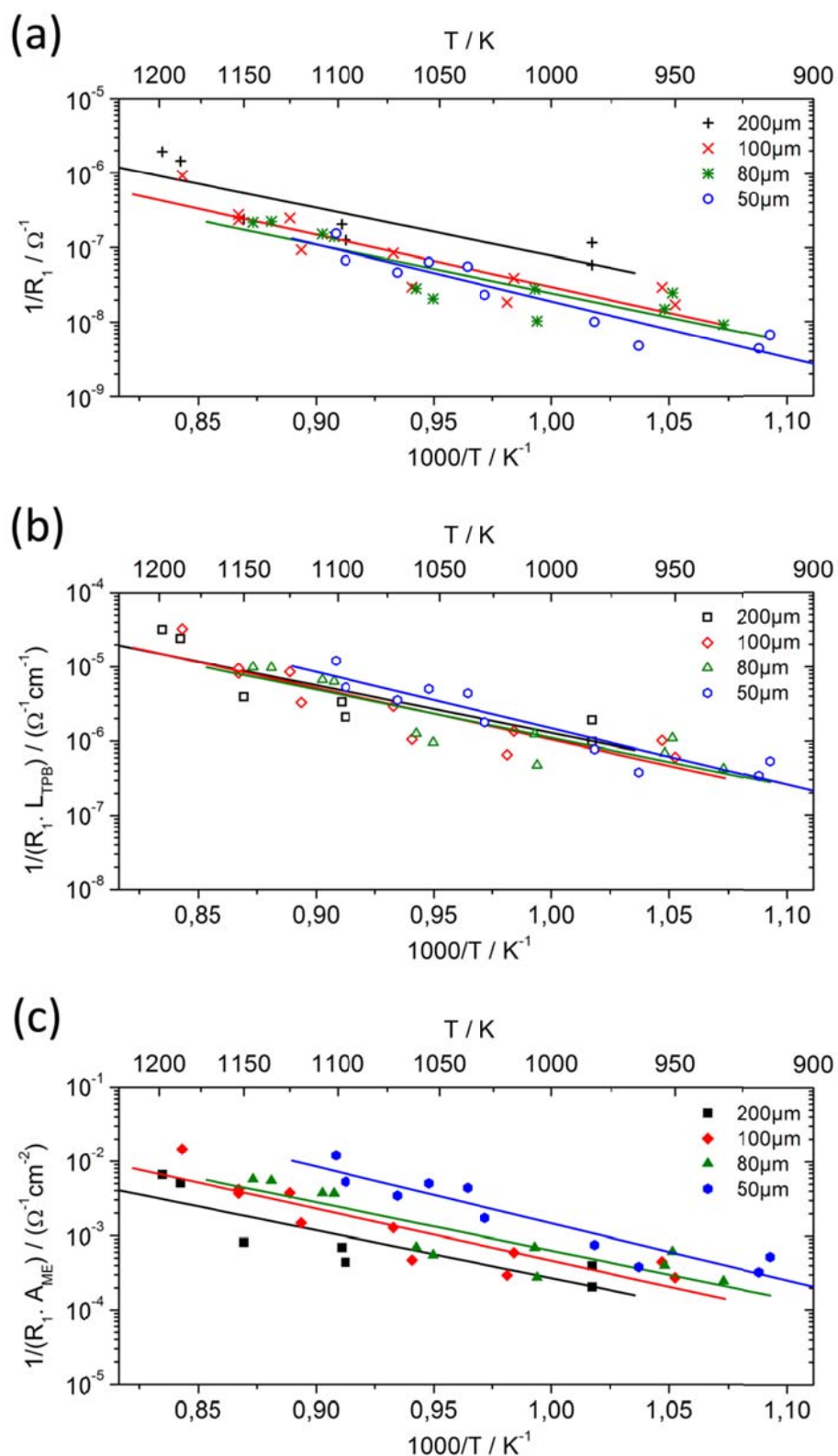


Figure 21: Arrhenius plots of the resistor R_s representing the rate determining step. In (a) the raw data is given as $1/R_s$ whereas in (b) and (c) TPB length and area-related data are plotted, respectively. Obviously in (b) all lines fall together and a specific electrode "conductivity" results.

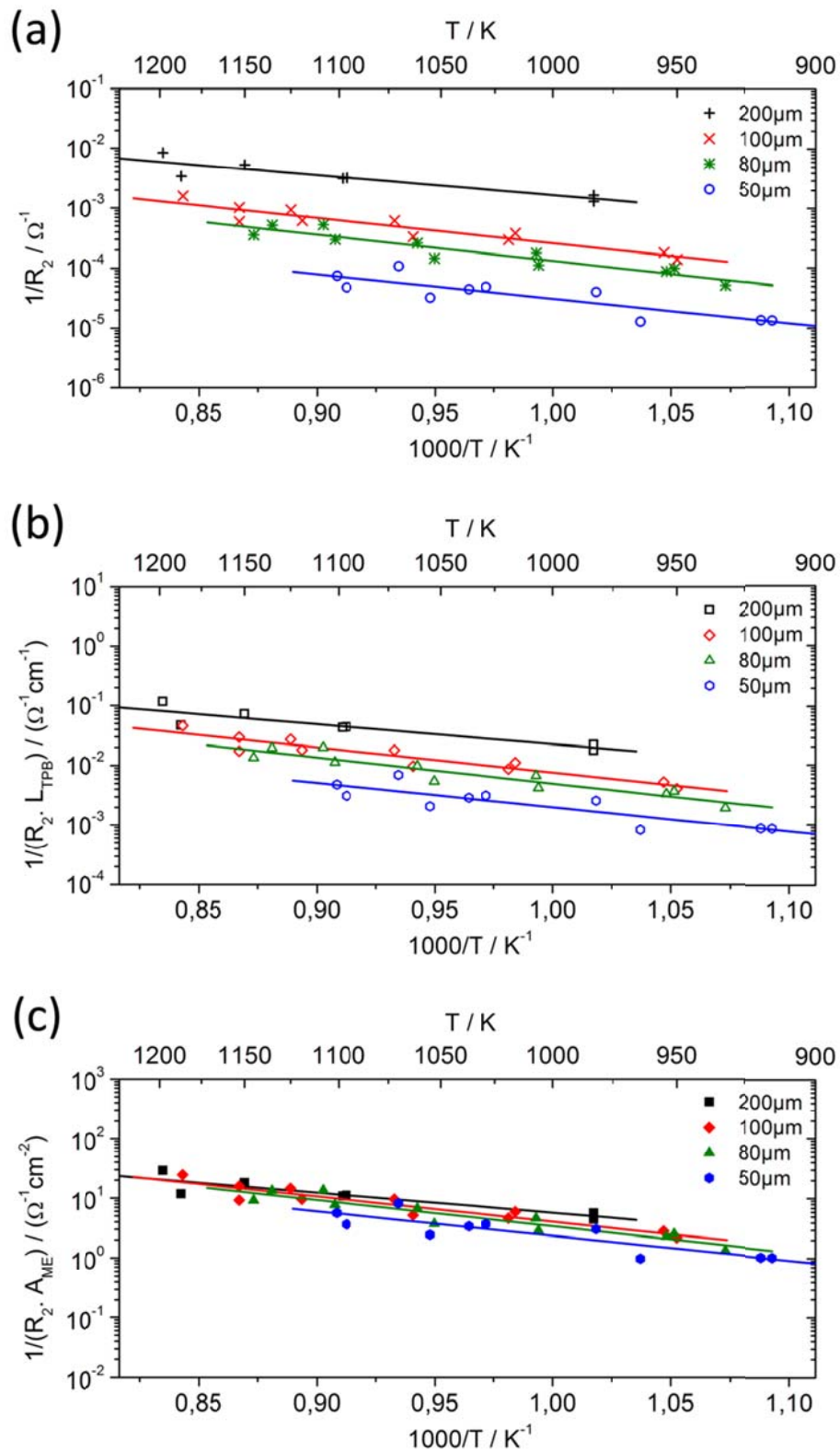


Figure 22: Arrhenius plots of the resistor R_2 which corresponds to the high frequency shoulder in the Nyquist Plot. (a) Raw data, (b) TPB length related values, (c) area-related values; Contrary to R_1 (Fig. 21) the area-related lines fall together.

different electrodes at one set temperature. As expected, larger electrodes exhibit a higher conductance than smaller ones (cf. Fig. 21a). The plots resulting after normalization to the TPB length and the electrode area are given in Figs. 21b and c, respectively. From these diagrams a clear conclusion can be drawn regarding the geometrical dependence of R_1 : Only regression lines of TPB length related conductances fall together. At 700 °C the rate determining step causes a TPB-specific conductance (electrochemical “conductivity”) of $6.6 \pm 0.9 \cdot 10^{-7} \Omega^{-1}\text{cm}^{-1}$. The activation energy of this process was calculated from the linear slopes in Arrhenius plots and amounts to 1.36 ± 0.11 eV. The same analysis procedure was applied to resistance R_2 which represents the high frequency shoulder in the impedance spectra. In contrast to R_1 this parameter shows an area-dependent behavior (see Figs. 22a, b, and c). An activation energy of 0.79 ± 0.09 eV was determined for the underlying process. The results of both resistive processes are summarized in Tab. 4. Reasons why processes at the counter electrode could be excluded as origin of the shoulder-like feature should be given in the following: Not only the strong relation between microelectrode area and R_2 or C_2 , but also the very small absolute value of C_2 strongly supports the assumption that the shoulder in the spectrum indeed reflects microelectrode rather than counter electrode properties. Further the characteristic frequency f^* of the shoulder-like structure was determined to be in the order of 10 kHz. In contrast to that f^* values obtained on a sample in a conventional setup with symmetrical extended Ag paste electrodes were in the range of 50 Hz at similar temperatures.

In order to further illustrate the geometry dependence of the rate determining step, the inverse of R_1 was also plotted versus the TPB length (Fig. 23). In case of a TPB-related process this kind of plot should display a linear relation for each temperature with regression lines intersecting the origin. The data points in this plot were calculated from the Arrhenius-fit lines in Fig. 21a (isothermal cuts through the diagram) in order to avoid errors caused by temperature differences of differently sized electrodes (see Sec. 4.1.1). For temperatures from 700 to 800 °C the extrapolations of the linear regression lines in Fig. 23 indeed almost exactly meet the origin. A slight deviation is found for 850 °C (particularly due to the data point of the 50 μm -electrode) and significant deviation (again because of the 50 μm -electrode point) results for 900 °C. This is possibly caused by a thermovoltage due to a temperature gradient – this was already mentioned in Secs. 2.2.2 and 4.1.1. In Ref. [22] a similar geometry dependence was

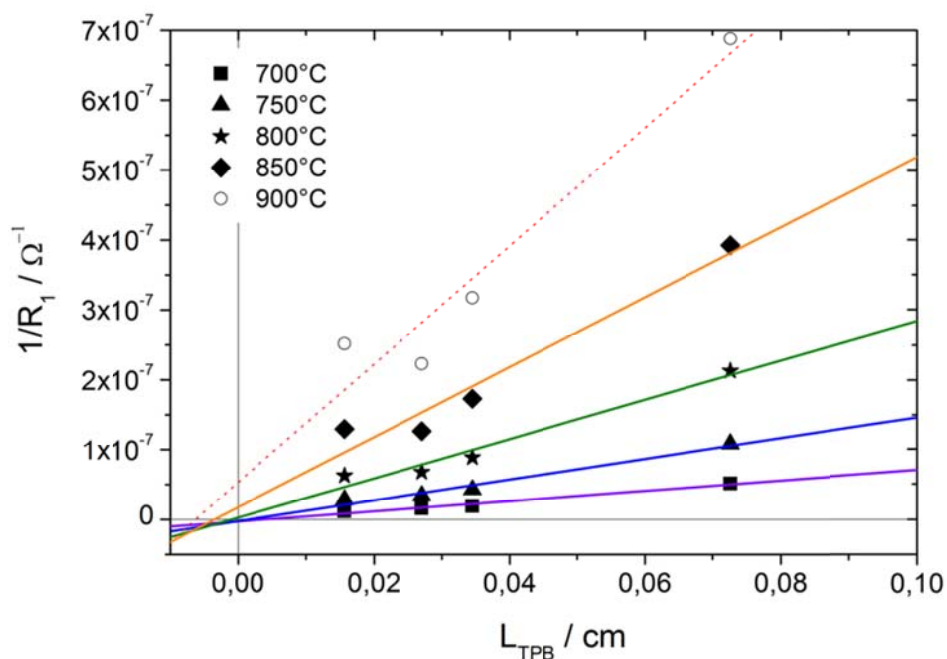


Figure 23: Inverse values of R_1 (representing the rate determining step) plotted versus the TPB length. The data points were calculated from the linear equations of the regression lines in Fig. 21a.

reported for stripe-shaped sputter-deposited Pt electrodes. However, these electrodes suffered from a large number of pores or pinholes which made data interpretation challenging: in a plot of the inverse resistance versus the TPB length an x-axis intercept of the linear regression lines resulted in this study.

4.1.2.2 Capacitances

The capacitive contributions to the impedance data are represented by two different circuit elements (cf. Fig. 19). To account for non-idealities in the behavior of capacitor one, a constant phase element (CPE) instead of an ideal capacitance was used. The complex impedance of the constant phase element Z_{CPE} is given by

$$Z_{CPE} = \frac{1}{(i \cdot \omega)^n Q_{CPE}} \quad (10)$$

where i denotes the imaginary unit, ω the angular frequency of the ac signal, and n and

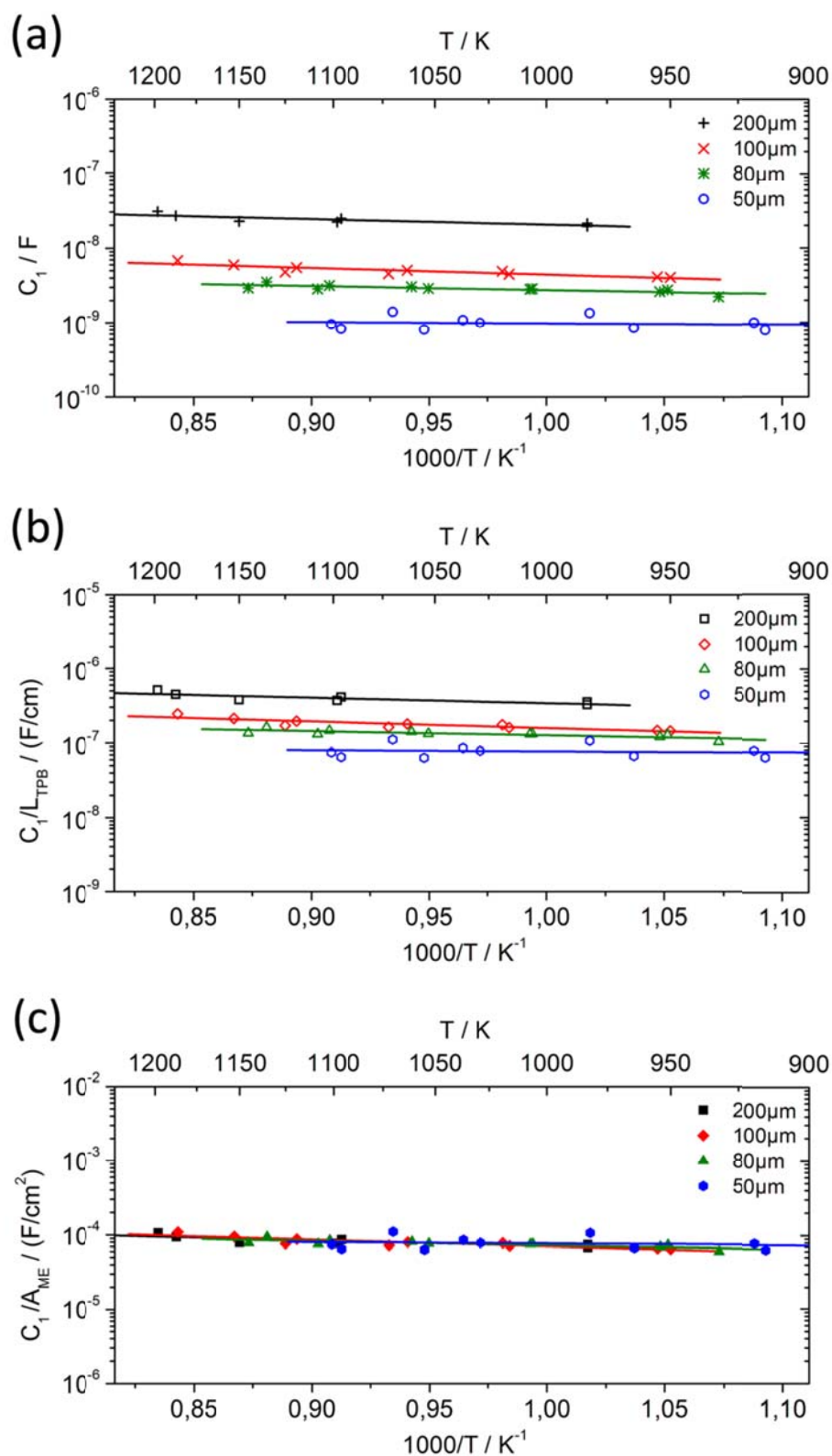


Figure 24: Arrhenius plots of the capacitance C_1 . (a) Raw data, (b) TPB length related values, (c) area-related values.

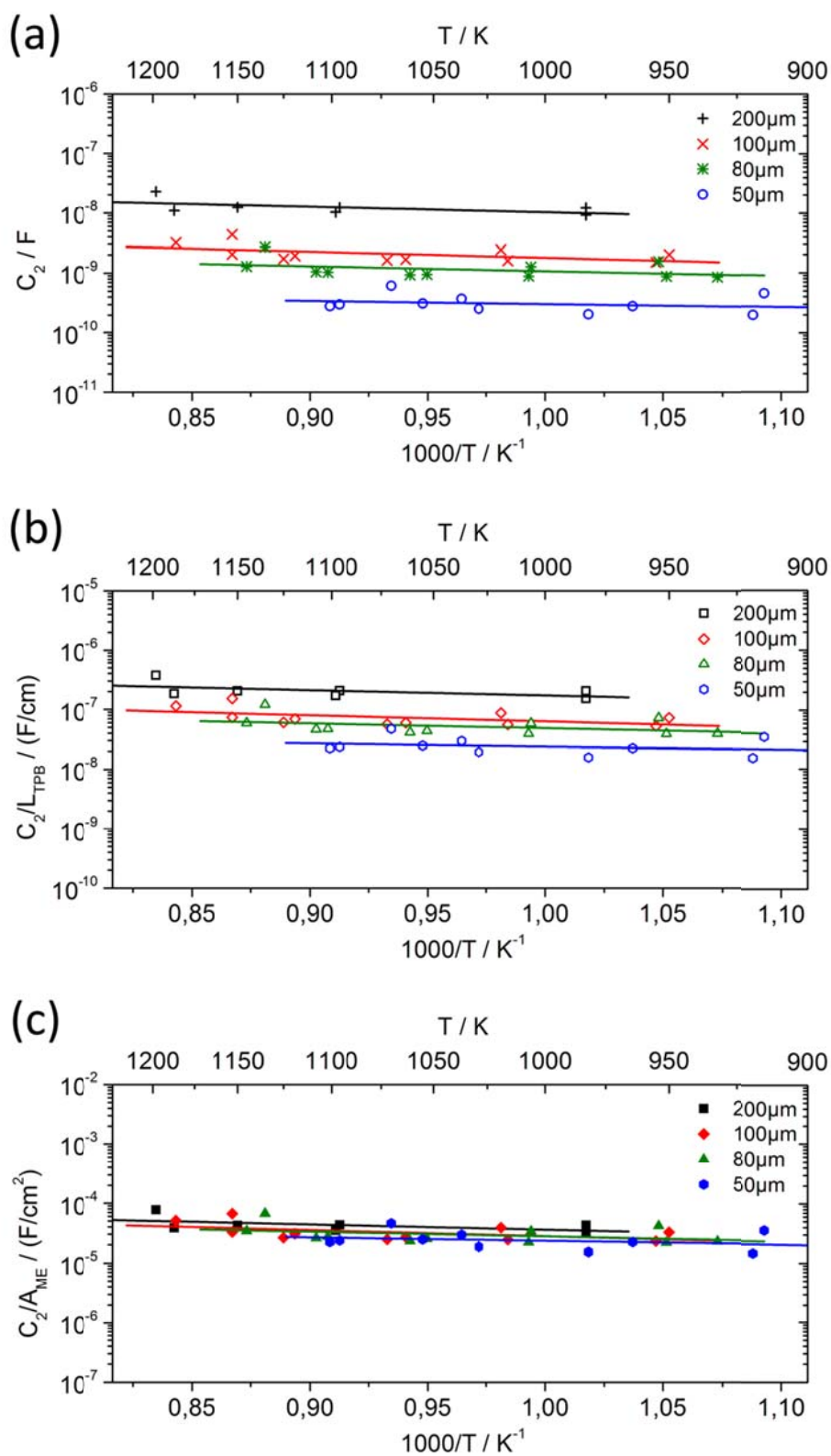


Figure 25: Arrhenius plots of parameter C_2 . (a) Raw data, (b) TPB length related values, (c) area-related values.

Q_{CPE} are fitting parameters. If n is exactly one the constant phase element represents an ideal capacitor with Q_{CPE} being equal to C . For $n < 1$ a capacitance value can be estimated from Q_{CPE} using the equation [103]

$$C = \left(R^{1-n} \cdot Q_{CPE} \right)^{\frac{1}{n}}. \quad (11)$$

Therein R denotes the resistance parallel to the constant phase element (in this case R_1 ; effects of R_2 and C_2 were neglected). Most n -values obtained from the fits in this study were between 0.7 and 1 which is a reasonable result for a non-ideal capacitor.

The geometry dependencies of C_1 and C_2 were investigated in the same manner as described for the two resistances. Both parameters showed area-related behavior as can be seen when comparing Figs. 24a-c and Figs. 25a-c. At 700 °C values of about $67 \pm 3 \mu\text{F}/\text{cm}^2$ and $27 \pm 5 \mu\text{F}/\text{cm}^2$ were obtained for C_1 and C_2 , respectively. Both capacitors only weakly depend on temperature and nominal activation energies obtained from Arrhenius-fits are given in Tab. 4.

Table 4: Summary of the results deduced from the impedance measurements

Parameter	Scales with...	Average value at 700 °C	E_a [eV]
$1/R_1$	TPB length	$6.6 \pm 0.9 \cdot 10^{-7} \Omega^{-1}\text{cm}^{-1}$	1.36 ± 0.11
$1/R_2$	surface area	$3 \pm 1 \Omega^{-1}\text{cm}^{-2}$	0.79 ± 0.09
C_1	surface area	$67 \pm 3 \mu\text{Fcm}^{-2}$	0.12 ± 0.06
C_2	surface area	$27 \pm 5 \mu\text{Fcm}^{-2}$	0.16 ± 0.04

4.1.3 Electrochemical interpretation of the fit parameters

4.1.3.1 The polarization resistance of the rate determining step – R_1

From the fact that the rate of the oxygen exchange reaction scales with the TPB length two mechanistic conclusions can be drawn. It evidences that O_2 , when being reduced on Pt|YSZ, indeed takes the surface path on its way from the gas phase into

the electrolyte; a dominating contribution via the bulk path through platinum would lead to a proportionality of reaction rate and area which is not observed in this temperature range. Moreover, the results show that the rate determining step is located close to the TPB. Oxygen adsorption as well as oxygen dissociation on the entire Pt surface (followed by fast diffusion to the TPB) can thus be excluded as rate limiting steps since both would lead to area-related R_t values. However, a co-limitation of adsorption or dissociation and surface diffusion with a short decay length of the corresponding impedance transmission line (of a few μm or less) would still be in accordance with the experimental facts. Moreover, any elementary electron or ion transfer step close to the TPB, including a diffusion through a possibly existing impurity phase at the TPB, can lead to the measured geometry dependence.

The conductance per TPB length of $6.6 \pm 0.9 \cdot 10^{-7} \Omega^{-1}\text{cm}^{-1}$ obtained at 700°C is in acceptable agreement with some of the values found in literature for electrodes with a thermal history comparable to the used preparation procedure [40, 41, 51]. In other studies with different electrode preparation processes, however, TPB-normalized properties differed by orders of magnitude [22, 42, 50]. This suggests that the route of sample preparation tremendously influences electrode kinetics at Pt electrodes. A similar data scattering was also reported in Ref. [104] for (La,Sr)MnO₃ electrodes. As a possible explanation the segregation of impurities to the TPB was discussed by several authors [7, 50, 54, 56, 104-106]. Despite poor accordance in the absolute value of the conductance per TPB length, the activation energy (1.36 ± 0.11 eV) is in acceptable agreement with many E_a -values found in literature (Ref. [22]: 1.37 eV, Ref. [41]: 1.66 eV, Ref. [46]: 1.32 – 1.54 eV, Ref. [50]: 1.5 eV).

4.1.3.2 The interfacial capacitor – C_1

Owing to its absolute value of $67 \pm 3 \mu\text{F}/\text{cm}^2$ at 700°C , its weak temperature dependence ($E_a = 0.12 \pm 0.06$ eV), and its position in the equivalent circuit parallel to the electrochemical reaction resistance (cf. Fig. 19), the constant phase element and hence the capacitor C_1 is attributed to the electrode|electrolyte interface. It can thus be regarded as a kind of double layer capacitance without excluding non-electrostatic contributions of the interface to this capacitor. Similar values of $100 \mu\text{F}/\text{cm}$ were measured in Ref. [41] on YSZ containing 10 mol% Y₂O₃ and interfacial capacitances between 120 and $330 \mu\text{F}/\text{cm}$ were found for YSZ with 8 mol% yttria [107, 108]. For doped ceria elec-

trolytes values of $\sim 100 \mu\text{F}/\text{cm}^2$ were reported in Ref. [48]. A detailed mechanistic understanding of such solid state “double layer” capacitors is still missing.

4.1.3.3 The capacitively blocked path – R_2+C_2

A shoulder-like feature at medium frequencies was also reported in Ref. [62]. There it was interpreted as a kind of current constriction at the TPB: Owing to its minor lateral extension the TPB in this study was assumed to act as a bottleneck for ionic current in the bulk, which may be short-circuited by the double layer capacitor. This bottleneck can lead to an additional arc with a resistor reflecting the additional current constriction in YSZ and scaling with the inverse TPB length [84]. However, the area dependence of R_2 found in the present measurements is not in accordance with this interpretation, even though the activation energy of R_2 would fit to the bulk activation energy of YSZ.

Therefore the following interpretation of the shoulder in the impedance spectra is suggested: Not only an additional serial kinetic process, but also a capacitively blocked parallel path (cf. Fig. 19) can cause an additional arc in an impedance spectrum [109]. The availability of a finite oxygen source between Pt and YSZ could give rise to such a capacitively blocked path. If this oxygen reservoir can be filled and emptied by the oxide ion flux in YSZ a serial connection of a capacitor and a resistor can be used to describe such a situation. Oxygen-filled, closed pores along the Pt|YSZ interface are one possibility leading to such a circuit. The oxygen in the pores can electrochemically exchange at the “internal” TPB of the pore and this leads to a resistance R_2 . Since the volume of the closed pores and thus the amount of oxygen stored in them is limited, any dc current is blocked by a (chemical) capacitor.

The chemical capacitance C_2 of the closed pores along the Pt|YSZ interface can be calculated from the charge Q required to modify the Galvani potential difference ϕ across the Pt|YSZ interface via a partial pressure change, i.e. by

$$C_2 = \frac{dQ}{d\phi}. \quad (12)$$

The increase or decrease of the number of oxygen molecules in the pores (dN_{O_2}) upon a voltage change $d\phi$ is connected to the amount of charge by Faradays law according to

$$dQ = ze_0 \cdot dN_{O_2} \quad (13)$$

where z denotes the number of electrons transferred when reducing one O_2 molecule. The relation between the voltage variation $d\phi$ and changes of the partial pressure of oxygen p_{O_2} is described by Nernst's equation

$$d\phi = \frac{k_B T}{ze_0} \cdot \ln \left(\frac{p_{O_2} + dp_{O_2}}{p_{O_2}} \right). \quad (14)$$

Linearization by first-order Taylor series approximation – i.e. $\ln \left(\frac{p_{O_2} + dp_{O_2}}{p_{O_2}} \right) \approx \frac{dp_{O_2}}{p_{O_2}}$ – leads to

$$d\phi \approx \frac{k_B T}{ze_0} \cdot \frac{dp_{O_2}}{p_{O_2}}. \quad (15)$$

The partial pressure is connected to the number of oxygen molecules N_{O_2} via the gas law

$$p_{O_2} \cdot V_{pore} = N_{O_2} \cdot k_B T \quad (16)$$

where V_{pore} denotes the volume of the closed pores filled with oxygen. Therefore it follows

$$dN_{O_2} = N_{O_2} \cdot d\phi \cdot \frac{ze_0}{k_B T}. \quad (17)$$

Inserting Eq. 17 in 13 yields

$$dQ = (ze_0)^2 \cdot N_{O_2} \left(\frac{d\phi}{k_B T} \right). \quad (18)$$

The chemical capacitance of capacitor C_2 (Eq. 12) therefore reads

$$C_2 = \frac{(ze_0)^2}{k_B T} \cdot N_{O_2} = \left(\frac{ze_0}{k_B T} \right)^2 \cdot p_{O_2} \cdot V_{pore} \quad (19)$$

In Ref. [49] small buried cavities between Pt and YSZ single crystal were assumed to act as nucleation sites for bubble formation in dense Pt thin films. Indeed in a SEM image of an electrode cross section cavities at the Pt|YSZ interface can be observed (cf. Fig. 12d). From this image a pore density of $4 \mu\text{m}^{-2}$ and an average pore size of 60 nm was estimated. Assuming a hemispherical shape of the pores this corresponds to a total volume of $1.5 \mu\text{m}^3$ in case of an electrode with 100 μm diameter. For the measured average capacitance of $27 \pm 5 \mu\text{F}/\text{cm}^2$ and the assumption of an oxygen partial pressure inside the pores of $p_{O_2} = 1\text{bar}$, a total pore volume of $V = 7.6 \mu\text{m}^3$ results from Eq. 19 for a 100 μm electrode. This value is in reasonable agreement with the volume of $1.5 \mu\text{m}^3$ estimated from Fig. 12d. Moreover, the high ideality of C_2 (a fit using a constant phase element leads to exponents very close to one) is typical for such chemical capacitances [31]. However, the absolute values of R_2 are up to 10^4 times smaller than those of R_1 (in case of a 100 μm electrode). This would correspond to an “internal” TPB length of the Pt|YSZ interface in the range of 3 m, provided both internal and external TPB exhibit the same TPB-specific conductance. This is hardly conceivable when looking at the SEM results (cf. Sec. 3.1.1). A possible explanation for this inconsistency is the assumption of different impurity levels at the outer and the inner TPB. This then leads to different normalized reaction rates and could also explain the different activation energies found for R_1 and R_2 . Impurities such as silica are frequently discussed in literature in terms of their detrimental influence on electrode kinetics [7, 50, 54, 56, 104-106].

Oxygen being “chemisorbed” to platinum at the electrode/electrolyte interface could be another finite oxygen source between Pt and YSZ. In that case the value of $C_2 = 27 \pm 5 \mu\text{F}/\text{cm}^2$ is formally in accordance with $3.5 \cdot 10^{12}$ O atoms being “chemisorbed” per cm^2 (assuming two electrons being transferred per oxygen atom). Then R_2 would reflect formation and dissolution of the chemisorbed oxygen species. For example the “chemisorption” of oxygen might be regarded as the formation or stoichiometry change of an additional interfacial oxide phase of Pt or impurities with a significant stoichiometry range. The existence of impurity oxides at the Pt|YSZ interface is also

discussed in Ref. [95]. The data available so far do not allow a final conclusion whether one of these two or any other mechanism leads to the parallel path (R_2+C_2) and thus to the small shoulder in the impedance plots.

4.2 Measurements on low temperature deposited electrodes

4.2.1 Results of Impedance Measurements

The electrochemical experiments on low temperature deposited electrodes were conducted in the pseudo 4-wire setup explained in Sec. 2.2.2. The impedance between the Pt microelectrode and the Pt paste counter electrode was measured at set temperatures between 300 and 750 °C in a frequency range of 1 MHz – 10 mHz with a resolution of 10 points per decade. For a given set temperature microelectrodes of two different sizes (200 μm and 50 μm) were electrochemically characterized (3 to 5 of each size) and on each microelectrode 2 to 3 impedance spectra were recorded. After sweeping through the temperature range (starting with the highest set temperature of 750 °C and ending at 300 °C) again a measurement at 750 °C (set temperature) was carried out. Since the results were within the experimental error of the very first measurements, the samples were assumed to be sufficiently electrochemically stable. Significant effects of irreversible changes of the samples during the impedance measurements were therefore excluded.

The measured impedance spectra depicted in Figs. 26a-c consist of a large low frequency arc in the complex impedance plane, a small shoulder at medium frequencies, and a high frequency intercept (at high measurement temperatures) or onset of a high frequency arc (at lower measurement temperatures). In accordance with Sec. 4.1.2 and many other studies on microelectrodes [24, 31, 56, 62, 75] the large arc can be assigned to the electrochemical oxygen exchange reaction at the microelectrode. Any influences of the porous counter electrode on the measured impedance spectra can be excluded since its polarization resistance is negligible compared to that of the microelectrode (due to its orders of magnitude larger size). At the highest temperatures the large arc is mostly visible within the frequency range under investigation (Fig. 26a).

For lower temperatures, however, only a fraction of it was detected (Fig. 26c). Details on the analysis of the raw data and mechanistic interpretation will be given in the following.

4.2.2 Kramers Kronig test

The impedance spectra were tested in terms of the Kramers Kronig (KK) relation to further exclude time dependent influences on the impedance data. For Kramers Kronig testing, the program “K-K test version 1.01” by B.A. Boukamp was used [110, 111]. For an easy monitoring of KK-compliance the relative differences – $\Delta_{re,i}$ and $\Delta_{im,i}$ – between the data and its KK-compliant fit were calculated. The residuals are defined by [110]

$$\Delta_{re,i} = \frac{Z_{re,i} - Z_{re,KK}}{|Z_{KK}|} \quad \text{and} \quad \Delta_{im,i} = \frac{Z_{im,i} - Z_{im,KK}}{|Z_{KK}|} \quad (20)$$

where $Z_{re,i}$ and $Z_{im,i}$ denote the real and imaginary part of the measured impedance data and $Z_{re,KK}$ and $Z_{im,KK}$ denote the real and imaginary part of the KK-transform, respectively. $|Z_{KK}|$ is the magnitude of the KK-transform.

In Fig. 26 three representative impedance spectra (open circles) measured on 200 μm electrodes and the corresponding KK-transforms (closed green diamonds) as well as their residuals are shown. Absolute impedance data and the corresponding KK-transform are given in Figs. 26a-c, while the respective residuals are plotted as a function of frequency in Figs. 26d-f. KK-compliant impedance data (that means good match between data and KK-model) should only yield a scattering of the residuals around the $\log(f)$ axis [111]. In Fig. 26d (corresponding to 615 $^{\circ}\text{C}$) indication for some trace was found. A possible explanation is a fluctuation in the thermovoltage which could also be observed when measuring this thermovoltage by a voltmeter (Keithley 2000, USA). However, the magnitude of data corruption is below 0.5 % which is much lower than the scatter of the experimental data when comparing measurements on different electrodes. At medium temperatures (510 $^{\circ}\text{C}$, Fig. 26e) the traces become less pronounced but the scattering especially in the low frequency range was increased,

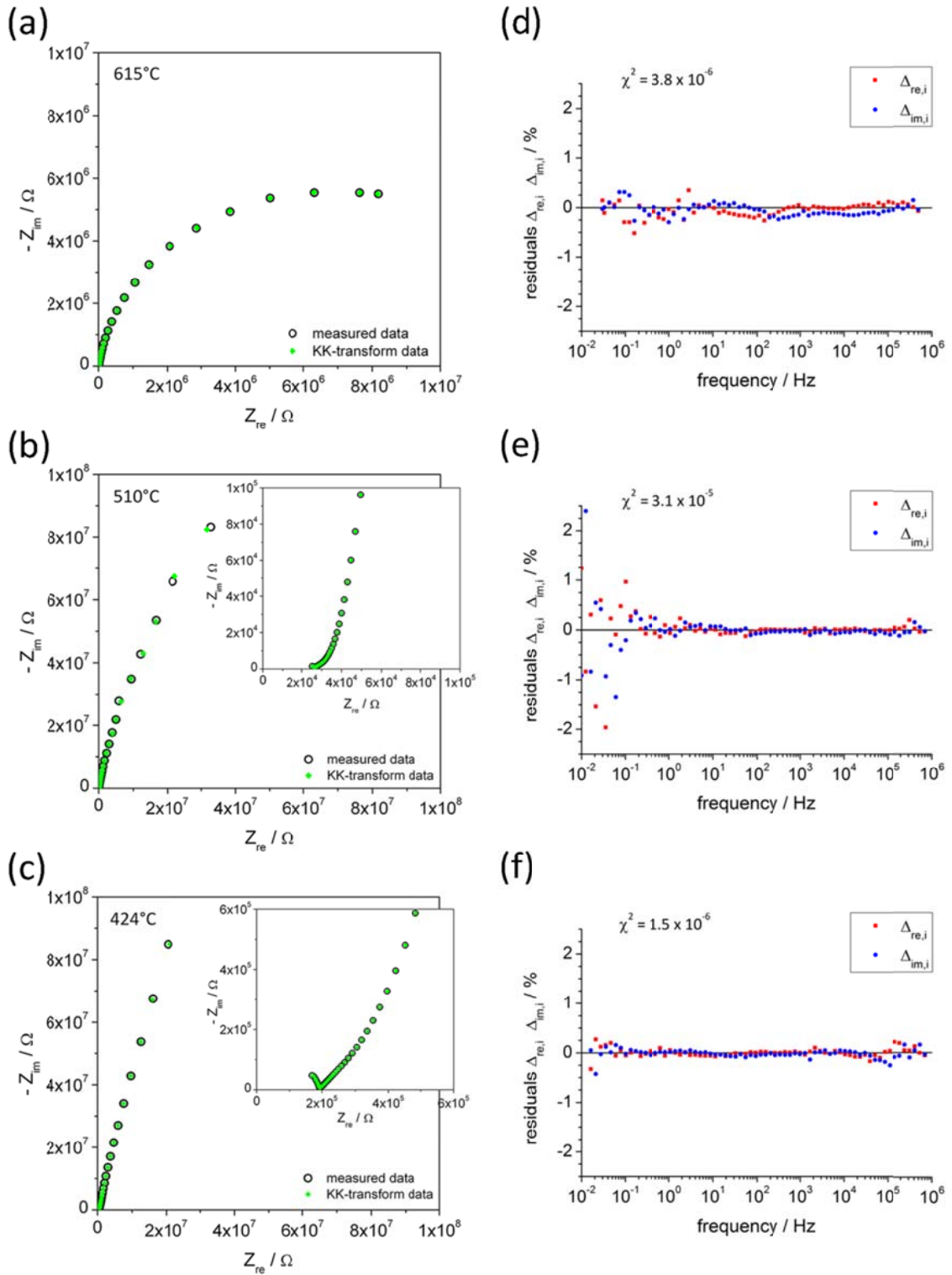


Figure 26: Comparison of three representative impedance spectra measured on 200 μm electrodes at three different temperatures (corrected values) with the results of the Kramers Kronig tests: (a) 615 °C, (b) 510 °C, (c) 424 °C. On the right hand side of each impedance spectrum the respective residual plot is shown (cf. Eq. 20): (d) 615 °C, (e) 510 °C, (f) 424 °C.

indicating more noisy data in this frequency range. In case of the low temperature (424 °C), the residuals plot in Fig. 26f indicates KK-compliant behavior as well as quite low noise. In summary, only minor (if any) systematic errors in the data were found in KK analysis. Hence, artifacts such as variations in activation energy due to changes of the samples during measurements (for example caused by irreversible changes of the electrodes due to a thermovoltage-induced polarization) could be excluded.

4.2.3 Parameterization

In Sec. 4.1 an equivalent circuit exhibiting a capacitively blocked path in parallel to a R-CPE element was applied to fit the impedance data (cf. Fig. 19). However, those Pt electrodes were differently prepared (high temperature deposition, 48 h annealing) and measurements were only performed at set temperatures above 700 °C. In case of low temperature deposited microelectrodes this circuit turned out to be applicable only to spectra obtained at the highest temperatures (above ~650 °C). For spectra recorded at lower temperatures the circuit in Fig. 19 did not lead to satisfying fit curves. Accordingly, a different circuit – shown in Fig. 27 – with two serial resistors was used instead for parameterization. One of the two resistors (R_{rds}) was always orders of magnitude larger than the other. Hence, the resistance R_{rds} was almost identical to the total polarization resistance of the microelectrodes and represents the rate determining step of the electrode reaction ($R_{\text{rds}} + R_{\text{B}} \approx R_{\text{rds}}$). To account for non-ideal capacitive behavior, constant phase elements (CPE_A and CPE_B) instead of ideal capacitances were used. The complex impedance of a constant phase element Z_{CPE} is given by Eq. 10. The rather

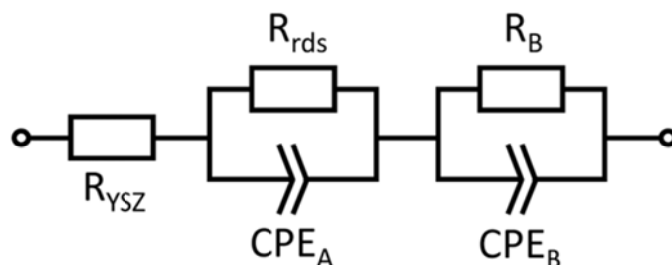


Figure 27: Equivalent circuit used for parameterization of impedance spectra measured at intermediate and low temperatures. R_{rds} represents the resistance of the rate determining step. The elements R_{B} and CPE_B were used to obtain satisfying fit results only.

small resistor R_B as well as the constant phase element CPE_B were only included to obtain sufficient fit quality but will here not be interpreted in a physical manner. The spreading resistance [74, 101] of ion conduction in YSZ (R_{YSZ}) and the known conductivity of YSZ were used to calculate the effective temperature of each individual electrode. The corresponding procedure was described in detail in Sec. 4.1.1 (Eq. 9). However, at lower temperatures (below 550 °C) values of 1.136 ± 0.002 eV and 21092 ± 1823 $\Omega^{-1}\text{cm}^{-1}$ were used for E_a and σ_0 , respectively. The corresponding Arrhenius plot of the YSZ conductivity measured by means of two extended electrodes in a standard sample holder is shown in Fig. 20.

In Fig. 28 measured impedance data are compared to the results of the CNLS fit using the equivalent circuit in Fig. 27. Since at lower temperatures only the onset of a huge electrode arc was visible in the low frequency range – see Figs. 28d and 26c – it has to be proven that such a fragmentary semicircle can yield reliable fit results. Therefore the high temperature spectrum in Fig. 28a was fitted in a reduced frequency range (omitting the lowest frequency points) – in Figs. 28b and c the frequency points used for this reduced range fit are indicated by the filled red circles. An extrapolation of the corresponding results is given in Fig. 28b by the blue dotted line and showed only about 10 – 15 % deviation in the resistance compared to the fit using the full (measured) frequency range (compare the extrapolations in Figs. 28a and b). This is still within the statistical scatter of measurements on different electrodes. An explanation for the rather low deviation is the “well-behaved” nature of the capacitor in parallel to R_{rds} . It can be quantified pretty well by a constant phase element with n -values of 0.88 ± 0.03 which stays almost constant over the entire temperature range. Accordingly, the depression of the corresponding arc in the complex impedance plane is almost the same for all examined temperatures and a small fraction of the arc is sufficient to get the whole information contained in the relaxation (i.e. the parameters R_{rds} , Q_A , and n_A). The capacitance of the arc can be calculated from the constant phase element CPE_A and the resistance R_{rds} by Eq. 10. An Arrhenius plot of the resulting capacitance is shown in Fig. 29. Even though capacitance C_A shows about 50 % relative standard deviation, it did not strongly change with decreasing temperature despite the fact that smaller and smaller parts of the arc were used in the fit. Hence, CNLS-fits of spectra measured at lower temperatures (fragmentary semicircles) can still be regarded as being quite

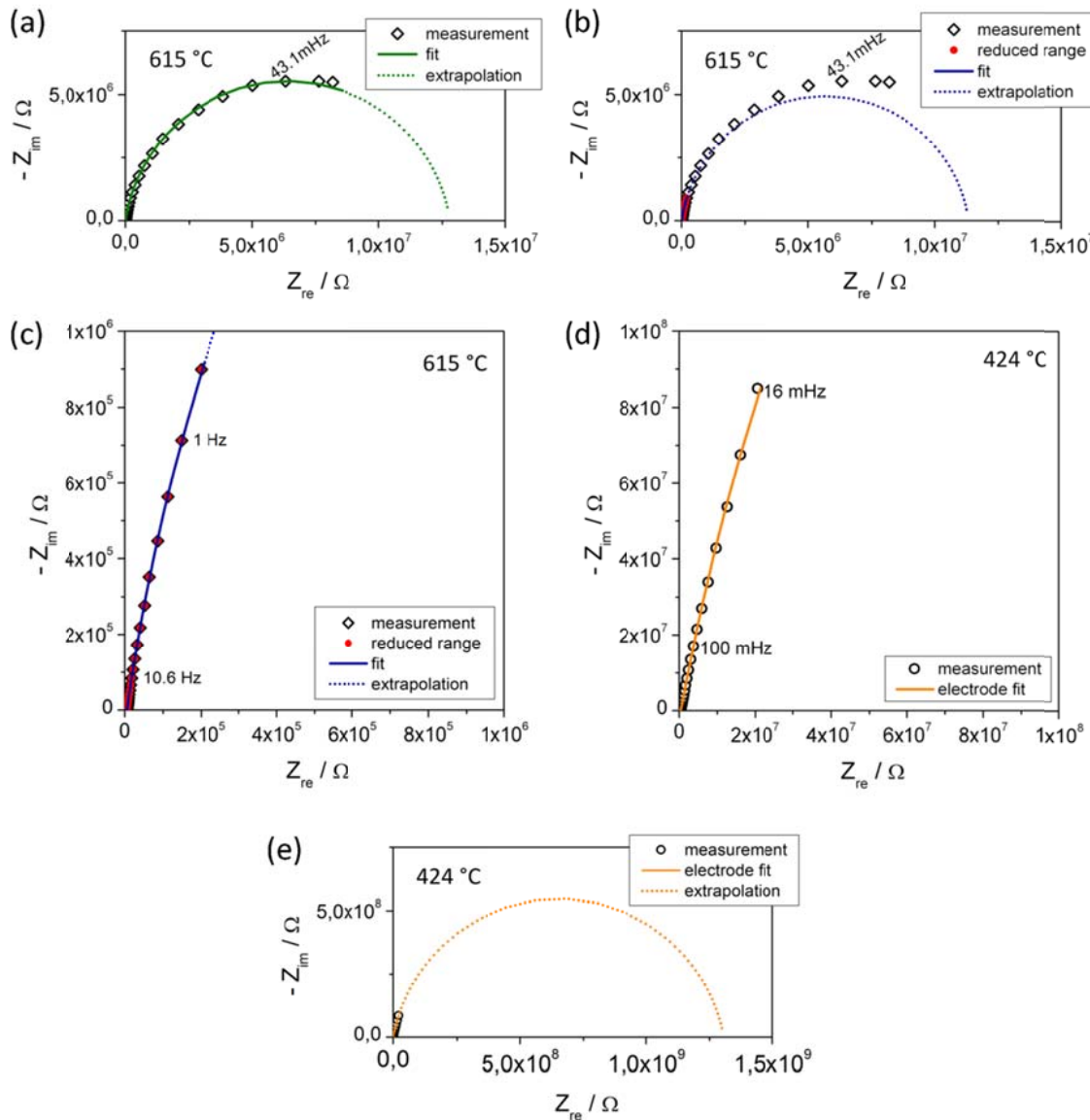


Figure 28: Impedance spectra measured at different temperatures on 200 μm electrodes compared with the results of the CNLS fit using the equivalent circuit in Fig. 27. (a) Measured impedance data at 615 °C electrode temperature (open diamonds) compared to the fit result (solid green line). The fit was extrapolated to very low frequencies (dotted green line) to indicate the dc resistance at this temperature. (b) Comparison of the measured data (open diamonds) with the extrapolated fit result (dotted blue line) when using only a reduced frequency range of the spectrum in the CNLS-fit (red filled circles). (c) Magnification of the medium frequency part of the spectrum in (b) indicating the reduced fit range. (d) Low frequency part of the spectrum measured at 424 °C (open circles) as well as the fit result (solid orange line). The extrapolation of the fit is shown in (e) with the orange dotted line.

reliable. In Fig. 28d a representative spectrum and its fit curve are shown for a lower measurement temperature; Fig. 28e shows the corresponding extrapolation.

The capacitor C_A exhibited an average value of about $600 \mu\text{F}/\text{cm}^2$ which is too high to be interpreted in terms of a double layer capacitor. This is also much higher than the value obtained for high temperature deposited electrodes (Sec. 4.1.2.2). Contributions by a chemical capacitance might explain such high values which could originate from oxygen in Pt grain boundaries or PtO_x /impurities at the Pt|YSZ interface [55, 95]. A detailed mechanistic interpretation on the origin of the high capacitance, however, cannot be drawn from the present data.

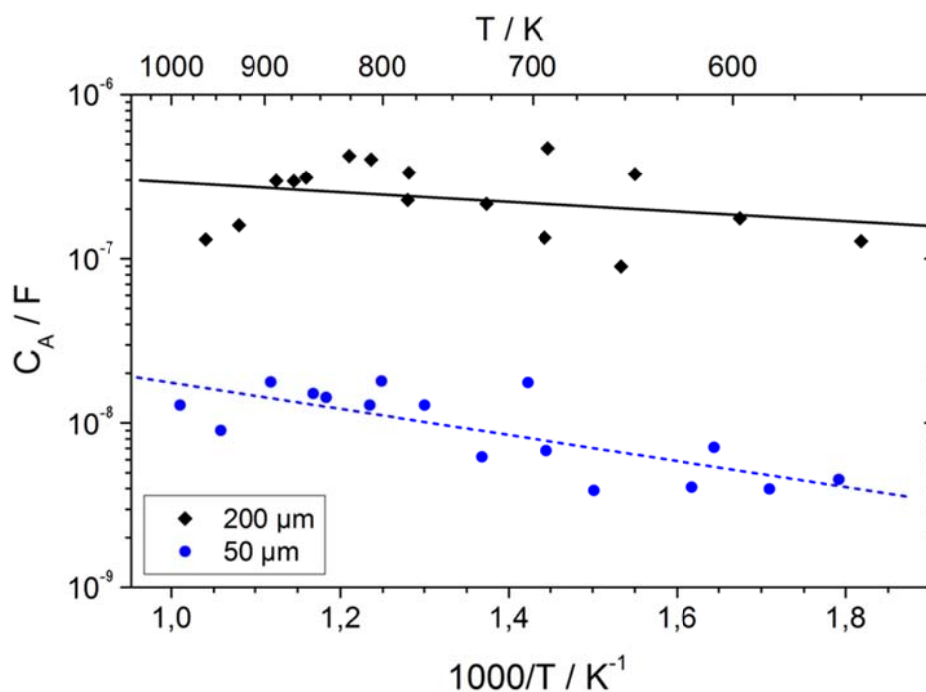


Figure 29: Capacitance C_A calculated by Eq. 10 from the constant phase element CPE_A , which in the equivalent circuit is in parallel to the resistance representing the rate determining step. Values were determined from the impedance data of $200 \mu\text{m}$ (black diamonds) and $50 \mu\text{m}$ electrodes (blue circles).

4.2.4 The geometry dependence of the electrode polarization resistance

The inverse values of R_{rds} are plotted in an Arrhenius diagram (see Fig. 30a). The data points already suggest two temperature regimes with different slopes in the Arrhenius plot and thus two processes with different activation energies. Since the slope (i.e. the activation energy) in the higher temperature range was obviously higher than for lower temperatures a parallel connection of two processes is an appropriate description of such a situation. This can be understood from the model calculations in Fig. 31 where the temperature dependent inverse resistances of two different electrode processes are sketched. Since they exhibit very different activation energies, their parallel or serial combination are both characterized by a changing slope in the Arrhenius diagram. However, only the parallel connection (red dotted curve) can lead to a situation with higher activation energy at higher temperature [53]. A serial connection (blue dotted curve) is unavoidably reflected by a lower activation energy at higher temperature and thus contradicts the results in Fig. 30a. Consequently, the Arrhenius diagram does not only give information on the activation energies of the processes (the slopes of the two parts of the resulting curve), but also on the type of connection of the involved resistive processes: parallel connections result in a concave shape and serial connections lead to a convex shape. The results were therefore analyzed in terms of two parallel oxygen exchange reaction paths with different activation energy.

To avoid an arbitrary definition of the transition range between the two activation energies the entire data set instead of two parts of the curve was fitted. For a parallel connection of two Arrhenius activated processes the fit equation for $1/R_{rds} = Y_{rds}$ reads

$$Y_{rds} = Y_1^0 \cdot e^{-\frac{E_{a1}}{k_b T}} + Y_2^0 \cdot e^{-\frac{E_{a2}}{k_b T}} \quad (21)$$

Therein the pre-exponential factors Y_1^0 and Y_2^0 as well as the activation energies E_{a1} and E_{a2} were fitting parameters. For an appropriate fit a weighting function w (different from one as in case of a linear fit equation) had to be defined and

$$w = \left(\frac{1}{\text{fit } Y} \right)^2 \quad (22)$$

was used which leads to a minimization of the relative deviation of the measured values from the fit results according to:

$$\left({}^{meas}Y - {}^{fit}Y \right)^2 \cdot w = \left(\frac{{}^{meas}Y - {}^{fit}Y}{{}^{fit}Y} \right)^2 = Min! \quad (23)$$

The fit results for 200 μm and 50 μm electrodes are given in Fig. 30a by the solid black line and the dashed blue line, respectively. The resulting activation energies (c.f. Eq. 21) are summarized in Tab. 5; on average 1.6 eV and 0.2 eV are found for the high and low temperature regime, respectively.

For the investigation of the geometry dependence of $1/R_{rds}$ both fit curves were related to the length of the TPB (calculated from the electrode diameter d_{ME} by $\pi \cdot d_{ME}$) as well as to the area of the electrodes ($\pi \cdot d_{ME}^2/4$). In Fig. 30b the fit curves related to the TPB length are shown. In this diagram the branches with the higher activation energy (at higher temperatures) fall together indicating a rate determining process at or close to the TPB in this temperature regime. In the plot of the area-related fit results – Fig. 30c – the shallow branches (at lower temperatures) coincide. In this temperature range the rate determining step is obviously related to the area of the electrodes. This different geometry dependence of the two parts of the fit curves clearly indicates a change of the geometry dependence of the polarization resistance and thus of the rate determining step. Moreover, the shape of the curve (higher E_a at higher temperatures and lower E_a at lower temperatures) indicates a parallel connection of these two processes (cf. Fig. 31). Altogether, the observed behavior suggests two different reaction pathways connected in parallel.

For the sake of completeness another interpretation of the temperature dependence should also be excluded: It was frequently discussed in literature that a co-limitation of two processes rather than only one single elementary step could be responsible for the polarization resistance of Pt electrodes on YSZ [4, 47, 52, 53]. Situations potentially leading to co-limited kinetics typically include a diffusion process (e.g. surface diffusion of adsorbed oxygen) and a reaction perpendicular to the diffusion direction (e.g. adsorption/desorption on the surface). Such a situation is sketched in Fig. 32a – the corresponding equivalent circuit (transmission line; capacitances neglected) is shown in Fig. 32b. However, also such a situation cannot explain the observed

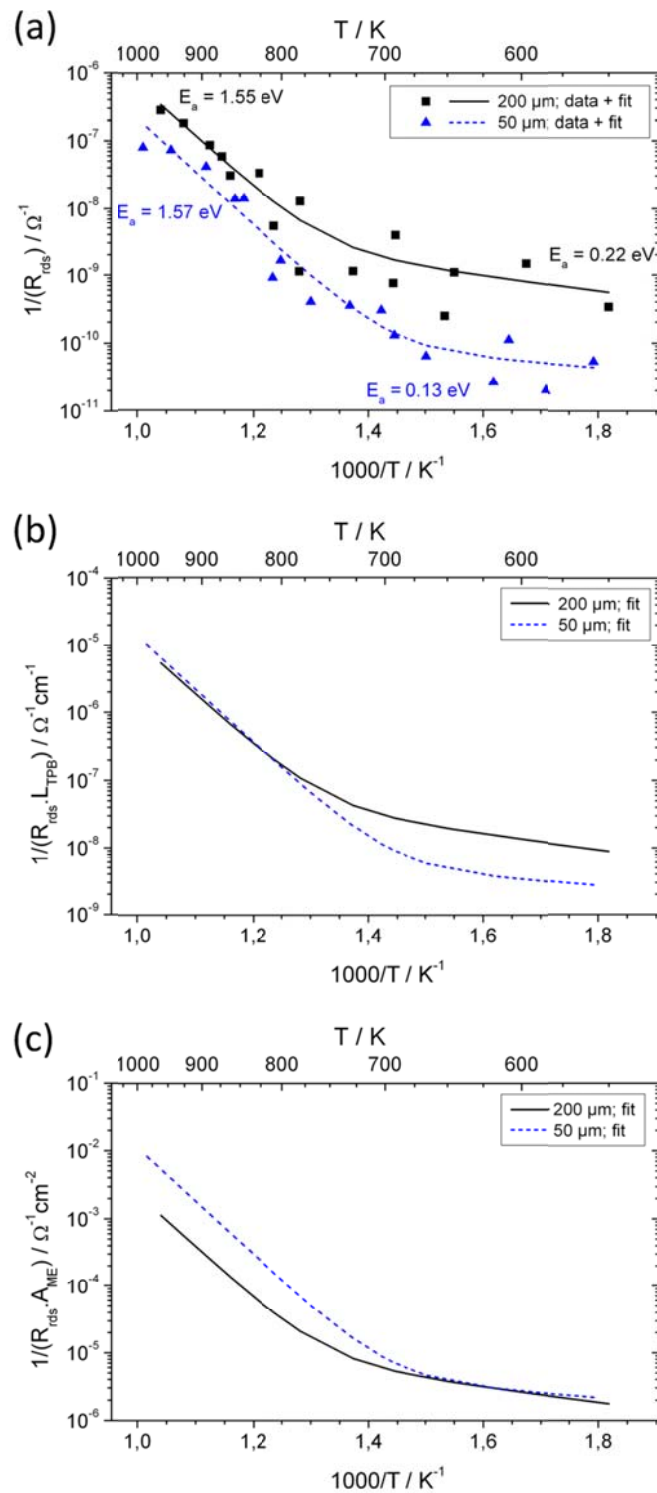


Figure 30: Arrhenius plot of the inverse polarization resistance representing the rate determining step. (a) Raw data of 200 μm (black squares) and 50 μm electrodes (blue triangles). Further the resulting fit curves using Eq. 21 are shown – 200 μm : solid black line; 50 μm : dashed blue line. (b) Fit results of 200 μm and 50 μm data related to the TPB length of the electrodes. Obviously at higher temperatures the steeper branches of the curves fall together. (c) Plot of area-related fit results; in this case the shallow branches fall together.

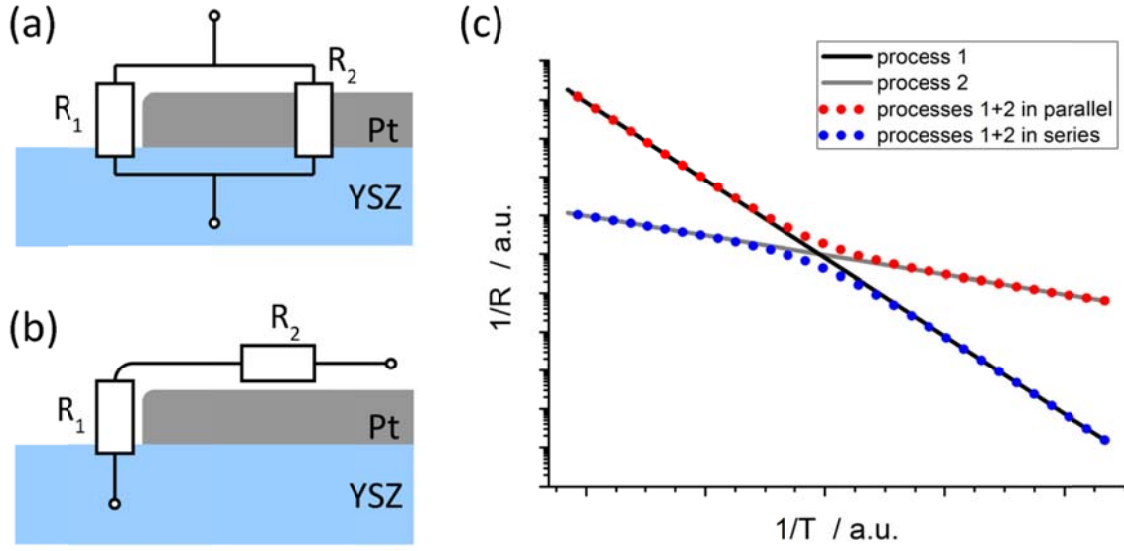


Figure 31: (a) Equivalent circuit describing two parallel resistive electrochemical processes (capacitive processes not shown). Resistor 1 represents the surface path with a rate determining step located close to the TPB. Resistor 2 symbolizes an area-related rate determining process of the pathway through the Pt electrode. (b) Equivalent circuit with two slow serial electrochemical processes (capacitances again neglected). (c) Expected Arrhenius diagram for the situations in (a) and (b) assuming different activation energies for the two processes.

Table 5: Activation energies of the processes responsible for the rate determining step of the electrode reaction obtained by fitting the measured data in Fig. 30a using Eq. 21.

electrode size [μm]	E_{a1} [eV]	E_{a2} [eV]
200	1.55	0.22
50	1.57	0.13
average	1.6	0.2

temperature dependence: For the hypothetical situation of a stripe shaped electrode with only one TPB being electrochemically active the polarization resistance of co-limited kinetics is given by [18]

$$R_{co} = \sqrt{\frac{1}{\sigma_{lat} X_{perp}}} \cdot \coth \left(H \sqrt{\frac{X_{perp}}{\sigma_{lat}}} \right). \quad (24)$$

Therein R_{co} denotes the resulting polarization resistance of co-limitation, σ_{lat} the lateral “conductivity” (e.g. of surface diffusion), χ_{perp} a constant quantifying the kinetics of the process perpendicular to the diffusion process (e.g. adsorption/desorption) and H the width of the electrode stripe. In Fig. 32c the resulting Arrhenius plot is sketched with the lateral diffusion exhibiting higher activation energy than the perpendicular reaction ($E_{a,lat} > E_{a,perp}$); Fig. 32d shows the opposite situation ($E_{a,lat} < E_{a,perp}$). In both cases Arrhenius curves with higher activation energy at lower temperature are found.

Even though Eq. 24 is exactly valid only in case of stripe shaped electrodes (with only one electrochemically active TPB) and should be modified for circular electrodes, it still allows a qualitative estimation of the temperature dependence of co-limited reaction kinetics on thin film electrodes. It can thus be concluded that co-limited reaction kinetics in the entire investigated temperature range cannot explain the result of a lower activation energy at lower temperatures. Indeed two parallel pathways have to be assumed. Co-limitation being responsible for only one branch of the measured Arrhenius curve, however, would still be in accordance with the measured results.

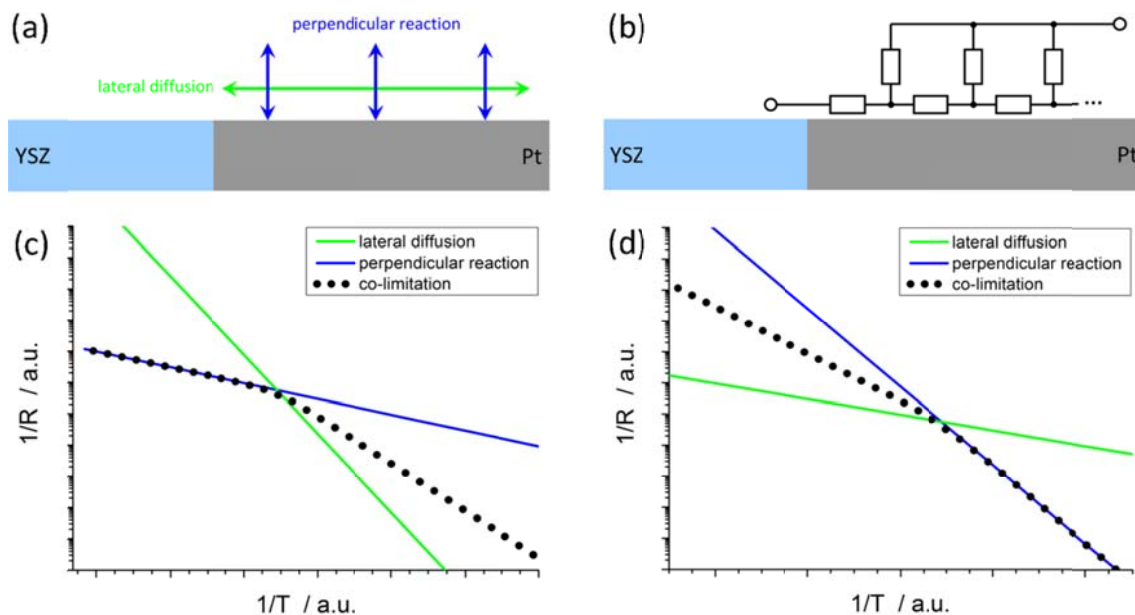


Figure 32: (a) Schematic illustration of two electrode processes potentially leading to a co-limited polarization resistance. (b) Equivalent circuit corresponding to the situation in (a) – capacitances were neglected. (c) Arrhenius diagram of the conductances of the two individual processes and the resulting co-limitation with the lateral diffusion process having a higher activation energy than the perpendicular reaction ($E_{a,lat} > E_{a,perp}$). (d) Resulting Arrhenius diagram with $E_{a,lat} < E_{a,perp}$.

4.2.5 Mechanistic discussion of oxygen exchange

It remains to be discussed which detailed reaction paths and rate determining steps are in accordance with the experimental results. It thus has to be searched for kinetic situations where two parallel paths are possible for oxygen exchange, one path having a rate determining step located close to the TPB while the other one exhibits an area-related rate determining step. The activation energies of the rate limiting elementary steps are 1.6 eV and 0.2 eV for the TPB- and area-related paths, respectively. In order to limit the possible kinetic scenarios, the following assumptions are made before discussing possible rate limiting processes.

i) Fast surface diffusion of oxygen adsorbed on platinum: In Ref. [66] in-situ imaging of the spill-over process of oxygen on single crystalline Pt (111) electrodes (on YSZ) was successfully demonstrated by scanning photoelectron microscopy. There, the authors showed that an anodic oxygen release ($U_{\text{set}} = +0.2 \text{ V}$; $400 \text{ }^\circ\text{C}$) led to a front of adsorbed oxygen moving from the TPB along the entire Pt surface. From these measurements a surface diffusion coefficient of $9.2 \pm 1.8 \cdot 10^{-4} \text{ cm}^2\text{s}^{-1}$ was obtained. Moreover, it could be concluded that the surface diffusion process was much faster than the desorption process, otherwise motion of the surface diffusion front over several hundred micrometres would not have been observed. On the length scale of the microelectrodes surface diffusion is thus assumed to be not included in the rate determining step.

ii) Close to equilibrium conditions oxygen reduction and incorporation into YSZ was assumed to only take place underneath the Pt electrode. This is concluded from the ToF-SIMS results presented in Sec. 5 where it will be shown, that only at very high electrode polarization (-2.18V) oxygen tends to be incorporated also along the free YSZ surface. Hence, also ionization by electrons from YSZ is not considered.

Regarding these assumptions three pathways of oxygen exchange are taken into account in the following discussion: a bulk path through the electrode (I), a surface path along the Pt electrode (II) and an alternative surface path along the free YSZ surface (III). In Fig. 33a a sketch of this situation is shown. In the following sections it is discussed which combinations of these paths and which rate determining steps are compatible with the experimental observations.

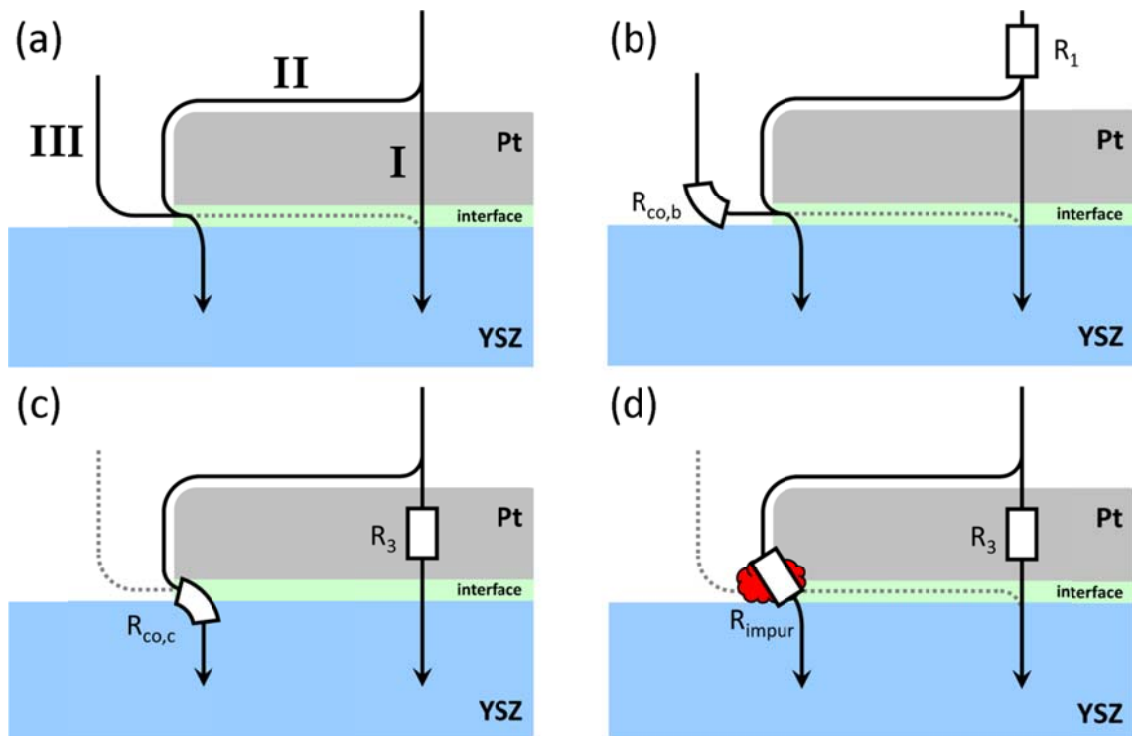


Figure 33: (a) Possible reaction pathways assuming fast Pt surface diffusion and negligible oxygen reduction/incorporation on free YSZ. The gray dotted path along the Pt|YSZ interface would only be accessible in case of fast interface diffusion. (b) Reaction pathways in (a) with oxygen adsorption on Pt being the area-related rate limiting step and co-limitation of adsorption and surface diffusion on YSZ (with a short decay length) being the slowest TPB-related elementary step. (c) Situation with oxygen diffusion through Pt (along grain boundaries) being the area-related rate determining step in parallel to co-limitation of oxygen diffusion along the interface and charge transfer at the interface with a short decay length being the TPB-related rate limiting step. (d) Alternative to the situation in (c) with diffusion of an adsorbed oxygen species through an impurity phase as the TPB-related rate limiting process.

4.2.5.1 Slow oxygen adsorption on Pt in parallel to co-limitation of oxygen adsorption and surface diffusion on free YSZ

One possible scenario is slow oxygen adsorption on the entire Pt surface as area-related process, followed by fast transport through Pt (I) or along the Pt surface (II) and fast incorporation of this oxygen along the Pt|YSZ interface or close to the TPB. Slow TPB-related processes can only be in parallel to such an assumed adsorption step if they are associated with the free YSZ surface (path III in Fig. 33a). For example a co-limitation of oxygen adsorption on YSZ and a surface diffusion of the adsorbed species with a short decay length would represent such a situation (Fig. 33b).

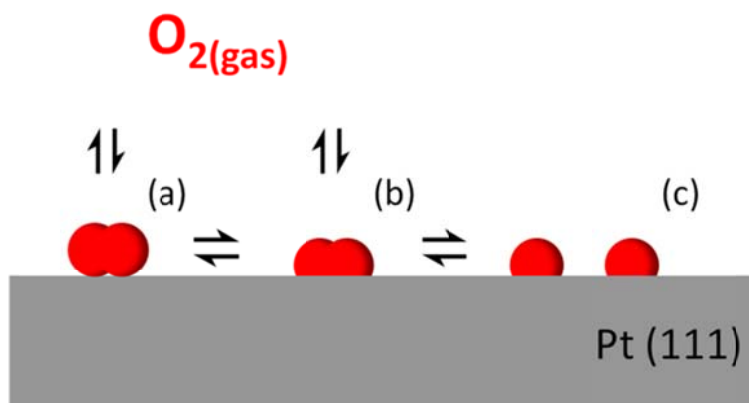


Figure 34: Sketch of the possible reaction steps of oxygen adsorption on Pt (111) – cf. Ref. [112]: (a) Physisorbed molecular species. (b) Chemisorbed molecular species (e.g. superoxo or peroxy species). (c) Dissociatively chemisorbed oxygen.

At temperatures > 150 K oxygen adsorbs dissociatively on platinum (111) surfaces forming $p(2 \times 2)$ layers with the resulting atomic species covalently bonded in the threefold hollow site [113, 114]. The mechanism of oxygen adsorption on Pt (111) is believed to proceed via molecular physisorbed or chemisorbed (superoxo or peroxy) precursor species [112, 113, 115] (cf. Fig. 34). Neglecting any effects of the physically adsorbed molecular species (cf. Fig. 34a) the adsorption reaction via a molecularly chemisorbed intrinsic precursor can be described by [112-115]



with a very fast first molecular adsorption step; r_a denotes the rate of dissociation, and r_{-a} the rate of reaction from the atomically adsorbed state into the molecularly adsorbed state. For such an adsorption process a sticking coefficient S can be defined

$$S = \frac{r_a}{2 \cdot P_{\text{tot}}} \quad (26)$$

where P_{tot} denotes the total impinging rate of O_2 per unit area. Further, under equilibrium conditions

$$r_{\text{eff}} = r_{a,\text{eq}} - r_{-a,\text{eq}} = r_{a,\text{eq}} - k_{-a} \cdot \Theta_{\text{eq}} = 0 \quad (27)$$

holds, where r_{eff} denotes the effective (net) reaction rate of the rate limiting dissociation step, k_{-a} the rate constant of reaction from the atomically adsorbed state into the molecularly adsorbed state, and Θ_{eq} the equilibrium coverage of atomically adsorbed oxygen. If the equilibrium is disturbed (e.g. by the ac signal of an electrochemical impedance experiment) the coverage of the atomically adsorbed species is changed by $\Delta\Theta$ and therefore the effective reaction rate changes to

$$r_{\text{eff}} = r_{a,\text{eq}} - k_{-a} \cdot \Theta = r_{a,\text{eq}} - k_{-a} \cdot (\Theta_{\text{eq}} + \Delta\Theta) = r_{a,\text{eq}} - r_{-a,\text{eq}} - k_{-a} \cdot \Delta\Theta \quad (28a)$$

$$r_{\text{eff}} = -k_{-a} \cdot \Delta\Theta \quad (28b)$$

Since atomically adsorbed oxygen is the electrochemically active species [19, 65, 66], the trapping of oxygen from the gas phase into the precursor state is virtually not affected. Consequently, also the rate of dissociative adsorption $r_{a,\text{eq}}$ is not affected by electrochemical manipulation. The resulting current I_{eff} is given by

$$I_{\text{eff}} = ze_0 \cdot r_{\text{eff}} = -ze_0 \cdot k_{-a} \cdot \Delta\Theta \quad (29)$$

where z is the number of transferred electrons. The change in coverage is coupled to the electrode overpotential η by Nernst's equation

$$\eta = \frac{k_B T}{ze_0} \cdot \ln\left(\frac{\Theta}{\Theta_{\text{eq}}}\right) = \frac{k_B T}{ze_0} \cdot \ln\left(\frac{\Theta_{\text{eq}} + \Delta\Theta}{\Theta_{\text{eq}}}\right) = \frac{k_B T}{ze_0} \cdot \ln\left(1 + \frac{\Delta\Theta}{\Theta_{\text{eq}}}\right) \quad (30)$$

The change of the coverage thus depends on the voltage via

$$\Delta\Theta = \Theta_{\text{eq}} \left(e^{\frac{ze_0 \eta}{k_B T}} - 1 \right) \quad (31)$$

and the current – given in Eq. 29 – reads

$$I_{eff} = -ze_0 \cdot k_{-a} \cdot \Theta_{eq} \left(e^{\frac{ze_0\eta}{k_B T}} - 1 \right). \quad (32)$$

The inverse polarization resistance of adsorption kinetics at equilibrium conditions $1/R_{ac,eq}$ is given by the slope of the current-voltage-curve at $\eta = 0$ V

$$\frac{1}{R_{ad,eq}} = \left. \frac{dI_{eff}}{d\eta} \right|_{\eta=0} = ze_0 \cdot k_{-a} \cdot \Theta_{eq} \cdot \frac{ze_0}{k_B T}. \quad (33)$$

After inserting Eqs. 26 and 27 as well as $z = 2$ for $O_{(ad)}$ in Eq. 33

$$R_{ad,eq} = \frac{k_B T}{4e_0^2} \cdot \frac{1}{r_a} = \frac{k_B T}{8e_0^2} \cdot \frac{1}{S \cdot P_{tot}}. \quad (34)$$

results for the polarization resistance. The total impinging rate

$$P_{tot} = \frac{N}{2V} \sqrt{\frac{k_B T}{M}} \quad (35)$$

can be obtained by kinetic gas theory [116]; N denotes the number of oxygen molecules within the volume V and M the mass of an O_2 molecule. The sticking coefficient shows Arrhenius type behavior at temperatures above 200 K [113]. Depending on the kinetic energy of the impinging oxygen molecule activation energies E_s of the sticking coefficient between 0.04 and 0.13 eV were reported [112, 113, 115]. Consequently, the temperature dependence of the inverse polarisation resistance is dominated by the temperature dependence of the sticking coefficient. Since, the activation energy of the measured area-related exchange rate (0.2 eV) is quite similar to the values of E_s the area-related polarization resistance could be attributed to an adsorption/desorption process.

However, despite the promising accordance in activation energy, adsorption kinetics is not believed to be rate limiting due to the following estimation: The resulting polarization resistance of the adsorption process can be calculated by Eq. 34. For impact energies of oxygen molecules corresponding to 650 K gas temperature sticking

coefficients are reported to be between 0.05 and 0.2 [112, 113, 115]. At this temperature, P_{tot} for oxygen in ambient air (200 mbar partial pressure) can be calculated from Eq. 35 to be $1.1 \cdot 10^{27} \text{ m}^{-2}\text{s}^{-1}$. Assuming the worst case scenario with $S = 0.05$ Eq. 34 yields an electrochemical adsorption resistance of $7.9 \cdot 10^{-10} \Omega\text{m}^2$. For a $200 \mu\text{m}$ microelectrode a polarization resistance of $2.5 \cdot 10^{-2} \Omega$ is thus predicted for adsorption under equilibrium conditions. This is far below the values measured on $200 \mu\text{m}$ electrodes at 650 K in this study ($\sim 10^9 \Omega$) and hence it can be concluded that the area-related polarization resistance is not caused by adsorption limited kinetics.

4.2.5.2 Oxygen diffusion through Pt in parallel to a path with charge transfer close to the TPB

Another rate limiting step with a reaction rate proportional to the electrode area would be diffusion through the Pt thin film – most likely proceeding along Pt grain boundaries [33, 35]. Rate limiting gas diffusion through any pores in the Pt films is excluded even though it would indeed lead to a small temperature dependence: First, such pores are not found in the SEM studies and second, even if there were some residual pores this would simply slightly enhance the TPB length and should virtually not modify the temperature dependence. Moreover, gas diffusion through pores would be connected in series with the TPB process which also contradicts the experimental results. In Ref. [35] the activation energy of 0.68 eV for grain boundary diffusion of oxygen in Pt was calculated by ab-initio methods. The inverse polarization resistance $1/R_{\text{diff}}$ of a diffusion limited electrode reaction close to equilibrium (assuming one dimensional diffusion through the Pt thin film) reads

$$\frac{1}{R_{\text{diff}}} = \frac{(ze_0)^2}{k_B T} \cdot \frac{D \cdot c_{\text{O}(\text{gb})}}{h} \quad (36)$$

with h being the film thickness, D the diffusion coefficient and $c_{\text{O}(\text{gb})}$ the equilibrium concentration of the diffusing oxygen species in the Pt grain boundary next to the surface [1]. The temperature dependence of D is given by Arrhenius' equation

$$D = D' \cdot e^{-\frac{E_{\text{diff}}}{k_B T}} \quad (37)$$

with D' denoting the pre-exponential factor and E_{diff} the activation energy of the diffusion process. For rate limiting diffusion the gas phase and the oxygen in the grain boundary are assumed to be in thermodynamic equilibrium – i.e. the reaction



is fast. For low concentrations $c_{O(gb)}$ is given by mass action law:

$$K = \frac{c_{O(gb)}}{\sqrt{p_{O_2}}} = K' \cdot e^{\frac{\Delta_r g}{k_B T}} = K' \cdot e^{\frac{\Delta_r h - T \Delta_r s}{k_B T}} = K'' \cdot e^{\frac{\Delta_r h}{k_B T}} \quad (39a)$$

$$c_{O(gb)} = \sqrt{p_{O_2}} \cdot K'' \cdot e^{\frac{\Delta_r h}{k_B T}} \quad (39b)$$

In Eqs. 39a and b p_{O_2} denotes the partial pressure of oxygen in the gas phase, K is the equilibrium constant, K' the pre-exponential factor, and K'' the modified pre-exponential factor ($K'' = K' \cdot e^{\frac{\Delta_r s}{k_B}}$); $\Delta_r g$, $\Delta_r h$, and $\Delta_r s$ are Gibb's free reaction enthalpy, reaction enthalpy, and reaction entropy for the reaction in Eq. 38, respectively. The reaction enthalpy of this reaction can be estimated from the binding energy of the O_2 molecule which is 4.91 eV per O atom and the binding energy of the oxygen species in the Pt grain boundary which is in the range of 3.97 - 4.60 eV [35]. Consequently a value between -0.31 and -0.94 eV results for $\Delta_r h$. Inserting Eqs. 37 and 39b in 36 yields

$$\frac{1}{R_{diff}} = \frac{(ze_0)^2}{k_B T} \cdot \frac{D'}{h} \cdot e^{\frac{E_{diff}}{k_B T}} \cdot \sqrt{p_{O_2}} \cdot K'' \cdot e^{\frac{\Delta_r h}{k_B T}} \quad (40)$$

The effective activation energy E_a of the inverse polarization resistance can therefore be estimated by

$$E_a \approx E_{diff} + \Delta_r h \quad (41)$$

to be in the range of 0.37 and -0.26 eV. This value is in reasonable agreement with the activation energy (0.2 eV) of the area-related reaction rate obtained from electrochemi-

cal measurements. Hence, a diffusion of oxygen through the Pt thin film is a very reasonable explanation for the area-related process.

Because adsorption as well as surface diffusion were excluded as kinetically slowest steps of the TPB-related path, a charge transfer step at the TPB is a realistic rate determining step of path II. More precisely – since the electrochemical reaction is assumed to take place at the Pt|YSZ interface – co-limitation of oxygen diffusion along the Pt|YSZ interface and charge transfer at this interface with a short decay length of the corresponding transmission line would be a possible TPB-related rate determining step (an equivalent circuit is sketched in Fig. 33c). Such a short decay length, however, can only be expected in case of slow interface diffusion. For fast interface diffusion a large decay length would result and the polarisation resistance would not scale with the length of the TPB.

An alternative TPB-related rate limiting step in parallel to oxygen diffusion through Pt would be oxygen diffusion through an impurity phase at the TPB (cf. Fig. 33d). Such impurity phases (particularly SiO₂ containing) were frequently discussed in the past to deteriorate the exchange rates of TPB-active electrodes [50, 93, 95, 104, 117]. In ToF-SIMS measurements impurity elements such as Si and Ca could be

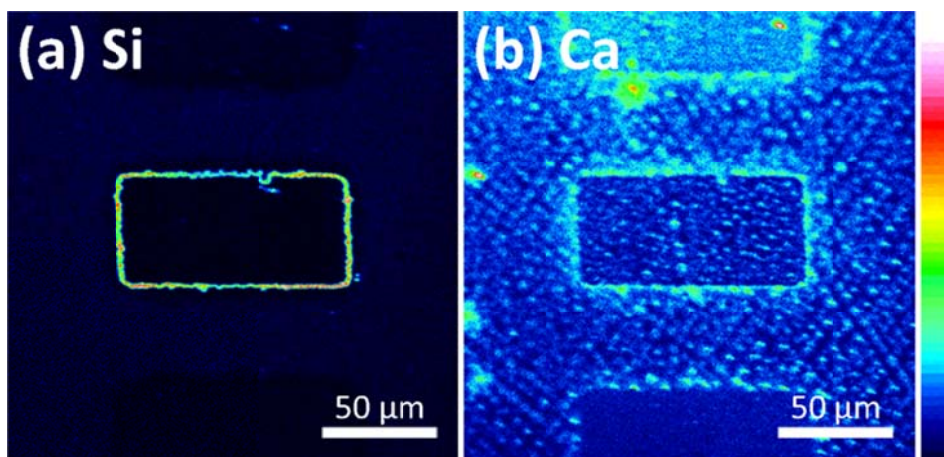


Figure 35: Distribution images (intensity plots) obtained by ToF-SIMS showing impurities on the YSZ surface after removing the Pt thin film electrode in nitrohydrochloric acid. The electrode in the center was strongly polarized (overpotential $\eta = -2.22$ V at 303 °C for 10 min), the neighboring electrodes – above and below – were not polarized during the experiment. (a) Accumulation of Si at the TPB of the polarized electrode. (b) Calcium distribution on YSZ.

identified at TPBs of strongly polarized Pt electrodes – cf. Fig. 35. However, it was not possible so far to unambiguously prove the existence of sufficient amounts of these impurities to affect electrode behavior also at equilibrium conditions. An effect of impurities on the TPB-process is also mentioned in Sec. 6 where the results of dc measurements are discussed.

4.2.5.3 Comparison with electrode “conductivities” in literature

A comparison of the TPB length related inverse polarization resistances (electrode “conductivities”) of the present study with values found in literature is shown in Fig. 36. Most activation energies and also several absolute values from other studies are in good agreement with the TPB length related data of the obtained results [40, 41, 51]. Moreover, it becomes obvious that the high temperature prepared electrodes (Sec. 4.1) exhibited a lower “conductivity” than the low temperature deposited ones. The deviations could possibly be attributed to impurities at the TPB: The high temperature deposition procedure of the Pt thin films as well as the longer annealing (cf. Secs. 2.1.1 and 2.1.2) might influence the amount of impurities accumulated at the TPB and therefore the polarization resistance of oxygen exchange [93, 104, 105]. The oxygen exchange mechanism at the TPB is thus assumed to be identical on both kinds of Pt electrodes (high and low temperature prepared).

Pt electrodes exhibiting higher “conductivity” values were found in Refs. [22, 42, 50]. In Ref. [50] silicon containing contaminations were demonstrated to tremendously affect the oxygen exchange kinetics of Pt electrodes. The Pt electrodes with the highest “conductivity” (▲ in Fig. 36) were shown to be free of these contaminations. In the study on porous Pt electrodes in Ref. [117], however, SiO₂ impurities only deteriorated the electrode performance when being located at the Pt|YSZ interface. Traces of SiO₂ on the surface of Pt even decreased the electrode polarization resistance. This effect was discussed in terms of a change in adsorption kinetics of oxygen on platinum. A change in oxygen surface concentration would also affect a polarisation resistance caused by an elementary step subsequent to adsorption (such as charge transfer or oxygen diffusion through an impurity phase at the TPB). Taking the strong effect of SiO₂ impurities into account the scenario in Fig. 33d seems to be the most realistic one.

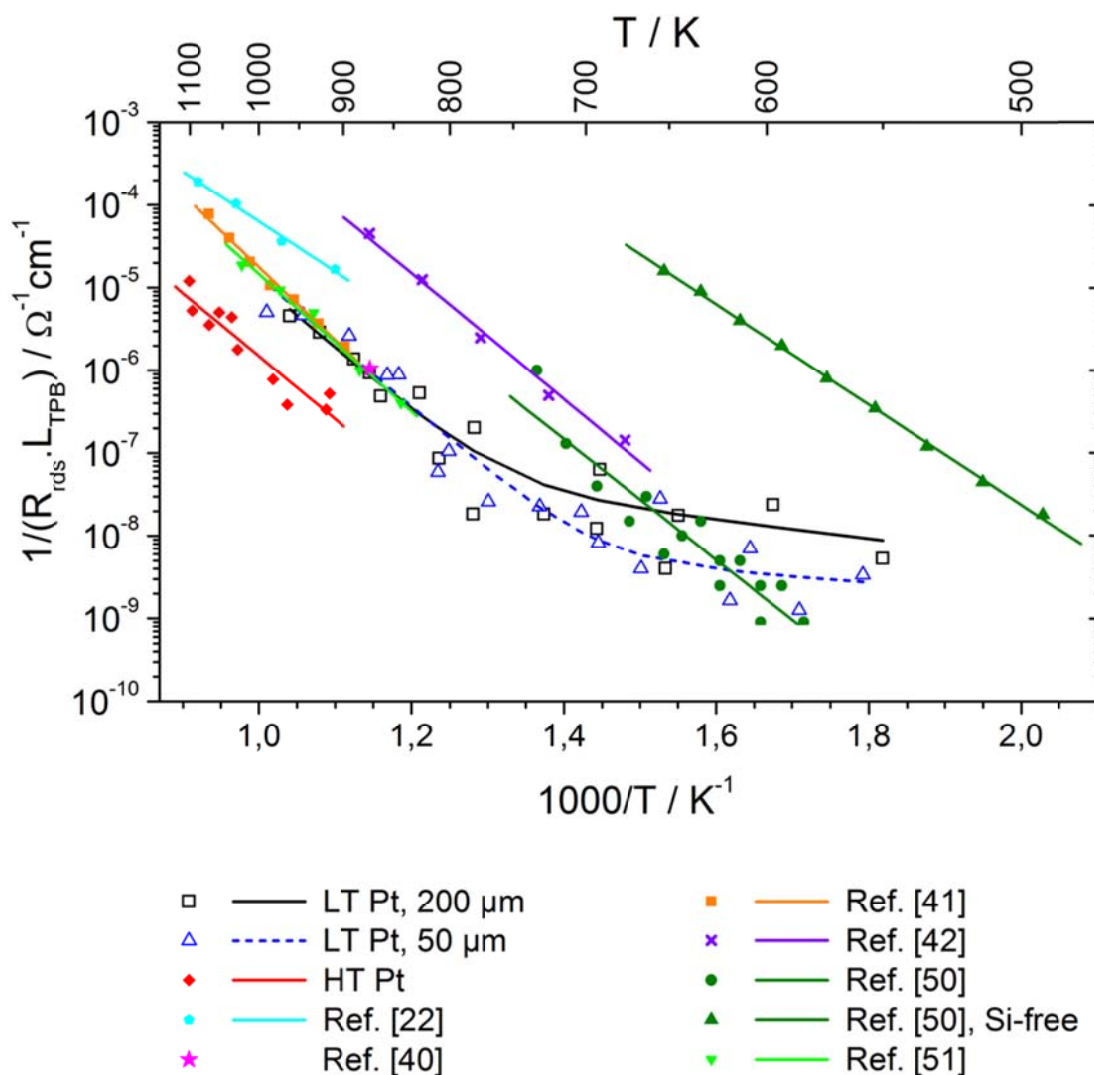


Figure 36: Comparison of the Arrhenius curves from the present thesis with electrode “conductivities” from literature. The terms LT Pt and HT Pt denote low temperature deposited and high temperature deposited Pt electrodes, respectively.

An area-related rate determining reaction step with a quite low activation energy of 0.2 eV as found in this study was not reported so far. This might be attributed to the extreme aspect ratio of the electrodes (50 – 200 μm diameter, 350 nm thickness) which – compared to Pt particles in porous paste electrodes – favours a bulk path. Moreover, the quite small grain sizes of the low temperature deposited electrodes (150 – 200 nm) and the consequently very high number of grain boundaries yielding a higher conductance of a diffusive path along Pt grain boundaries might be responsible for making this path electrochemically observable.

5 Results and Discussion of Tracer Incorporation Experiments

For further analyzing reaction paths and mechanisms of oxygen reduction on Pt|YSZ voltage-driven ^{18}O tracer incorporation experiments with subsequent ToF-SIMS analysis of the tracer distribution were performed. These results are presented in Sec. 5.2. These experiments were complemented by the electrochemical characterization of the corresponding rectangular shaped Pt microelectrodes. Results of these electrochemical measurements are given in Sec. 5.1.

5.1 Electrochemical experiments

5.1.1 Impedance results without dc bias

The impedance spectra measured at the rectangular, high temperature deposited Pt electrodes at zero bias and 350 °C set temperature show a high frequency semicircle originating from the YSZ bulk [31, 74] and the onset of a huge low frequency arc. In Figs. 37a and 37b an exemplary spectrum without dc bias is shown (open symbols). The fitting results – also shown in Fig. 37 in solid lines – were obtained using two serial R-CPE elements as an equivalent circuit. Since YSZ single crystals were used, grain boundaries can be ruled out as an origin of any impedance feature and the low frequency arc has again to be attributed to electrochemical electrode processes. This is in accordance with the low temperature measurements in Sec. 4.2 and further supported by the nonlinear current-voltage behavior of the low frequency semicircle (see Sec. 5.1.2). Owing to geometrical reasons again only a very small resistive contribution of this arc is caused by the extended porous counter electrode and the onset of the low frequency impedance arc is thus almost exclusively attributed to the Pt microelectrode [31]. Obviously its relaxation frequency is much too low to make spectra completely visible in the frequency range used (cf. Sec. 4.2). The high frequency arc on the other

hand can be attributed to the bulk resistance due to ion transport in YSZ and an unavoidable stray capacitance between the contact needles of the order of a few 10 fF [118]. The bulk resistance of YSZ (R_{YSZ} , diameter of the high frequency semicircle) was again used for the calculation of the effective electrode temperature, which deviates from the set temperature as already mentioned in Sec 4.1.1. The effective electrode temperature T was again estimated from Eq. 9 and $E_a = 1.136 \pm 0.002$ eV as well as $\sigma_o = 21092 \pm 1823 \Omega^{-1}\text{cm}^{-1}$ (cf. Fig. 20). Even though Eq. 9 was derived for circular shaped electrodes acceptable estimates of electrode temperatures are also expected for the rectangular $50 \times 100 \mu\text{m}^2$ electrodes used in this study when approximating their spreading resistance by that of circular electrodes with a diameter of $80 \mu\text{m}$ (i.e. with the same electrode area). Results for different samples are listed in Tab. 6.

Table 6: Sample temperatures calculated from the averaged YSZ spreading resistance (\bar{R}_{YSZ}).

Sample	\bar{R}_{YSZ} [$10^7 \Omega$]	σ_{ion} [$10^{-6} \Omega^{-1}\text{cm}^{-1}$]	T [$^{\circ}\text{C}$]
A	2.16 ± 0.08	2.9 ± 0.2	308 ± 4
B	1.09 ± 0.04	5.7 ± 0.2	326 ± 5
C	2.60 ± 0.29	2.4 ± 0.3	303 ± 6

5.1.2 Impedance measurements under cathodic dc bias

A strong effect of a dc voltage on the electrode polarization resistance is a well-known phenomenon in electrochemistry and is related to the nonlinearity of the I- η characteristics of the electrochemical reactions at the electrodes [1]. In the impedance plot this is often reflected by a strong (nonlinear) decrease of the electrode semicircle with increasing overpotential. In Fig. 37 impedance spectra measured under different cathodic bias voltages (ranging from -2.00 to -2.50 V) are compared to spectra without additional dc voltage. The rather large scatter of the data points was caused by the extreme ratio of dc voltage (> 2 V) and ac amplitude (10 mV). As expected the electrode resistance was strongly affected by the cathodic polarization voltage. A change of

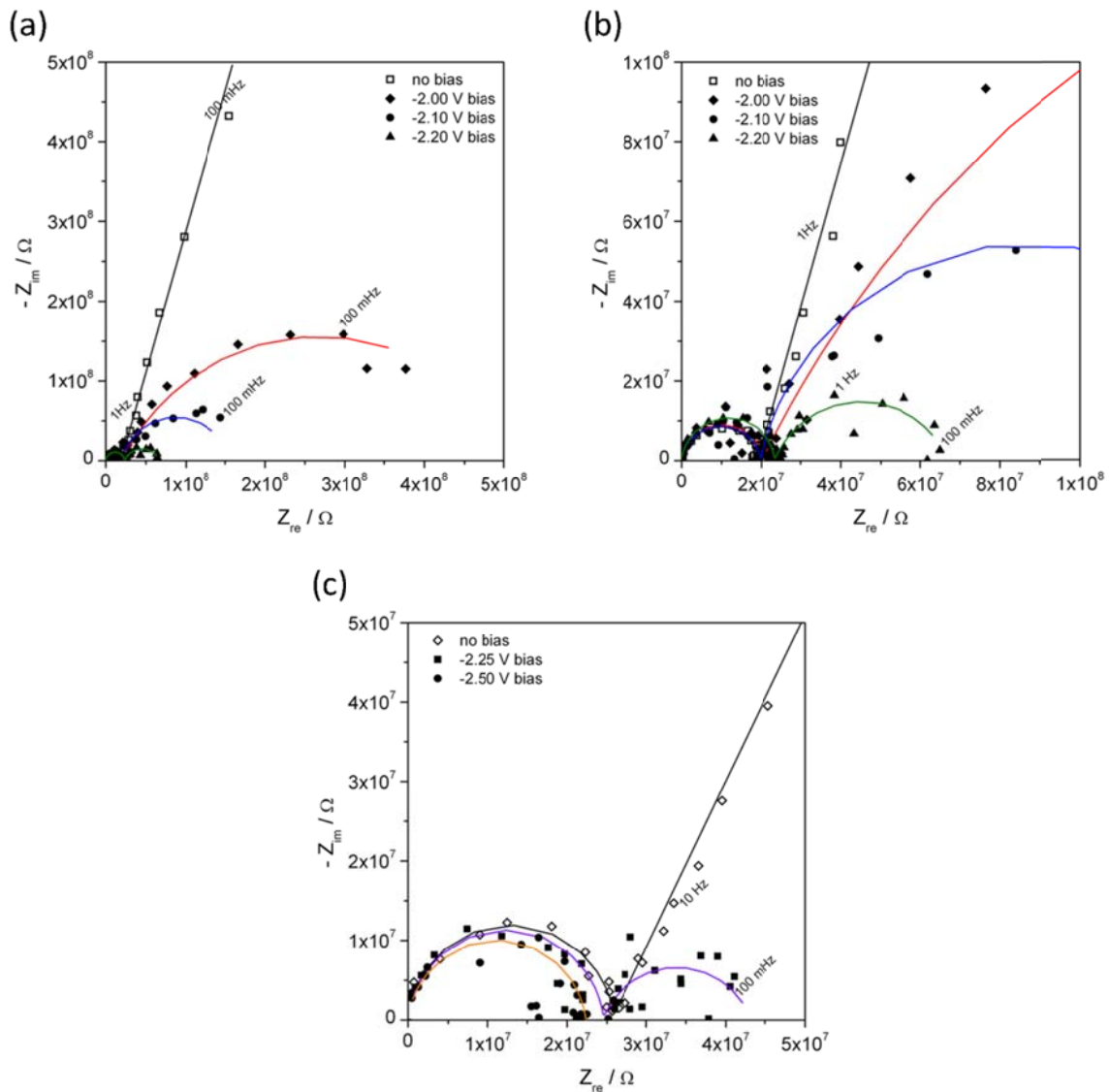


Figure 37: Impedance spectra measured under equilibrium conditions (open symbols) compared to those measured under dc bias (closed symbols). The solid lines show fit results using two serial R-CPE elements as an equivalent circuit. (a) The size of the low frequency arc and thus the polarization resistance of O_2 reduction strongly decreases with increasing bias. (b) High frequency part of the spectra in (a): the bias voltage has no effect on the YSZ bulk resistance at “lower” bias values. (c) In case of the highest polarization (-2.50 V) the bulk resistance shows a slight decrease which indicates an increase in electron concentration due to some reduction of YSZ.

100 mV in polarization from -2.00 to -2.10 V, for example, lead to a decrease of the electrode resistance by a factor of about three (cf. Fig. 37a). In case of -2.25 V bias the polarization resistance was reduced by many orders of magnitude compared to the

equilibrium state without dc bias (see Fig. 37c). However, the high frequency semicircle, which represents the bulk resistance of YSZ, was hardly affected by dc bias values of -2.25V (cf. Figs. 37b and 37c). This proves that YSZ was still almost entirely ion conducting, despite the relatively high polarization. Only in case of the highest dc bias (-2.50 V) some decrease of $R_{YSZ,bias}$ was observed which can be interpreted as the consequence of an electrochemical reduction of YSZ. The resulting increase in electron concentration leads to a parallel electronic conduction path and could thus increase the conductivity [119]. As the resistance change was only about 20 %, YSZ was still in a predominantly ion conducting regime. Alternatively the decreased bulk resistance can be attributed to an effective electrode increase due to partial reduction of YSZ, see also Sec. 5.1.3. A significant electrode arc was no longer visible at such high dc bias.

It has to be kept in mind that a fraction of the dc bias U_{set} drops in the YSZ bulk and thus U_{set} only partly affects the electrode reaction. For a calculation of the latter contribution, i.e. the electrode overpotential η , knowledge of the YSZ spreading resistance under a bias voltage of each individual polarized electrode $R_{YSZ,bias}$ is essential. The potential difference in YSZ is given by the total dc current I_{dc} times the bulk resistance of the polarized electrode $R_{YSZ,bias}$. The electrode overpotential therefore reads

$$\eta = U_{set} - I_{dc} \cdot R_{YSZ,bias} \quad (42)$$

and was calculated for each individual electrode used for tracer incorporation; $R_{YSZ,bias}$ was obtained by the impedance measurements under a bias voltage which were mentioned above.

5.1.3 Electrochemical tracer incorporation experiments

Plots of the current I_{dc} versus time t for the different dc voltages applied in this study are given in Fig. 38. In case of set voltages from -2.00 to -2.25 V the I_{dc} - t curves show the typical relaxation characteristics of R-C-elements (charging of the interfacial capacitance; see Fig. 38a). For the electrode under the highest polarization ($U_{set} = -2.50$ V; Fig. 38b) an additional change, i.e. an increase after a sharp current decrease, was observed. This may be caused by the partial reduction of YSZ which is much

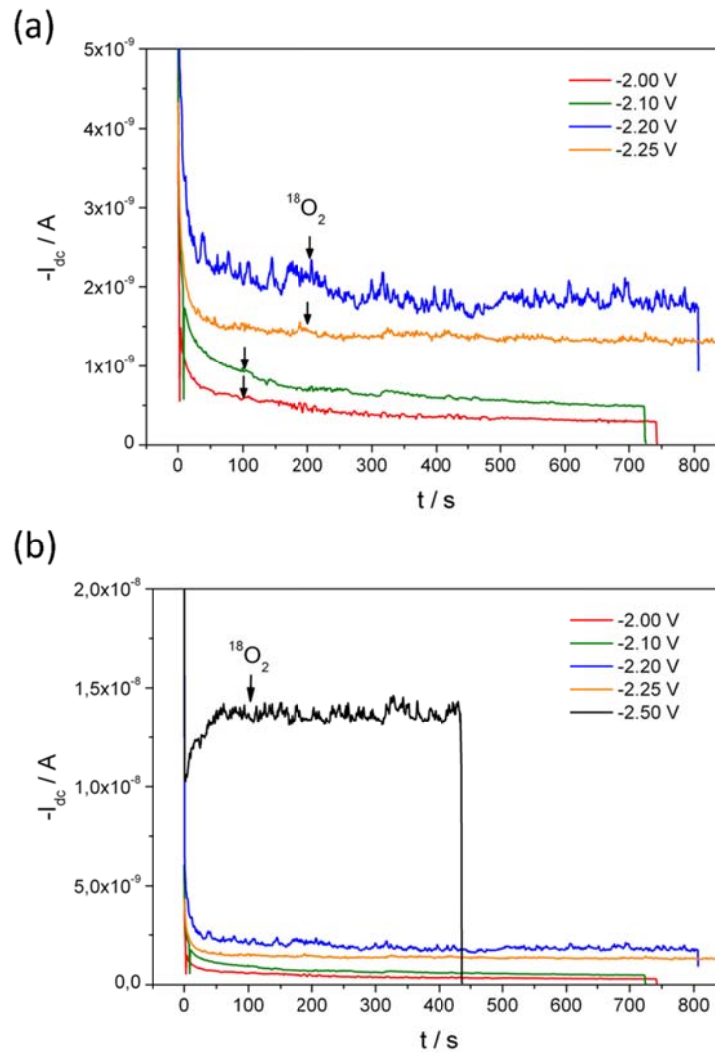


Figure 38: Time dependence of the dc current I_{dc} during incorporation experiments. (a) Current-time behavior of electrodes at polarizations where a significant YSZ reduction was not observed. The arrows indicate the point when ^{18}O incorporation was started. (b) Comparison of the curves in (a) with I_{dc} - t characteristics of the electrode with highest polarization. The increase in current during the first 50 seconds of polarization can be explained by reduction of YSZ.

slower than the double layer charging and results in an increase in electron concentration. Hence a decrease of the electrode and – to a minor degree – of the bulk resistance within the first 100 seconds of polarization was found. This change of the bulk resistance can be caused by an effective increase of the electrochemically active electrode area due to the partial reduction of YSZ. Assuming that the decrease in $R_{\text{YSZ},\text{bias}}$ in case of electrode 5 ($U_{\text{set}} = -2.50$ V) was predominantly caused by this increase of the active

area and assuming further the validity of the spreading resistance equation [100] ($R_{\text{YSZ,bias}} = 1/(4 \cdot r_{\text{ME}} \cdot \sigma)$ with r_{ME} being the active electrode radius) the 20% change in YSZ spreading resistance would be associated to an increase of the radius by about 8 μm . This corresponds well to the ^{18}O results obtained under the same conditions – see Secs. 5.2.3 and 5.2.4.

The starting time of ^{18}O supply via the capillary and thus of ^{18}O tracer incorporation is indicated by arrows in Fig. 38. The dc current during tracer incorporation was averaged over the duration of the incorporation experiment. The values obtained for I_{dc} were used to calculate the electrode overpotential by means of Eq. 42 – the results are summarized in Tab. 7. The fact that in case of -2.20 V set voltage the current was higher than for -2.25 V was most probably caused by the slightly higher sample temperature (see Fig. 38b and Tabs. 6 and 7). Fig. 38 also very clearly shows the reasons for being “constrained” to use quite high polarization values: even at these harsh cathodic conditions the resulting current was rather low at the electrode temperatures of about 300 - 330 $^{\circ}\text{C}$ used in the experiments. However, low temperatures were essential for successfully monitoring the three phase boundary width since only then tracer diffusion in YSZ could be kept at a sufficiently low level – cf. Secs. 1 and 5.2.2 as well as Ref. [88]. As a consequence it cannot be excluded, that the results of this study reflect an oxygen reduction mechanism that differs from that close to equilibrium (cf. Sec. 6).

Table 7: Calculation of the cathodic overpotentials η from the applied voltage U_{set} by subtracting the voltage drop in the electrolyte (Eq. 42). The nominally identical η for set voltages of -2.25 and -2.50 V may be due to some measurement or fitting inaccuracies.

Electrode	Sample	U_{set} [V]	$R_{\text{YSZ,bias}}$ [$10^7 \cdot \Omega$]	I_{dc} [$10^{-9} \cdot \text{A}$]	η [V]
1	A	-2.00	2.27 ± 0.32	-0.4 ± 0.1	-1.99 ± 0.01
2	A	-2.10	2.23 ± 0.26	-0.6 ± 0.1	-2.09 ± 0.01
3a	B	-2.20	1.09 ± 0.04	-1.8 ± 0.1	-2.18 ± 0.01
3b	B	-2.20	1.09 ± 0.04	-2.4 ± 0.1	-2.17 ± 0.01
4	C	-2.25	2.30 ± 0.32	-1.4 ± 0.1	-2.22 ± 0.01
5	C	-2.50	2.07 ± 0.18	-13.7 ± 0.3	-2.22 ± 0.03

5.2 ToF-SIMS results

5.2.1 Lateral ^{18}O distribution and the location of the electrochemically active zone

The ^{18}O distribution images (intensity plots) obtained by ToF-SIMS on differently polarized electrodes are shown in Fig. 39. The ^{18}O intensity is color-coded with low and high intensities being dark and white, respectively (see the vertical bar on the left hand side of Fig. 39). Images, which were recorded with the corresponding Pt electrode still remaining on top of YSZ, are given in the first line (Figs. 39a-e). The distribution plots after removal of Pt by an etching step are shown in the second line (Figs. 39f-j). A comparison of the two ^{18}O distribution images in case of lowest polarization (electrode 1) suggests that the tracer incorporation zone was beneath the platinum electrode: only after removing the electrode an ^{18}O frame was visible (compare Figs 37a and f). By a further increase of the polarization some ^{18}O also became visible in SIMS measurements with the electrode still remaining on the electrolyte. However, an additional signal could always be observed when removing the Pt thin film.

In each experiment a significant increase of ^{18}O intensity in YSZ was found only for polarized electrodes. Neighboring electrodes, which were exposed to the same thermal but no voltage treatment, did not show any evidence of ^{18}O incorporation even though they were also exposed to a substantial amount of $^{18}\text{O}_2$ during the dc experiment (in Fig. 39 electrodes below and/or above the electrode where tracer was incorporated). Effects due to purely concentration driven oxygen exchange as well as artifacts during SIMS measurements – e.g. a matrix effect [120] – can therefore be excluded as sources for the increase in ^{18}O intensity at the TPBs of polarized electrodes.

In principle, the observed difference in ^{18}O signal before and after removing the Pt electrode could be caused by two different effects: Either by transport of an ^{18}O species along the Pt|YSZ interface or by a shadowing effect caused by the geometry of the Pt thin film electrode, which could be unfavorable with respect to the incident angle of the SIMS measuring beam. In order to exclude the second interpretation, a cross-section of one of the electrodes was prepared by means of a focused ion beam. A SEM image of such a cross section at the TPB region is shown in Fig. 12d. It can be seen that

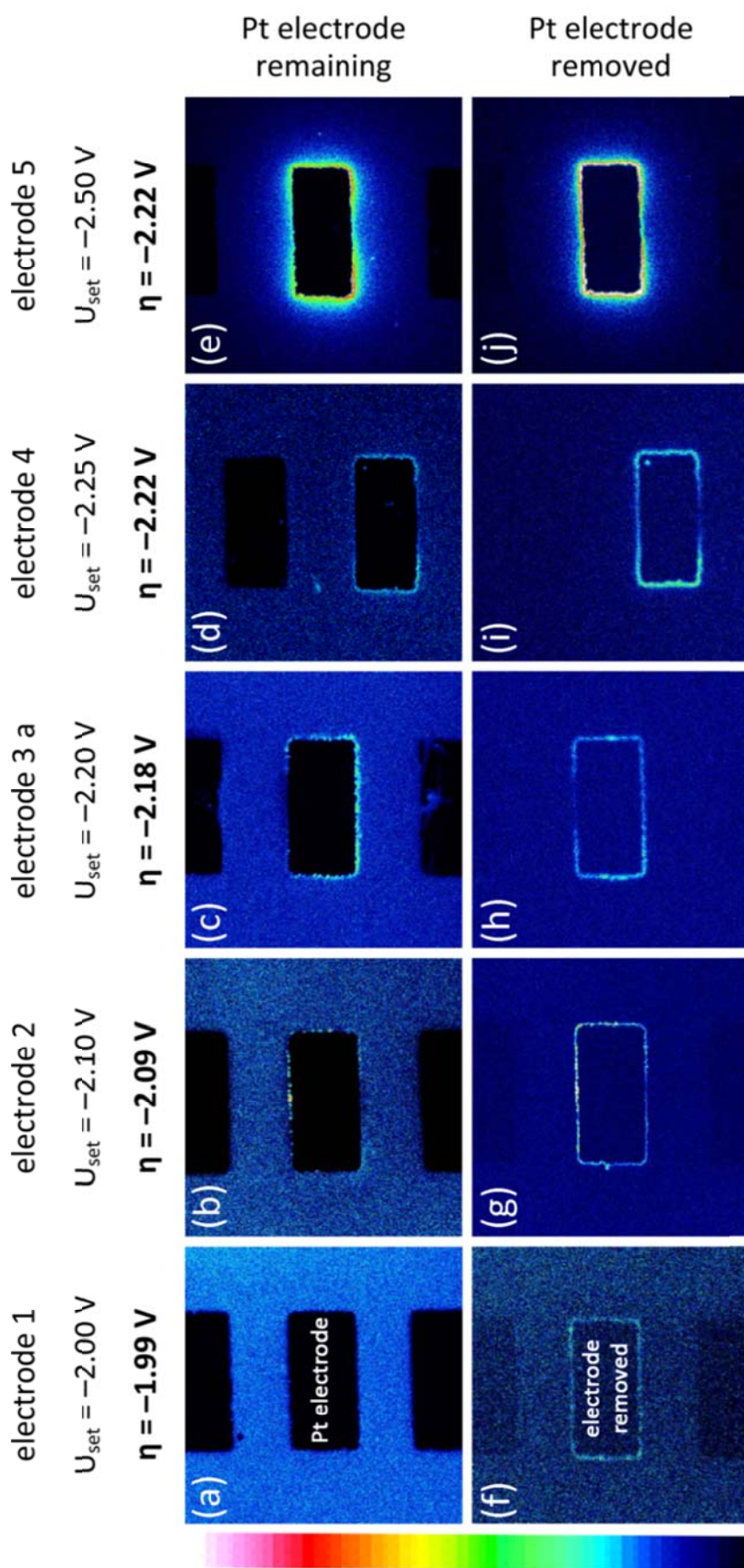


Figure 39: ^{18}O distribution images (intensity plots) of differently polarized electrodes. The ^{18}O intensity is color-coded (see the vertical bar on the left – black: low intensity, white: high intensity); the size of each image is $200 \times 200 \mu\text{m}^2$. Images in the first line were recorded with the electrode still remaining on the YSZ. (a-e), those in the second line were measured after removing the Pt thin film electrode (f-j).

the electrode|YSZ contact is established up to the edge of the Pt electrode. Indication of de-wetting of Pt close to the TPB was not found. Thus a gap along the Pt|YSZ interface, allowing gas diffusion beneath the Pt electrode, is ruled out as an explanation of the observed ^{18}O incorporation behavior. A large influence of the 45° angle of the SIMS measuring beam can be excluded as well: As the film thickness is only of about half a micrometer the resulting shadow would not be able to completely cover the profiles found after removing the electrodes. Moreover, this kind of shadowing would only occur on one side of the electrode, which is in contrast to the obtained results (The somewhat asymmetric shape of the incorporation zones in Figs. 39b and c might be attributed to this kind of shadowing effect.) Hence, it can be concluded that in case of the lowest polarization used in the study ($\eta = -1.99$ V) the electrochemically active zone is indeed located along the Pt|YSZ interface close to the TPB and oxygen was almost exclusively incorporated into YSZ beneath the platinum electrode. Such an extension of the active zone along the Pt|electrolyte two phase boundary was already suggested in Ref. [44], however, the temperatures in that study were higher (500°C) and porous Pt electrodes instead of dense ones were used.

Increasing the polarization led to a spatial extension of the electrochemically active zone along the free YSZ surface. In ToF-SIMS investigations of electrodes 2, 3a, and 4 some tracer was already detectable with the electrodes still remaining on the YSZ (see Figs. 39b-d). However, a substantial amount of ^{18}O was again found in the TPB-near zone beneath the Pt thin film. Only in case of highest polarization (electrode 5) very little (if any) extension of oxygen incorporation beneath the Pt is visible. Moreover, the highest polarization was accompanied by a significant change of the shape of the electrochemically active region. Instead of a more or less sharp frame-like appearance of the incorporation zone a corona-like image resulted. This modification of the shape of the electrochemically active zone also suggests a change of the oxygen incorporation mechanism for very high polarization. An obvious explanation for this behavior is the strong change of the electron concentration in YSZ with increasing cathodic overpotential, which is also indicated by the impedance data and dc current measurements on electrode 5. In case of electrode 1 the electron concentration in YSZ seems to be sufficiently low to not affect the usual role of electrode and electrolyte in terms of electron supply and oxide ion uptake. The strong increase of electron concentration in YSZ for very high polarization, on the other hand, allows O_2 to also be reduced on the free electrolyte surface. However, owing to the moderate electron conductivity of polarized

YSZ this zone is still restricted to a “corona” around the TPB. A similar electron supply via the electrolyte even without bias was also suggested for Bi-based solid electrolytes [25] and to a minor degree for ceria electrolytes [26]. Moreover, a role of electrons in YSZ will also be concluded in Sec. 6 for similar electrodes from current-voltage curves at higher cathodic overpotentials but higher temperatures.

5.2.2 Diffusion of the tracer in YSZ

In order to determine in how far tracer diffusion in the YSZ bulk contributes to the apparent width of the oxygen incorporation zone a depth profile of ^{18}O in YSZ was measured for -2.20 V set voltage. Distribution images obtained on electrode 3b in x-y-plane (lateral distribution) and x-z-plane (depth distribution) are shown in Figs. 40a and b, respectively. Please note the strong difference in lateral and depth axis scale of Fig. 40b – a seemingly pipe-like diffusion is not present. Rather, isotropic diffusion in cubic YSZ is found. For quantification the relative tracer concentration $c(^{18}\text{O})$ could be calculated from the intensities int of the oxygen isotopes [121, 122]

$$c(^{18}\text{O}) = \frac{\text{int}(^{18}\text{O})}{\text{int}(^{18}\text{O}) + \text{int}(^{16}\text{O})}. \quad (43)$$

A plot of the laterally integrated tracer concentration versus the depth is shown in Fig. 40c (green line). Even though integration parallel to the surface does not exactly match the integration along equi-concentration lines, a reasonable estimate of the diffusion length can be obtained from the full width at half maximum (FWHM) of this diffusion profile and a value of 0.5 μm results. Since the diffusion time was known to be 600 s (duration of the incorporation experiment), a tracer diffusion coefficient $D^* = 4.2 \cdot 10^{-12} \text{ cm}^2\text{s}^{-1}$ can be estimated from Eq. 5. Using Eq. 6 this value can be converted into an ionic conductivity of $4.7 \cdot 10^{-6} \Omega^{-1}\text{cm}^{-1}$ at a temperature of 320 °C. This agrees very well with the conductivity value obtained in impedance measurements (cf. Tab. 6, sample B and Fig. 20). Hence, the following initial assumptions were verified: i) In the present concentration range ($c(^{18}\text{O}) < 10\%$) only concentration driven diffusion leads to an unintended broadening of the incorporation zone; field driven tracer migration is

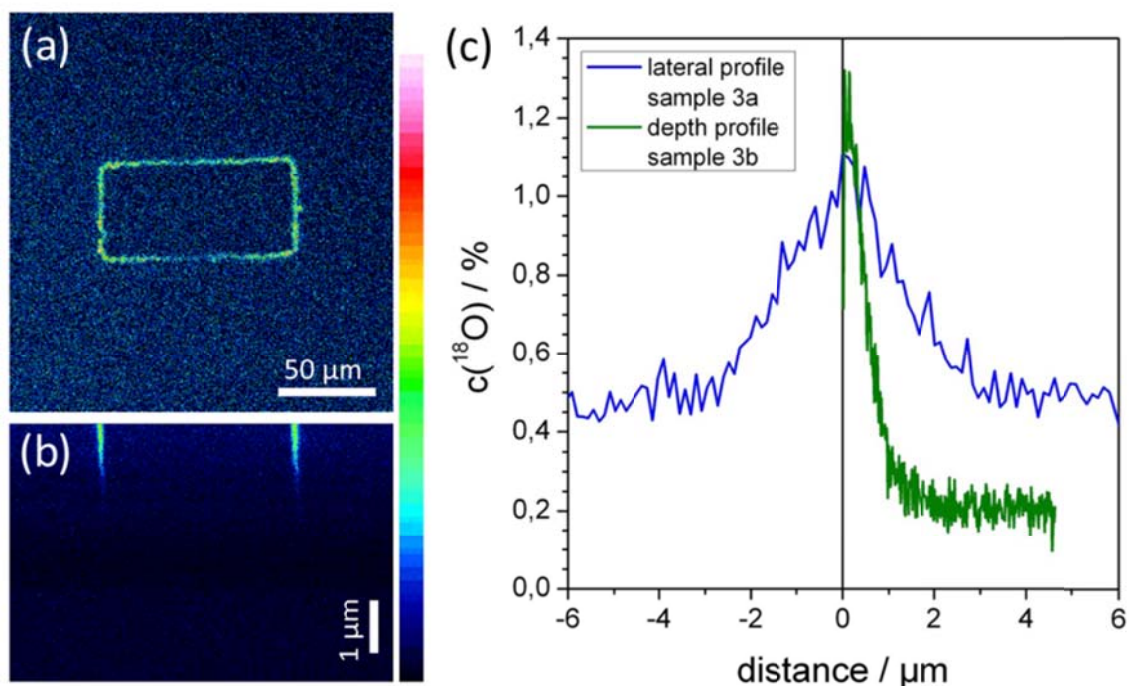


Figure 40: (a) Lateral ^{18}O distribution image (x-y-plane) of electrode 3b ($\eta = -2.17\ \text{V}$) after removing the platinum electrode. (b) Tracer depth distribution in YSZ (x-z-plane) for the same electrode. Note the different scale of lateral (x/y) and depth directions (z) – the z-direction is strongly exaggerated. (c) ^{18}O depth profile (tracer concentration plotted versus depth; green line) compared to a lateral profile (blue line) obtained for electrode 3a.

still negligible [87, 88]. ii) Diffusion is sufficiently slow to only cause a sub-micrometer broadening effect. Consequently, it is reasonable to subtract this diffusion length from the measured lateral incorporation profiles to eliminate the broadening due to ^{18}O transport in YSZ.

5.2.3 Determination of lateral profiles from ^{18}O -distribution images

For the determination of the lateral extension of the electrochemically active zone, distribution images of higher resolution ($30 \times 30\ \mu\text{m}^2$; 256×256 pixels) were used. The ^{18}O distribution at one corner of electrode 1 after removing the Pt is shown in Fig. 41a. For calculation of the relative ^{18}O concentration integration areas have to be

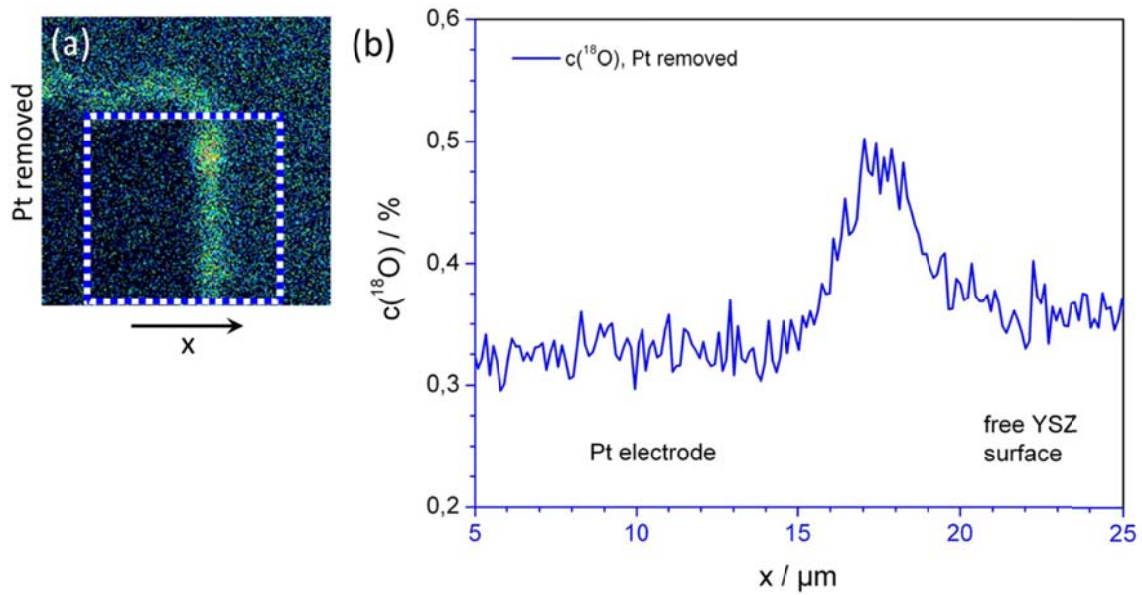


Figure 41: (a) ^{18}O distribution image focusing on one corner of electrode 1 after removing the Pt thin film (image size $30 \times 30 \mu\text{m}^2$). The area inside the blue dotted box was used for determining the lateral profile. (b) Concentration plot calculated from the box in (a) showing the lateral distribution of ^{18}O along the Pt|YSZ interface and the free YSZ surface.

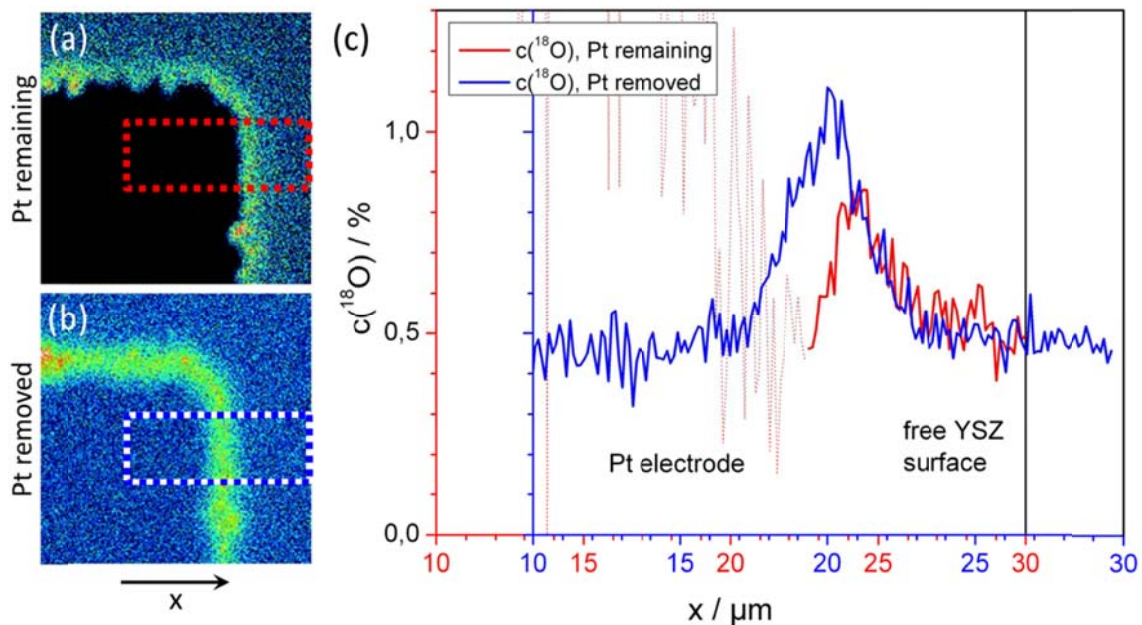


Figure 42: (a) ^{18}O distribution image of one corner of electrode 3a with the Pt electrode still remaining on the YSZ single crystal and (b) after removing the Pt thin film (image sizes $30 \times 30 \mu\text{m}^2$ each). (c) Lateral distribution of ^{18}O (concentration plot) calculated from the areas inside the dotted boxes in (a): red and (b): blue. A shift of the peak position towards the region initially covered by Pt is obvious.

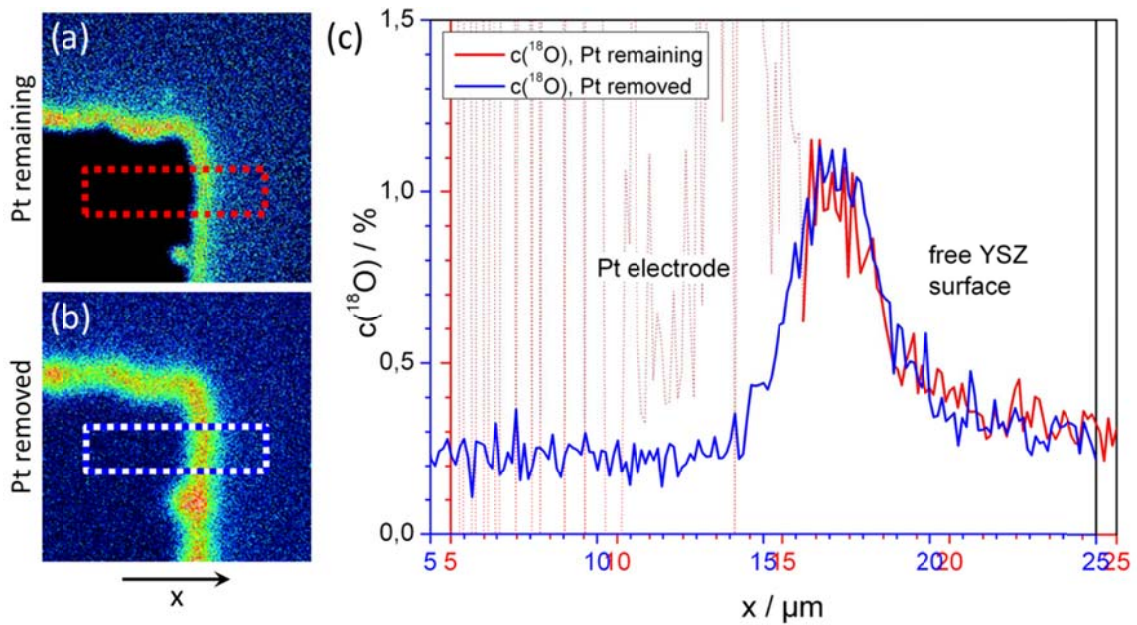


Figure 43: (a) ^{18}O distribution image of one corner of electrode 4 with the Pt electrode still remaining on the YSZ single crystal and (b) after removing the Pt thin film (image sizes $30 \times 30 \mu\text{m}^2$ each). (c) Lateral distribution of ^{18}O (concentration plot) calculated from the areas inside the dotted boxes in (a): red and (b): blue. Peak positions are almost identical. Only the left shoulder of the peak was initially covered by the platinum electrode.

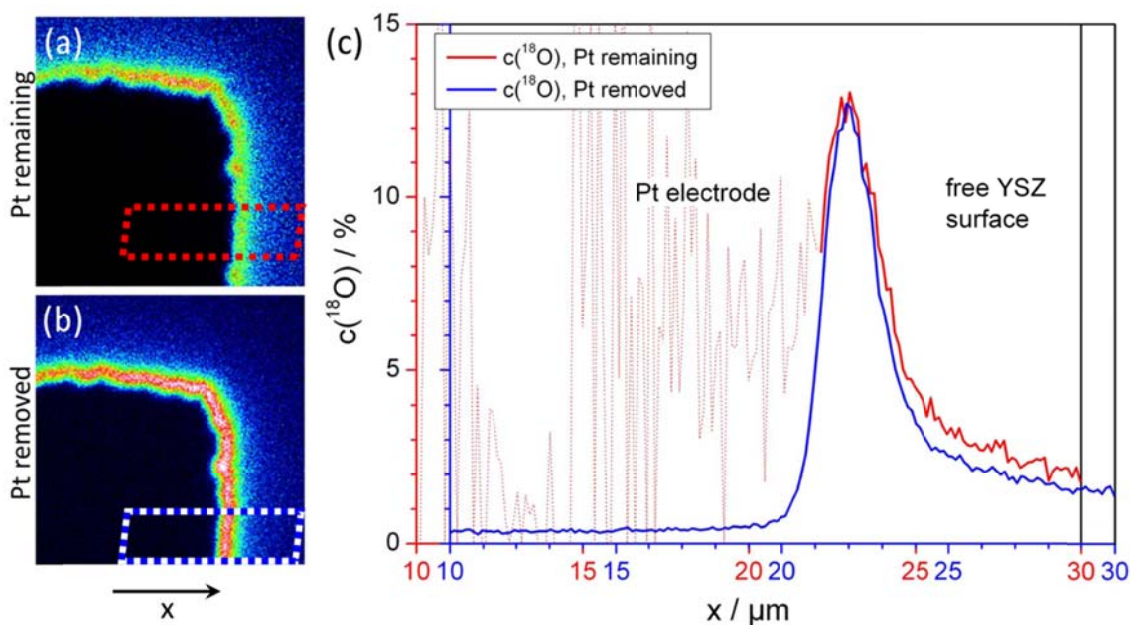


Figure 44: (a) ^{18}O distribution image of one corner of electrode 5 with the Pt electrode still remaining on the YSZ single crystal and (b) after removing the Pt thin film (image sizes $30 \times 30 \mu\text{m}^2$ each). The rhomboid shape of the integration areas accounts for the slightly tilted position of the sample. (c) Lateral distribution of ^{18}O (concentration plot) calculated from the areas inside the dotted boxes in (a): red and (b): blue. Peak positions and shapes are virtually identical.

summed up along the vertical (y) direction and related to the total oxygen intensity (cf. Eq. 43). These normalized values plotted versus the horizontal (x) axis are shown in Fig. 41b for electrode 1. The same procedure was applied to calculate the lateral profiles for the other polarized electrodes (see Figs. 42, 43, and 44). For three electrodes (3a, 4, 5) lateral profiles were determined from distribution images before and after removing the Pt electrode (part c of Figs. 42-44). In profiles calculated from the distribution images with remaining Pt electrodes the part of the profile corresponding to the electrode surface is characterized by a strong scattering. This is caused by a very low signal to noise ratio on the Pt surface. Hence, the corresponding part of the profile is not reliable and therefore only given by a thinner dashed line.

In order to compare concentration plots before and after electrode removal a lateral shift of the distribution images (caused by removal of the samples from the SIMS measurement chamber for etching) had to be compensated. Overlap of the outer part of the profiles was assumed to indicate the correct positions. These plots further quantify the trends already visible in the ^{18}O images: For “smaller” overpotentials the ^{18}O incorporation almost exclusively (electrode 1) or predominantly (electrode 3) occurs beneath the Pt electrode. Figure 42 clearly shows that the maximum of the ^{18}O profile became only visible after removing the Pt electrode. However, the electrochemically active zone extends along the free YSZ surface with increasing polarization (see Figs. 43 and 44). Moreover, a shift of the zone with highest oxygen incorporation rate (i.e. the maximum in the concentration profile) towards the free surface with increasing polarization becomes obvious.

5.2.4 The width of the electrochemically active zone (“TPB width”)

In order to quantify the width of the electrochemically active zone at the TPB the FWHM-values of the lateral profiles were determined from the concentration plots in Figs. 41 – 44. As already discussed in Sec. 5.2.2 tracer diffusion in YSZ caused some broadening of the lateral incorporation profile. This broadening (green profile in Fig. 40c) is much smaller than the FWHM b_{tot} of the measured lateral incorporation profiles ($\sim 3 \mu\text{m}$). Hence, a subtraction of twice the diffusion length of $0.5 \mu\text{m}$ from lateral profiles measured after removal of the Pt electrode is expected to yield the true width b_{eff} of the electrochemically active zone. In Tab. 8 the results of this analysis are

summarized. The highly polarized electrode 5 exhibited a significantly different incorporation profile than the other electrodes: A relatively sharp decay is followed by a long tail along the free YSZ surface with only slowly decreasing incorporation activity (cf. Fig. 44c). The nominal FWHM obtained from electrode 5 is thus not sufficient for describing this strongly asymmetrical profile. However, the significant broadening of the active zone fits quite well to the decrease in the spreading resistance corresponding to the increase of the effective electrode “radius” by 8 μm discussed in Sec. 5.1.3.

For a final interpretation of the resulting “TPB widths”, also the geometrical shortcomings of the electrodes have to be considered, namely their slightly wavy edge. It was already tried to minimize this effect by selecting the least wavy sections as integration areas for profile calculation. A precise quantification of the apparent broadening due to non-straight electrode edges is difficult but its contribution is in the worst case around half a micrometer. As a consequence, even for this extreme case of a geometry-caused apparent broadening of 0.5 μm , it can be concluded from all measurements that the true width of the incorporation zone ($b_{\text{TPB}} = b_{\text{eff}} - 0.5 \mu\text{m}$) is between 1.0 and 1.3 μm . This is much more than most TPB widths estimated so far [43, 62, 81]. In how far the high polarization values strongly broaden the electrochemically active-zone (even without incipient electron conduction) cannot be concluded from these experiments. Neither can be decided whether the same rate limiting step as close to equilibrium determined the kinetics of these experiments. In Sec. 6 results will be discussed which suggest different rate limitations for high and low polarization.

Table 8: The width b of the electrochemically active zone of differently polarized electrodes: FWHM values $b_{\text{free YSZ}}$ and b_{tot} were determined from Figs. 41 – 44 with the electrode still remaining and after removal of the Pt electrode, respectively. The corrected values ($b_{\text{eff}} = b_{\text{tot}} - 2 \cdot L_{\text{diff}}$) were obtained after subtraction of the contribution caused by diffusion. In case of electrode 5 the TPB width determined from the FWHM is not comparable to the others, since the shape of the lateral profile is more complex.

Electrode	$b_{\text{free YSZ}}$ [μm]	b_{tot} [μm]	b_{eff} [μm]	b_{TPB} [μm]
1	—	2.6	1.6	1.1
3a	1.8	2.5	1.5	1.0
4	2.1	2.8	1.8	1.3
(5)	(1.9)	(2.0)	(1.0)	—

5.2.5 Bulk path versus surface path

The increase of ^{18}O concentration at the free YSZ surface (cf. 0.2 % natural abundance of ^{18}O) can be explained by conventional tracer exchange at oxide surfaces [123]. However, the enhanced ^{18}O concentration in the entire region initially covered by the Pt electrode (0.25 - 0.45 %) is not that self-explanatory. This ^{18}O increase is not a simple SIMS artifact but followed by a diffusion profile in YSZ bulk: In Fig. 45a the ^{18}O distribution image of electrode 3b ($\eta = -2.17$ V, $T = 326$ °C) after removing the Pt electrode is shown. The relative tracer concentration $c(^{18}\text{O})$ was calculated from the intensities of the oxygen isotopes in the distribution plot by Eq. 43. A plot of the laterally integrated tracer concentrations versus the sputter depth is depicted in Fig. 45b and acceptable diffusion profiles were obtained for the TPB zone (green dashed line, corresponding to the difference between white and orange integration area in Fig. 45a) and for the electrode area (orange solid line, corresponding to the orange integration area). The surface concentration in the electrode area (which was completely covered by a gas-tight Pt film during the incorporation experiment) was increased from 0.2 % (natural abundance of ^{18}O) to 0.3 – 0.4 % – see orange depth profile in Fig. 45b and lateral profile in Fig. 46b. Hence, since the increased surface concentration along the entire electrode area was also followed by a diffusion profile in YSZ, a SIMS artifact could be excluded as the source for the increase in ^{18}O concentration beneath the electrode.

Even though this phenomenon is not in the main focus of this section, a brief discussion should be given. A possible mechanism leading to an ^{18}O enriched YSZ|Pt interface is oxygen diffusion through the Pt thin film. Despite bulk platinum is commonly accepted to not dissolve significant amounts of oxygen [4, 19-21], there exists some evidence that very thin platinum films indeed are permeable for oxygen [33, 34]. The quite high polarization values in the experiments may also contribute to a significant transport of oxygen through the thin film. However, this explanation would implicate that the total oxygen reduction current includes contributions from the surface path (via the TPB) and the bulk path (through the electrode). In terms of an equivalent circuit, two electrochemical resistors in parallel would be suitable in the simplest case (cf. Fig 46c). Hence, a straightforward separation of both paths by means of impedance spectroscopy is not possible. Tracer incorporation experiments, however, are feasible for separation and even for quantification of the two different reaction

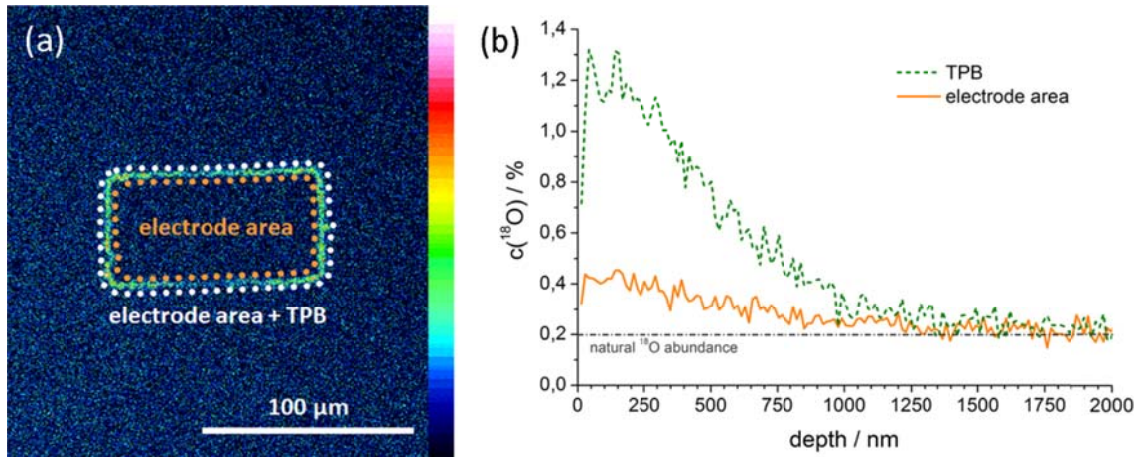


Figure 45: (a) Distribution of ^{18}O in YSZ at electrode 3b ($\eta = -2.17\text{ V}$, $T = 326\text{ }^\circ\text{C}$). The green frame-shaped area reflects high intensities of ^{18}O close to the TPB (cf. Fig. 39h). The dotted boxes indicate different integration areas. (b) The integrated intensity was converted into a concentration (Eq. 43) and plotted versus the sputter depth (z-direction) to obtain depth profiles. The orange depth profile corresponds to the orange integration area in (a) whereas the dashed green depth profile of the TPB region corresponds to the difference of white minus orange integration area.

pathways. For a first estimate the increase in tracer surface concentration $\Delta c(^{18}\text{O}) = c(^{18}\text{O}) - 0.002$ is assumed to be proportional to the electric current density $i_{dc} = I_{dc}/A$ of the corresponding reaction path:

$$\Delta c(^{18}\text{O}) \propto \frac{i_{dc} \cdot t}{ze_0}. \quad (44)$$

Consequently the relation of the amount of tracer incorporated close to the TPB and along the entire Pt|YSZ interface reflects the relation of the currents via the surface and the bulk path, and thus of the corresponding polarization resistances of the surface path (R_{TPB}) and the bulk path ($R_{Pt|YSZ}$):

$$\frac{\Delta c(^{18}\text{O})_{TPB} \cdot A_{TPB}}{\Delta c(^{18}\text{O})_{Pt|YSZ} \cdot A_{Pt|YSZ}} = \frac{I_{dc,TPB}}{I_{dc,Pt|YSZ}} = \frac{R_{Pt|YSZ}}{R_{TPB}}. \quad (45)$$

The electrochemically active YSZ surfaces in case of TPB-incorporation (A_{TPB}) and in

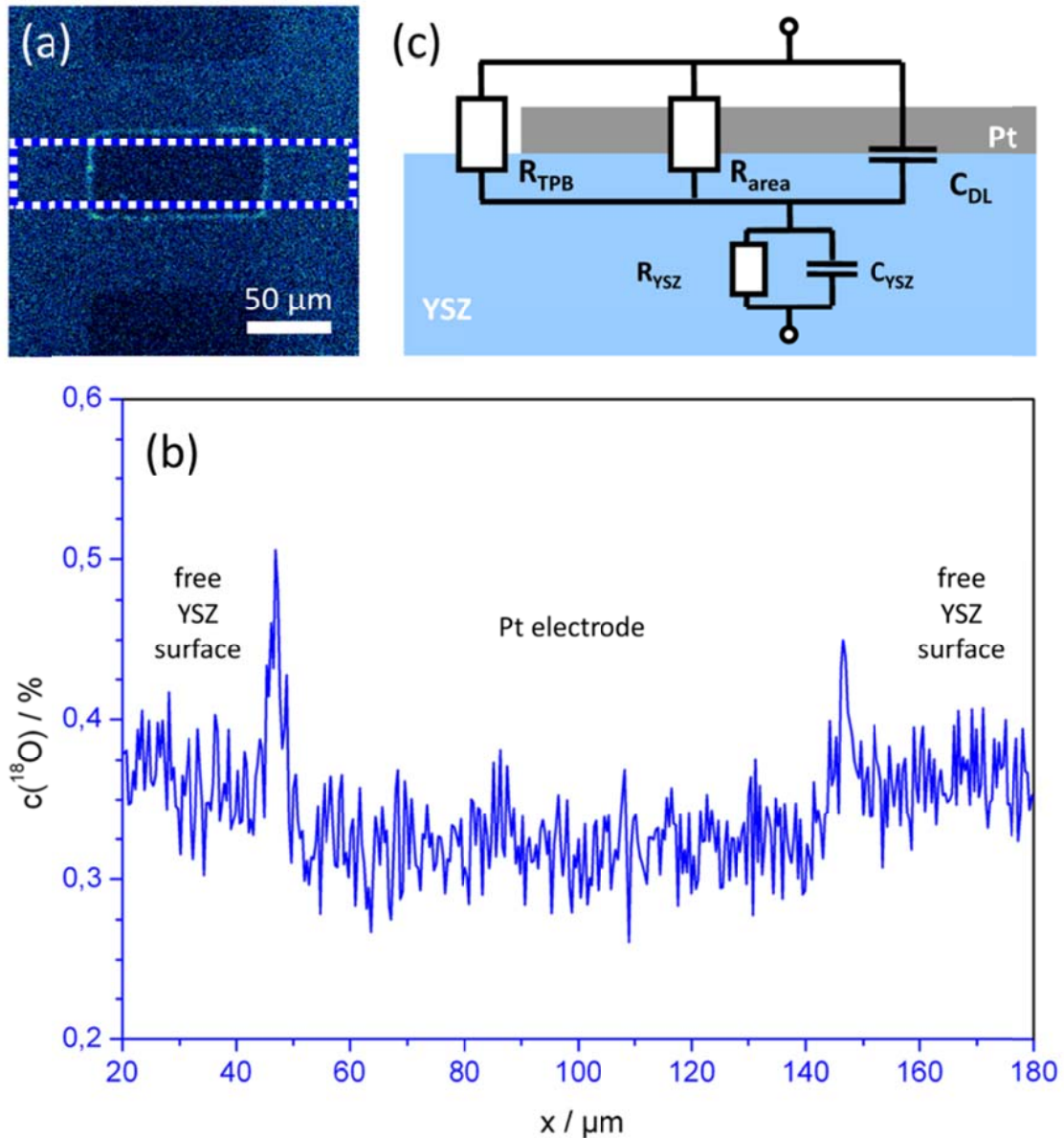


Figure 46: (a) ^{18}O distribution image of electrode 3a (cf. Fig. 39h) with the integration area for the calculation of the profile in (b) where the concentration (calculated by means of Eq. 43) is plotted versus the lateral position. (c) Equivalent circuit reflecting oxygen incorporation via two parallel paths i.e. two parallel resistive processes.

case of a Pt bulk path ($A_{\text{Pt/YSZ}}$) were approximated as areas with $300 \times b_{\text{tot}} \mu\text{m}^2$ (for b_{tot} see Tab. 8) and $100 \times 50 \mu\text{m}^2$, respectively. Thus they differ by a factor of about six. A comparison of the results is given in Tab. 9. Provided that the enhanced ^{18}O concentra-

tion along the Pt|YSZ interface is indeed due to a bulk path, this means that at lower polarization values the Pt-bulk path carries approximately three to four times more current than the surface path via the TPB. Only for the two highest polarization values a distinct change in favor of the surface path (via the TPB) was found. This pronounced role of the bulk-path is partly related to the extreme aspect ratios of the electrodes ($100 \times 50 \mu\text{m}^2$ area and only about 500nm thick). Extrapolating this to equilibrium conditions an area-related behavior of the electrode polarization resistance would not be surprising for the low temperature range used in the present impedance study.

This interpretation does not conflict with the quantitative analysis of the TPB width: Both paths are in parallel and all information given on the surface path is still valid. However, this interpretation would suggest that in case of electrodes 1 – 3 an elementary step being part of the Pt-bulk path (through the Pt electrode) is rate determining and a polarization resistance proportional to the inverse electrode area would be expected. In impedance measurements on low temperature prepared electrodes indeed an area-related polarization resistance in parallel to a TPB process was observed at comparable temperatures (cf. Sec. 4.2). The rate limiting step of this process was discussed in Sec. 4.2.5 to be oxygen diffusion along Pt grain boundaries.

Table 9: Comparison of amounts of tracer incorporated via the surface (TPB) or the bulk path (Pt|YSZ interface) of the Pt thin film electrodes.

	electrode 1		electrode 3a		electrode 4		electrode 5	
	TPB	Pt YSZ interface	TPB	Pt YSZ interface	TPB	Pt YSZ interface	TPB	Pt YSZ interface
$c(^{18}\text{O})$	0.0041	0.0033	0.0079	0.0045	0.0070	0.0023	0.0652	0.0037
$\Delta c(^{18}\text{O})$	0.0021	0.0013	0.0059	0.0025	0.0050	0.0003	0.0632	0.0017
$\Delta c(^{18}\text{O}) \cdot A [\mu\text{m}^2]$	1.64	6.50	4.43	12.50	4.20	1.50	37.92	8.50
$\frac{I_{\text{dc,TPB}}}{I_{\text{dc,Pt YSZ}}}$	0.25		0.35		2.80		4.46	

6 Results and Discussion of dc Measurements

6.1 Parameterization of dc data

The dc measurements were performed by the method described in Sec. 2.2.3 on high temperature deposited Pt electrodes (circular shape; $d_{ME} = 100 \mu\text{m}$). In order to obtain the overpotential η of the Pt electrode the contribution of the ohmic overpotential caused by YSZ has to be subtracted (cf. Eq. 42). However, since the voltage drop in the electrolyte was 0.1 mV or lower in all dc measurements in the investigated temperature range $U_{set} \approx \eta$ can safely be assumed. The overpotential at the counter electrode is negligible due to its orders of magnitude larger size compared to the microelectrode (0.0079 mm² dense vs. ~ 10 mm² porous paste) [74, 75].

In Figs. 47a and 48a current-overpotential curves obtained at different temperatures are depicted. Each curve shows one voltage cycle with the following sequence: 0.0 V \rightarrow -1.5 V \rightarrow +0.1 V \rightarrow 0.0 V. The reason for not increasing anodic overpotentials beyond +0.1 V was avoidance of irreversible morphology changes of the Pt electrodes such as bubble formation [49]. In the anodic region under investigation an exponential increase of the current was found. In the cathodic part of the curve, after a first increase the current seems to be almost constant despite increasing polarization and only for very high polarizations (voltages below -1 V) an exponential relationship between overpotential and current can be observed. Figs. 47b and 48b show the I- η characteristics at lower polarization (between +0.1 and -1.0 V) and the curves exhibit the characteristic shape of mass transport limited kinetics with a limiting current [1]. Quite similar current-voltage behavior was already reported in literature [40, 42, 44, 53] for different Pt electrodes (porous paste or point electrodes from Pt wire) on YSZ at lower cathodic polarization values manifested by a decreasing slope in I- η plots when

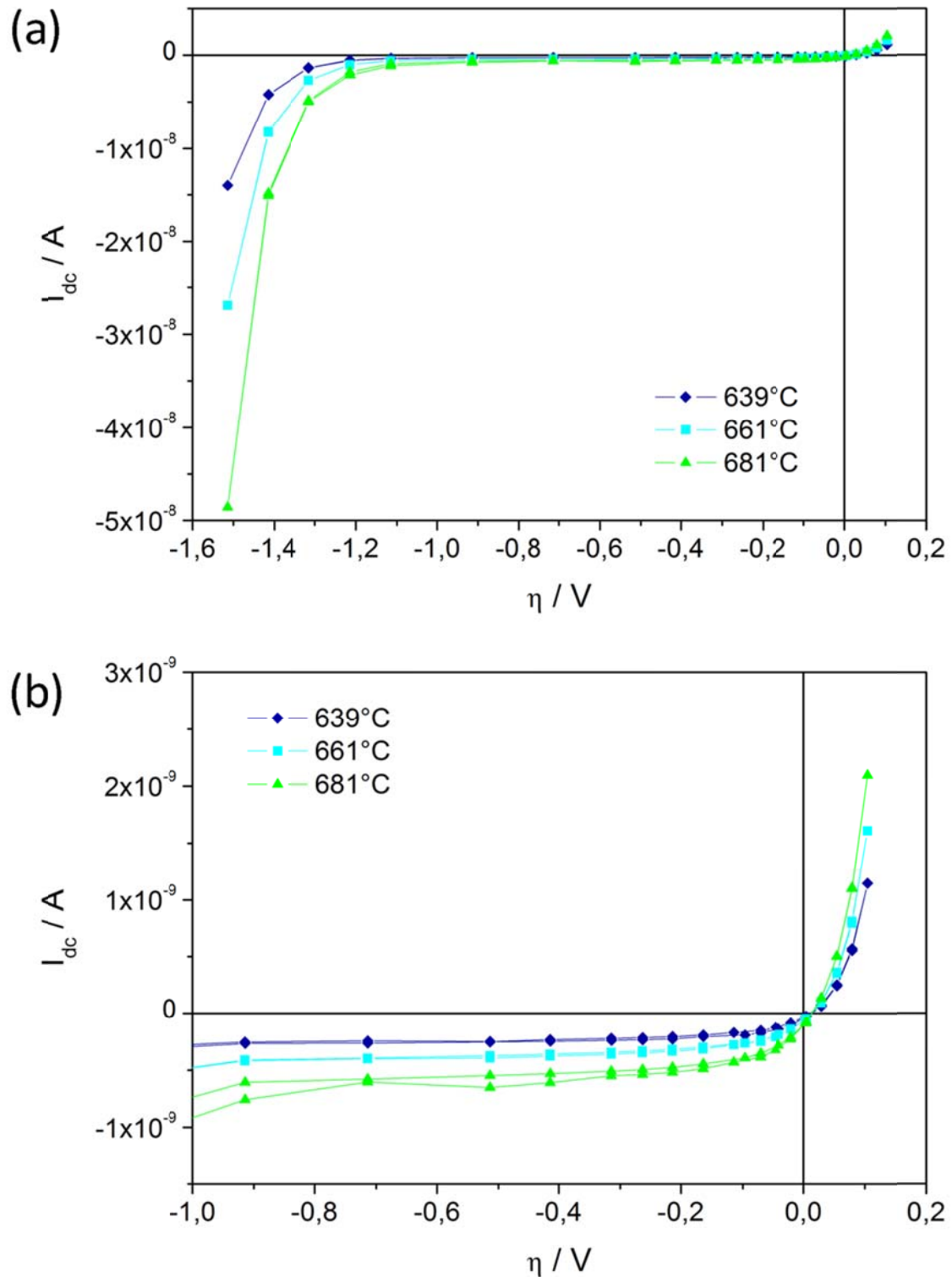


Figure 47: (a) Current-overpotential curves measured on 100 μm electrodes at 639 °C (dark blue diamonds), 661 °C (light blue squares), and 681 °C (green triangles). The given temperatures represent corrected values (cf. Sec. 4.1.1) (b) Magnification of the less polarized part of the curves in (a).

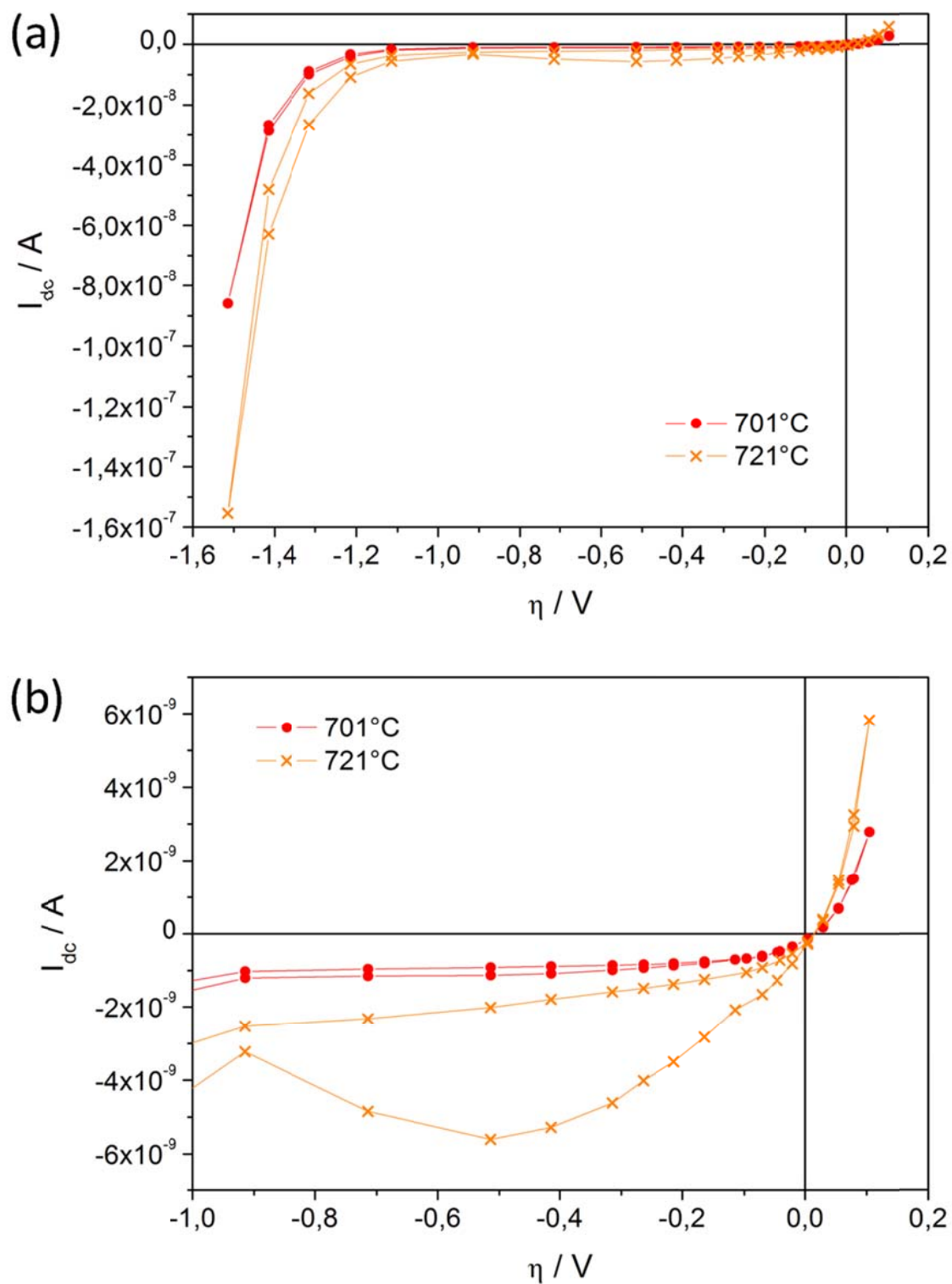


Figure 48: (a) Current-overpotential curves measured on 100 μm electrodes at 701 $^{\circ}\text{C}$ (red circles), and 721 $^{\circ}\text{C}$ (orange crosses). The given temperatures represent corrected values (cf. Sec. 4.1.1) (b) Magnification of the less polarized part of the curves in (a).

the cathodic polarization is increased. An additional exponential current-overpotential relationship at high polarization, however, was not mentioned in these studies. In the present experiments identical I - η curves could be obtained repeatedly at temperatures up to ca. 700 °C (corrected temperature; cf. the algorithm in Sec. 4.1.1). At higher temperatures, however, some irreversible changes of the electrodes during the measurements became obvious – see Fig. 48b, 721 °C curve. Hence, the analysis of dc data was limited to measurements without such irreversible effects (usually below ~700 °C). The irreversible behavior at higher temperatures might for example be attributed to changes (e.g. migration) of impurities at the TPB of the Pt electrodes during polarization [56, 93] or to decomposition of a PtO_x “phase” [42, 67]. However, it was not further investigated in the present study.

The observed electrode characteristics with a limiting current at lower polarization and an exponential current-voltage relationship at high polarization constitutes a quite unusual situation. Much more common would be the reverse case with Butler-Volmer-type kinetics at low polarization followed by a mass transport limitation when the polarization is increased. The latter situation could be described by a serial connection of the two processes. In the present case, however, a parallel connection of two reaction paths is more appropriate to explain the observed shape of the I - η curves: A rate limiting concentration polarization step leading to a limiting current in one path and an exponential process determining the current of the second path. In Sec. 4.2.5.1 a pretty low adsorption resistance of oxygen on Pt was estimated from adsorption kinetics data ($7.9 \cdot 10^{-10} \Omega\text{m}^2$) and hence a diffusion process being responsible for the mass transport limited kinetics of the path dominating at lower polarization is assumed in the following. The current-overpotential relation for simple diffusion limited kinetics and an exponential current-voltage relation in the cathodic region are given by Eqs. 46 and 47, respectively [1]:

$$I_{diff} = I_{lim} \cdot \left(1 - e^{-\frac{z_{diff} e_0}{k_B T} \eta} \right) \quad (46)$$

$$I_{exp} = -I_0 \cdot \left(e^{-\frac{b \cdot e_0}{k_B T} \eta} \right). \quad (47)$$

In Eq. 46 I_{diff} denotes the resulting diffusion current at an overpotential η , I_{lim} is the limiting current, and z_{diff} the number of charges transferred by the diffusing particle. In Eq. 47 I_{exp} denotes the current exponentially depending on the overpotential and I_0 and b are fitting parameters. The total current I_{dc} resulting from a parallel connection of both processes is given by

$$I_{dc} = I_{diff} + I_{exp}. \quad (48)$$

To account for voltage shifts caused by the thermovoltage U_{therm} mentioned in Sec. 2.2.2 Eqs. 46 and 47 were further modified and insertion in Eq. 48 yields

$$I_{dc} = I_{lim} \cdot \left(1 - e^{\frac{z_{diff}e_0}{k_B T}(\eta - U_{therm})} \right) - I_0 \cdot \left(e^{\frac{b \cdot e_0}{k_B T}(\eta - U_{therm})} \right). \quad (49)$$

In the fitting procedure I and η were used as dependent and independent variable, respectively and the fitting parameters were I_{lim} , I_0 , z_{diff} , and b . The value for the thermovoltage was measured before each dc measurement and used as a constant in the fit. Parameter T was the corrected electrode temperature (see Sec. 4.1.1). The resulting fit curves are compared with two different measurements in Figs. 49 (661 °C) and 50 (701 °C) and reflect a satisfying description of the experimental data.

6.2 Diffusion limited kinetics

The fitting results of parameter I_{lim} are shown in the Arrhenius plot in Fig. 51a with different symbols for measurements on different electrodes. The values obtained on each electrode show acceptable Arrhenius type behavior. They exhibit similar activation energies (i.e. similar slopes in the plot) with an average value of 1.57 ± 0.17 eV. This value is also in reasonable agreement with the activation energies of the polarization resistances measured at comparable temperatures by impedance spectroscopy (cf. Secs. 4.1.3.1 and 4.2.4 as well as Tabs. 4 and 5). However, the absolute I_{lim} values obtained on different electrodes show significant scattering. This might be related to the

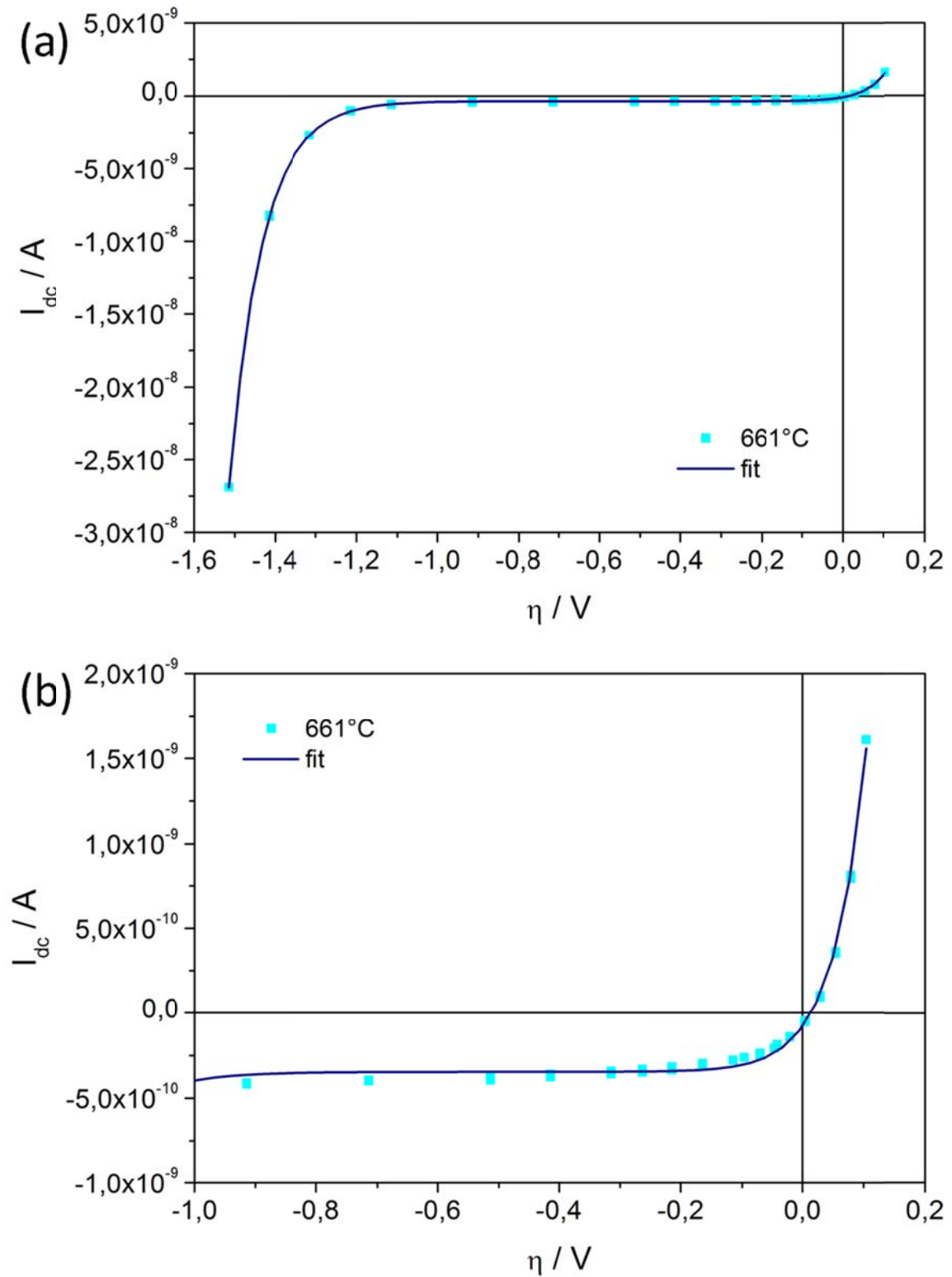


Figure 49: The $661^\circ C$ curve from 43 together with its fit curve according to Eq. 49. (a) Entire measured voltage range. (b) Diffusion dominated part at lower polarization.

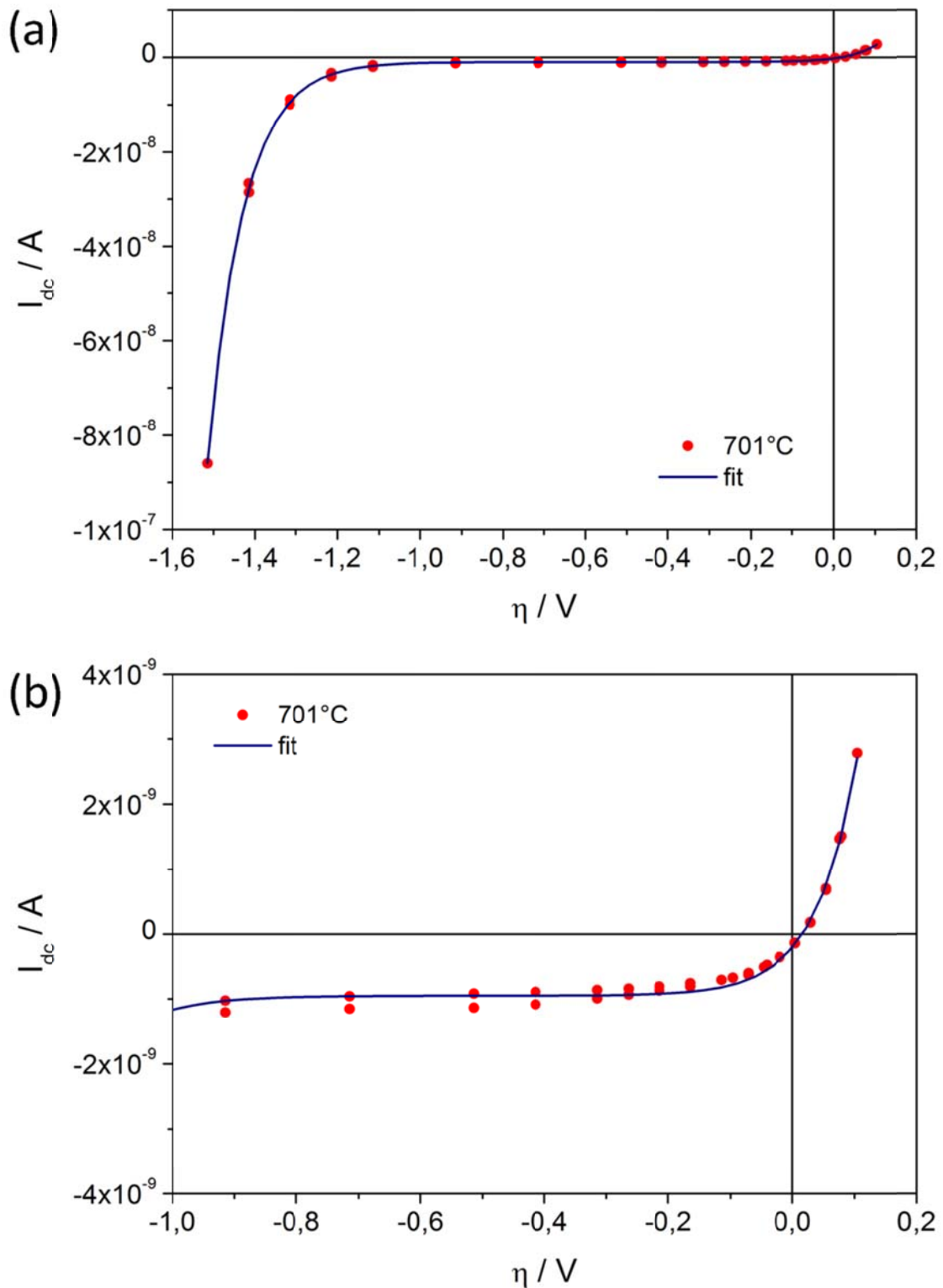


Figure 50: The $701^\circ C$ curve from Fig. 48 together with its fit curve according to Eq. 49. (a) Entire measured voltage range. (b) Diffusion dominated part at lower polarization.

nature of the diffusion limitation. In Sec. 4.2.5.2 the TPB-related polarization resistance of Pt electrodes was discussed to be possibly caused by impurities at the TPB [93]. Assuming such a TPB-blocking impurity phase as the origin for the diffusion limitation on the Pt electrodes, the limiting current would not only depend on the geometry of the electrode but also on the geometry and the composition of the impurity “rim” at the TPB. Changes in the thickness of such an impurity “rim” would thus affect the limiting current.

In Refs. [50, 117] Si containing impurities were shown to strongly affect oxygen exchange kinetics of Pt electrodes on YSZ. Moreover, in Ref. [50] it was demonstrated that electrodes, which were free of Si, exhibited tremendously lower polarization resistances than Si containing ones. In that study the polarization resistances of the Si-contaminated electrodes also exhibited notable variation, whereas the polarization resistances of Si free electrodes provided significantly less scattering. Also in the impedance measurements on similarly prepared Pt electrodes in Sec. 4.1 a remarkable scattering of the polarization resistances could be observed (cf. Fig. 21). Since the electrode polarization resistance (which is usually obtained by impedance measurements) is proportional to the inverse slope of the current voltage curves it reflects the same electrochemical process. Impurities at the TPB, which potentially hinder the oxygen exchange reaction at the TPB, would thus show the same effect on impedance measurements around equilibrium as on the limiting current in the present study. Different thicknesses, morphologies, porosities, or compositions of an impurity phase at the TPB of different electrodes would consequently lead to varying results.

Since the exchange current of the exponential-type reaction (Eq. 47) is orders of magnitude lower than the diffusion current, the polarization resistance around equilibrium $R_{ac,eq}$ can simply be obtained by differentiation of the diffusion related part of Eq. 49

$$\frac{1}{R_{ac,eq}} = \left. \frac{dI_{diff}}{d\eta} \right|_{\eta=U_{therm}} = I_{lim} \cdot \frac{z_{diff} e_0}{k_B T} \cdot e^{\frac{z_{diff} e_0}{k_B T} (\eta - U_{therm})} \bigg|_{\eta=U_{therm}} = I_{lim} \cdot \frac{z_{diff} e_0}{k_B T}. \quad (50)$$

The resulting inverse polarization resistances close to equilibrium were normalized to the TPB length of the electrodes and compared in Fig. 52 with the Arrhenius-fit of the

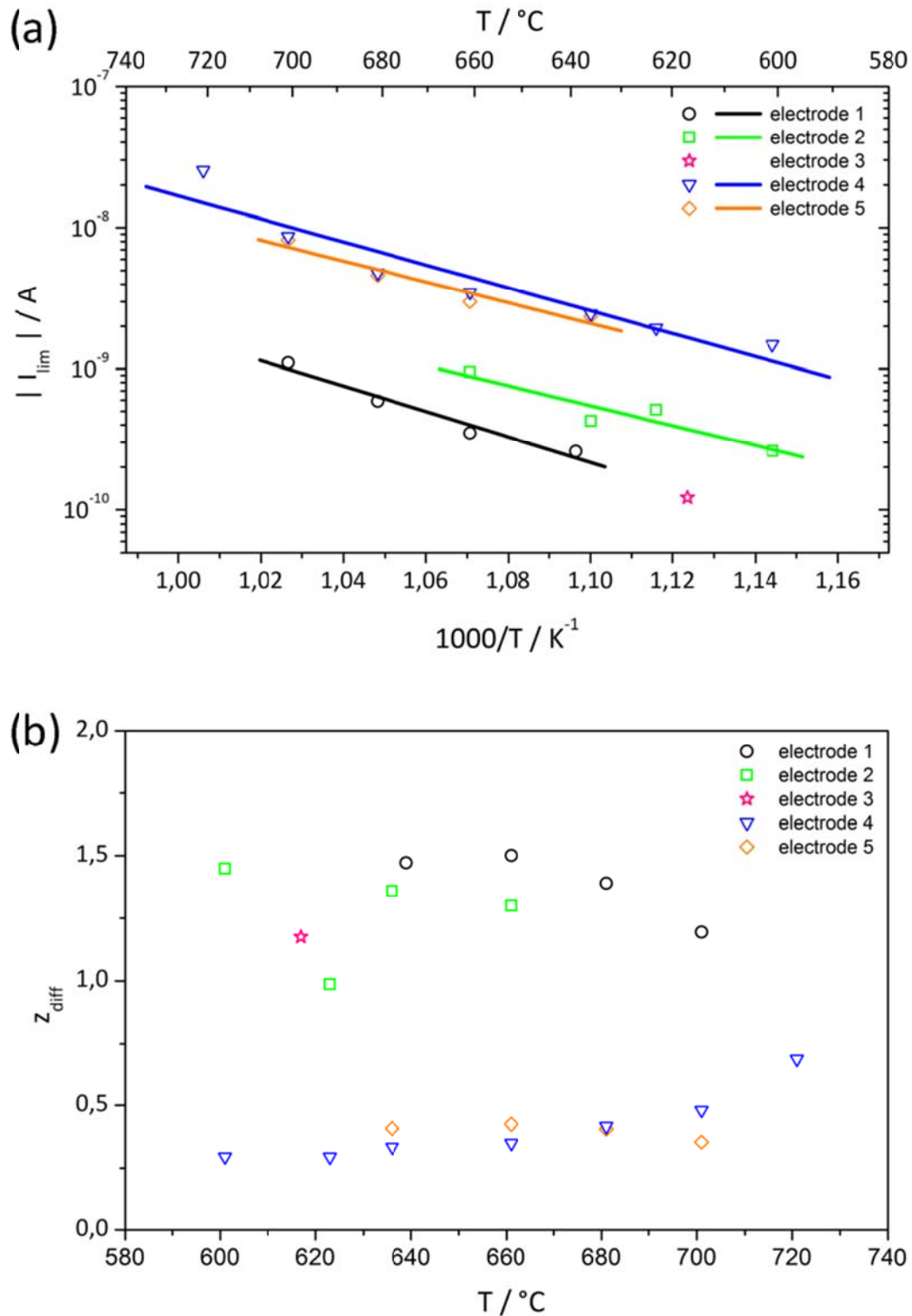


Figure 51: Fit parameters corresponding to the diffusion process (cf. Eq. 46). (a) Arrhenius plot of the limiting current I_{lim} (absolute values) including linear regression lines. Different symbols correspond to different electrodes. (b) Plot of z_{diff} values versus temperature.

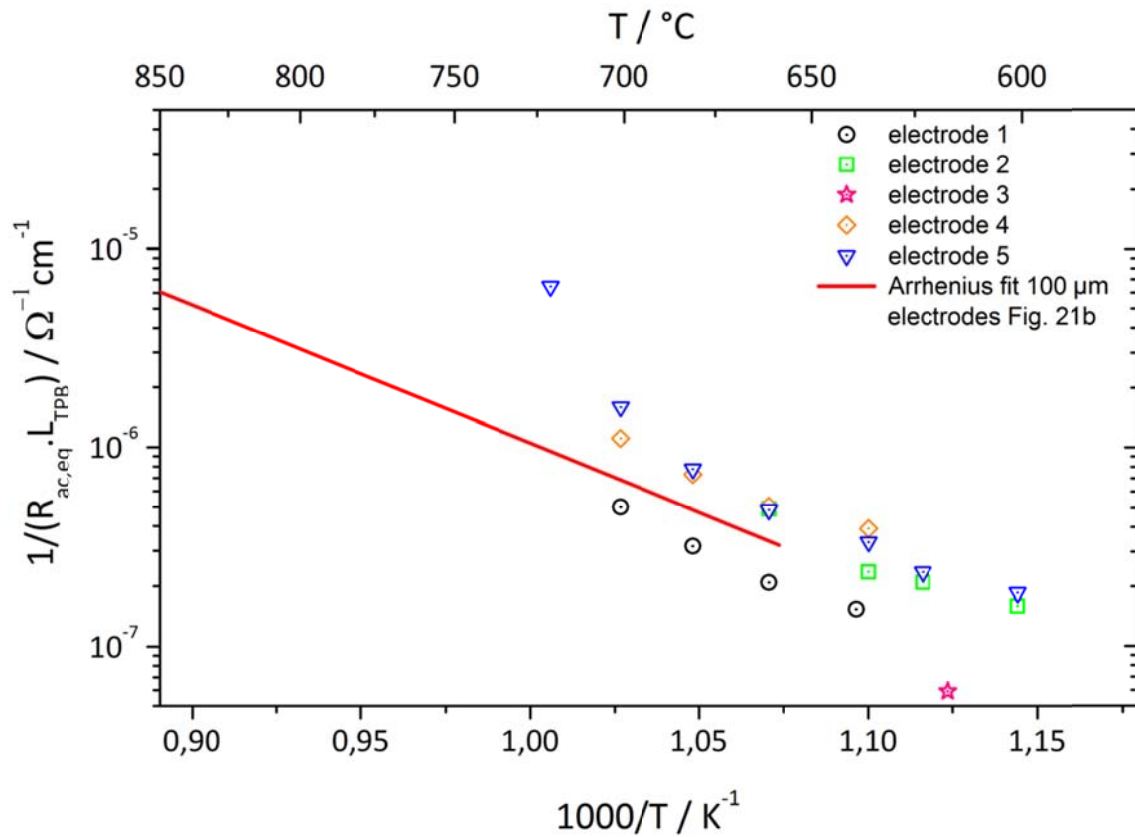


Figure 52: Comparison of TPB length related inverse polarization resistances (obtained from the slopes of the fit curves – cf. Eq. 50) with results of impedance data from Sec. 4.1.2.1 (Fig. 21); the red line shows the Arrhenius fit of impedance measurements on 100 μm electrodes.

inverse TPB length-related polarization resistances of 100 μm electrodes from Sec. 4.1.2.1 (Fig. 21b). It becomes obvious that the values obtained from the dc results by Eq. 50 scatter around the fit line from ac measurements on comparably prepared electrodes. Moreover, both data sets exhibit quite similar slopes in the Arrhenius plot and thus similar activation energies: 1.36 ± 0.11 eV versus 1.57 ± 0.17 eV. Hence, it can be concluded that the TPB-related polarization resistances (measured at comparable temperatures above 600 $^{\circ}\text{C}$) in the impedance study of Sec. 4.1 can also be attributed to a diffusion-limited process.

The second fit parameter z_{diff} also showed a broad distribution of values for different electrodes, but in contrast to I_{lim} clear trends in dependence of temperature could not be observed (Fig. 51b). Reasons for this scattering as well as for the average

value of roughly one rather than two are not clear. A factor of two would be expected for a simple diffusion of an atomic/ionic oxygen species through an impurity phase. More detailed information on the exact path (through the phase, along an interface between phase and electrode, etc.) and the diffusing species can thus not be given.

6.3 Exponential current-voltage relationship

Both fitting parameters (I_0 and b) related to the exponential part of the fit function are depicted in Fig. 53. The fitting results of I_0 are shown in an Arrhenius plot in Fig. 53a (two measurements were not considered due to problems with the fitting procedure). A noteworthy fact is that I_0 exhibits an activation energy of 3.65 ± 0.35 eV, which is uncommonly high for electrode processes on YSZ. The average value of fitting parameter b was obtained to be 1.05 ± 0.07 .

As mentioned above the shape of the current-voltage curves suggests a parallel connection of two reaction pathways, each with a rate limiting elementary process (cf. Sec. 6.1). Since the process dominating at low polarization was assigned to a diffusion process at the TPB, the process at high cathodic polarizations could still either be an elementary step of a bulk path through the Pt electrode or of a YSZ surface path. Since a possibly existing bulk path, which was discussed to be limited by diffusion of oxygen along Pt grain boundaries (cf. Sec. 4.2.5.2 and Ref. [35]), is only relevant at temperatures below 450 °C, the observed exponential I - η relationship is most likely attributed to a process on the free YSZ surface. In such a surface path via YSZ, electron conduction in YSZ from Pt to oxygen reduction sites on the free YSZ surface is required. Therefore the exponential relationship between current and voltage at high polarization could be interpreted in at least two different ways: i) Changes in electronic conductivity in YSZ with stoichiometry changes due to cathodic reduction of YSZ (stoichiometry polarization) could exhibit an exponential current-voltage relationship [124]. ii) Charge transfer limited electrode kinetics (commonly denoted Butler-Volmer kinetics) would be another possible model for the observed exponential current-voltage behavior [1] and its high activation energy. A discussion of these possible interpretations will be given in the following sections.

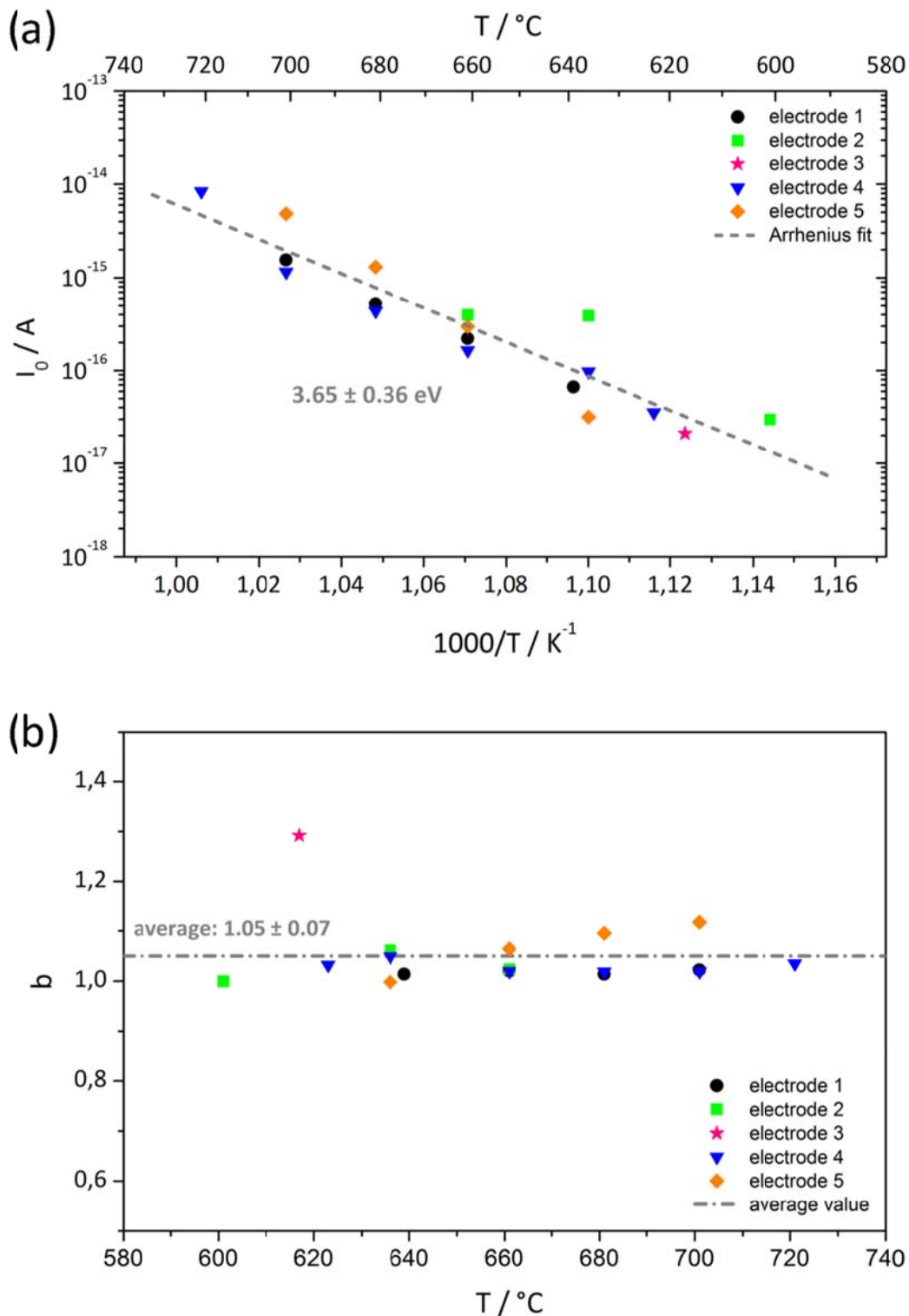


Figure 53: Fit parameters corresponding to Eq. 47 for different electrodes. (a) Arrhenius plot of fit parameter I_0 . Taking the data of all electrodes into account the grey dashed fit line is obtained; the corresponding activation energy is 3.65 ± 0.36 eV (b) Plot of b values versus temperature; the average value of all data points was 1.05 ± 0.07 (gray dash-dotted line).

6.3.1 Stoichiometry polarization

The conductivity of electrons in YSZ is proportional to their concentration (assuming that their mobility is concentration independent) [97, 119]. The stoichiometry of YSZ and thus the concentration of “free” electrons in the material can be changed by electrochemical polarization. The electronic current I_{eon} through YSZ with a cathode ideally blocking the ionic current and a reversible counter electrode (classical Wagner-Hebb polarization) is given by [124]

$$I_{\text{eon}} = -\frac{k_B T}{e_0 B} \cdot \sigma_{\text{eon,eq}} \cdot e^{-\frac{e_0 \eta}{k_B T}}. \quad (51)$$

In Eq. 51 B denotes the length of the sample in the one dimensional case of macroscopic electrodes and $\sigma_{\text{eon,eq}}$ is the electronic conductivity of YSZ at equilibrium conditions (i.e. at the reversible electrode).

A very similar situation is found here: The Pt microelectrode is highly blocking (though not entirely blocking for oxygen exchange along the TPB) while the counter electrode is almost reversible due to its large size. Accordingly, a significant stoichiometry polarization beneath the Pt electrode, which is also decaying along the free electrolyte surface, can be expected. As a consequence the related increase of the local electron concentration in YSZ can open a second pathway for oxygen reduction at the free YSZ surface. If electron conduction from Pt to the reaction sites on YSZ is rate limiting, an I - η relation similar to Wagner-Hebb-polarization would be expected, with B in Eq. 51 now reflecting the lateral path of electron transport from Pt to the reaction site rather than to the counter electrode. Hence, despite our electrode setup is not symmetric and the Pt microelectrode is not ideally blocking Eq. 51 still allows a meaningful approximation of the I - η behavior in case of stoichiometry polarization with electron transport in YSZ as the rate limiting step of oxygen reduction on the free YSZ surface. Neglecting any polarization resistance of processes in series to electron migration in YSZ it therefore follows $I_{\text{exp}} \approx I_{\text{eon}}$. In this interpretation the fitting parameter b has to be equal to one and the parameter I_0 reads (compare Eqs. 47 and 51)

$$I_0 = \frac{k_B T}{e_0 L} \cdot \sigma_{\text{eon,eq}}. \quad (52)$$

In this case the activation energy of I_0 is given by the activation energy of electron conduction in YSZ. The value of 3.65 ± 0.36 eV obtained from the Arrhenius fit in Fig. 53a is in good agreement with activation energy values for electronic conductivity in stabilized zirconia reported in literature: 3.88 eV for 8 mol% Y_2O_3 - ZrO_2 [97] and 3.7 eV for CaO - ZrO_2 [125]. Since also the fit parameter $b = 1.05 \pm 0.07$ (cf. Fig. 53b) is in accordance with this interpretation, it is considered that stoichiometry polarization and thus the electronic conductivity of YSZ is a very likely rate limiting process to describe the exponential current-voltage characteristics of our Pt electrodes at high cathodic polarization. Moreover, it was published recently that also the electrode reaction on the system noble metal (Au; Pt)|Sm-doped ceria under reducing conditions is limited by migration of electrons in the electrolyte [26].

Please note: In case of an ideally blocking electrode the relationship between current and set voltage would also be an exponential one (owing to an additional electronic path through YSZ from the blocking to the reversible electrode – cf. Eq. 51). To

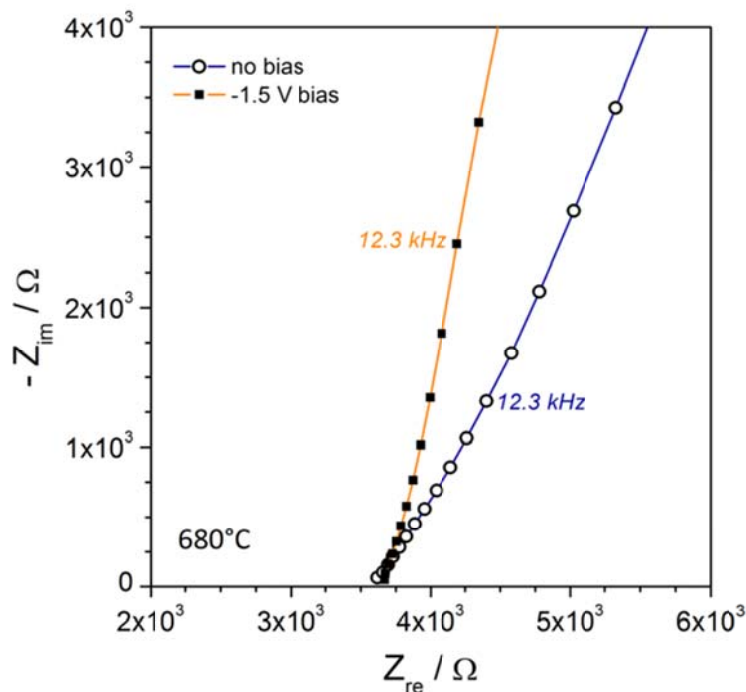


Figure 54: High frequency part of impedance spectra measured without an additional dc bias (open circles) and at -1.5 V bias (closed squares). The high frequency intercept is virtually the same indicating no noteworthy electronic current path within YSZ.

exclude this classical Wagner-Hebb-like electronic current as the source of the exponential current-voltage behavior, an impedance spectrum measured under -1.5 V bias is compared to an impedance spectrum without an additional dc voltage in Fig. 54. The high frequency axis intercepts of both spectra – corresponding to the spreading resistance of YSZ – are virtually equal and consequently an electronic current path from the microelectrode to the counter electrode significantly affecting the total conductivity can be excluded. The current in YSZ is still almost exclusively ionic. The small electronic current from Pt via YSZ to the reaction site on the YSZ surface is caused by stoichiometry polarization close to the microelectrode but then transferred into an ionic current due to the electrochemical oxygen reduction on the YSZ surface. Hence the increased total dc current has to be attributed to an increased electrochemical reaction rate rather than an additional electronic current in parallel to the ionic current in YSZ.

6.3.2 Polarization due to charge transfer and low electron concentration in YSZ

Another case potentially leading to an exponential I- η curve is a charge transfer reaction on the free YSZ surface (O^y denotes an arbitrary oxygen species with charge y).



The exchange current I_{eq} of such a reaction is given by

$$I_{eq} = e_0 \cdot k_{cath} \cdot [O^y] \cdot [e^-]_{eq} \quad (54)$$

with k_{cath} denoting the rate constant of the cathodic reaction, $[O^y]$ the concentration of the oxygen species and $[e^-]_{eq}$ the equilibrium concentration of electrons in YSZ. Since the kinetics of charge transfer reactions on the surfaces of mixed conductors are highly complex [126] a straightforward discussion of I_{eq} - η relationships can hardly be given at this point. In the classical Butler-Volmer kinetics the concentrations are assumed to be independent of η . In the present case, however, this assumption would not hold for the concentration of electrons. Moreover, the concentration of an oxygen species on the

YSZ surface would depend on the surface potential difference which is coupled to η by non-trivial relationships [126]. An estimation of the corresponding activation energy of such a scenario is difficult even though also very high values can be expected simply due to the highly temperature dependent electron concentration. Hence, also a charge transfer reaction at the YSZ surface as rate limiting step of the exponential part in the I- η curves cannot be excluded. Anyway, both scenarios (6.3.1 and 6.3.2) reflect an additional reaction path of oxygen reduction via the free YSZ surface.

6.4 Consequences of dc results for the CNLS-fitting of impedance spectra

It was already mentioned above that the I- η curve close to equilibrium should correspond to the situation observed in impedance measurements without bias voltage. As shown in Fig. 55 in agreement with all impedance measurements of this study (Secs. 4.1 and 4.2) again a large arc results in the complex impedance plane was observed and this should mainly be caused by the diffusion limited process discussed in Sec. 6.2. At high frequencies again a kind of shoulder was found and this cannot be explained by the reaction paths discussed so far for dc measurements. Its resistor is proportional to the inverse electrode area (cf. Sec. 4.1) and thus neither caused by an additional step in the diffusion limited TPB path nor due to the YSZ surface related exponential kinetics which is not only TPB-related but also negligible close to equilibrium. Hence, in the investigated temperature region between 600 and 700 °C the complete picture of electrochemical reaction paths on Pt thin film electrodes has to consider three contributions and is sketched in Fig. 56: The diffusion limited TPB path, presumably across an impurity phase (a), the YSZ surface path measurable only at high overpotentials (b) and a capacitively blocked path at the electrode|electrolyte interface visible as high frequency shoulder in the impedance spectra (c).

In the analysis of the impedance data close to equilibrium in Sec. 4.1 an equivalent circuit consisting of a R-CPE element in parallel to an additional capacitively blocked reaction path was used (cf. Fig. 19). The resistive path was interpreted as an electrochemical reaction at the TPB (charge transfer) or in terms of co-limited kinetics with a short decay length close to the TPB. One interpretation of the capacitively

blocked path was an electrochemical reaction of “chemisorbed” oxygen at the Pt|YSZ interface, which might be attributed to an interfacial nonstoichiometric impurity phase or an interfacial oxide phase of Pt. In Fig. 57a the Bode plot of the impedance spectrum in Fig. 55 (open circles) is compared to the CNLS-fit employing the circuit in Fig. 19 (filled red diamonds). The low frequency region of the spectrum (exhibiting the polarization resistance of the rate determining step) is characterized sufficiently, whereas

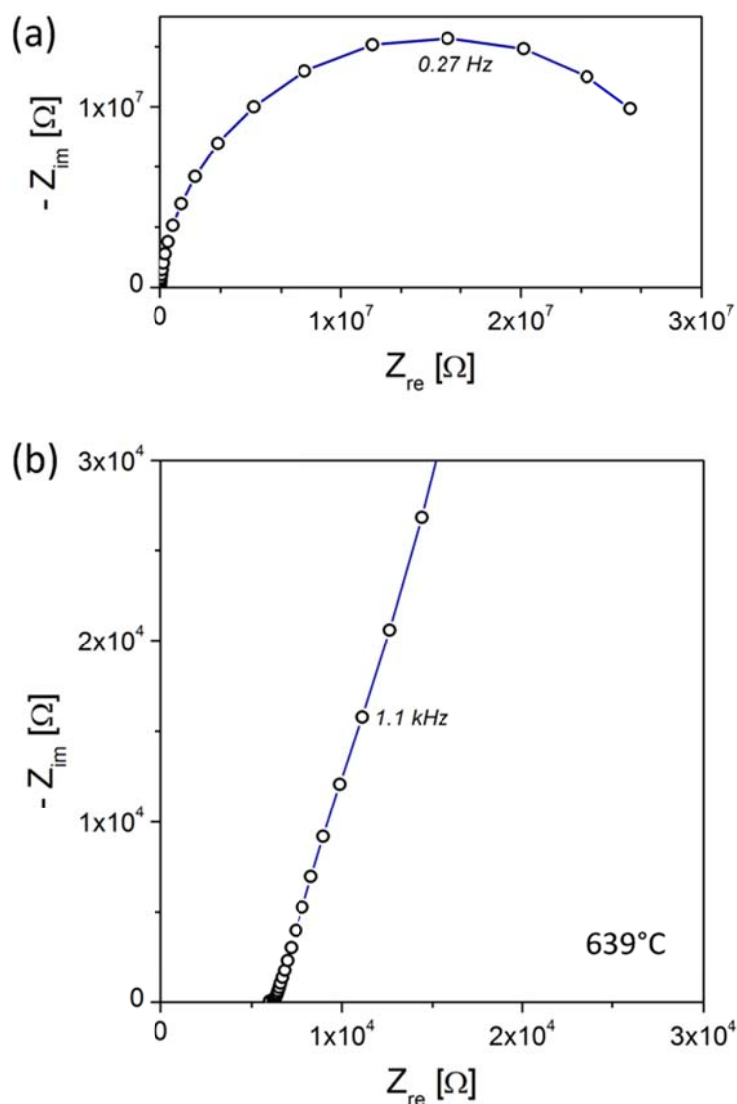


Figure 55: Impedance spectrum (Nyquist plot) of a 100 μm electrode measured at 639 °C (real temperature). (a) Low frequency part of the spectrum showing the dominating arc. (b) High frequency part exhibiting a real axis intercept and a shoulder-like feature.

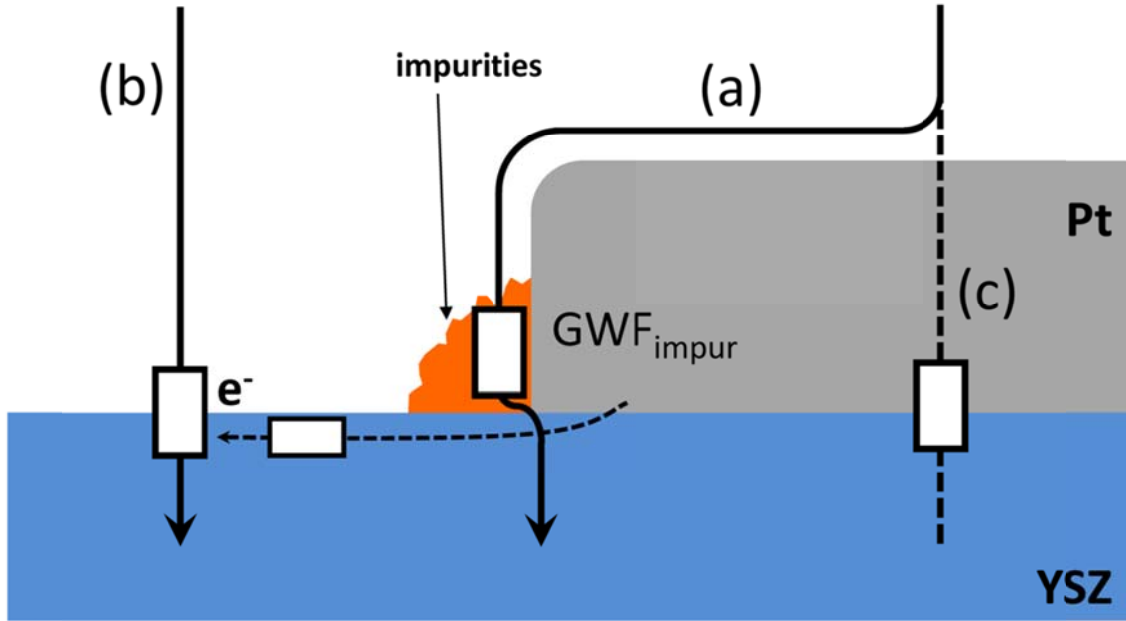


Figure 56: Sketch of the discussed parallel electrochemical pathways (capacitances are not shown): (a) Pt surface path with diffusion of oxygen through an impurity phase at the TPB being rate limiting. (b) Electrochemical oxygen reduction process on the free YSZ surface with electron supply via the electrolyte. (c) Capacitively blocked path via an interfacial “phase”.

some deviation between fit and measured data can be observed in the medium and high frequency range. This deviation is not surprising since the corresponding equivalent circuit does not consider the circuit elements usually representing a rate limiting diffusion process namely a generalized finite Warburg (GFW) element [127]. With a short circuited terminus the impedance Z_{GFW} of the GFW element is defined by

$$Z_{GFW} = \frac{R_{GFW} \cdot \tanh(i \cdot \omega \cdot t_{GFW})}{(i \cdot \omega \cdot t_{GFW})^p} \quad (55)$$

where i and ω are the imaginary unit and the angular frequency, respectively. R_{GFW} , t_{GFW} and p are fitting parameters. In the diffusion interpretation (i.e. with $p = 0.5$) R_{GFW} is the dc diffusion resistance and t_{GFW} is a characteristic time given by

$$t_{GFW} = \frac{L^2}{D} \quad (56)$$

with L denoting the diffusion length and D the diffusion coefficient. The accuracy of a fit using a GFW element instead of R_1 , however, only slightly increased. When also replacing the second resistor R_2 by a GFW element, the fit quality became considerably higher. The results of the CNLS-fit – employing the equivalent circuit from Fig. 19 and the circuit with GFW elements instead of resistors – are summarized in Tab. 10. Further, the fit result using GFW elements instead of resistors (closed green squares) is compared with the measured data in Fig. 57b – the circuit is shown as insert. When comparing Figs. 57a and b it becomes obvious that especially the high frequency part of the spectrum is much better described by the circuit with GFW elements instead of resistors. Since the p values of both Warburg elements are not far from 0.5 (0.65 for GFW_1 and 0.44 for GFW_2) both can be interpreted as non-ideal diffusion processes. The dc resistances of GFW_1 and GFW_2 in case of a $100\ \mu\text{m}$ electrode at $639\ \text{°C}$ were obtained to be $31.1 \cdot 10^6\ \Omega$ and $57.5 \cdot 10^3\ \Omega$, respectively. Despite the only moderate errors for all fit parameters in Tab. 10 it remains an open question whether this modification of the equivalent circuit is an over-parameterization or physically meaningful. Nevertheless, a few thoughts regarding the mechanistic relevance of the two Warburg elements are given in the following.

The meaningfulness of the element GFW_1 was already discussed above and is in accordance with the dc results. A rate-limiting diffusion process on the system Pt|YSZ was also discussed in literature [4, 47]. In Ref. [47] the authors successfully applied an equivalent circuit commonly called Randles-circuit to fit the impedance spectra of porous electrodes. This circuit consists of a diffusion impedance in series to a resistor (interpreted as charge transfer resistance) and an interfacial capacitor in parallel to both processes. The semicircle-like appearance of the electrode impedance rather than a 45° line in the high frequency part of the Nyquist plot despite assuming a rate limiting diffusion was attributed by the authors to the relatively high value of the interfacial capacitor. Indeed a subtraction of these capacitive contributions (as well as the charge transfer resistance) from the measured data obtained the 45° high frequency feature, which is characteristic for diffusion processes. As a consequence of this result the rate determining step of oxygen reduction at Pt electrodes on YSZ was often interpreted in terms of a rate limiting surface diffusion of an adsorbed oxygen species on Pt or a co-limitation of surface diffusion and adsorption [47, 58, 70]. However, this can hardly be the case for the Pt model electrodes used in the present thesis when looking at the

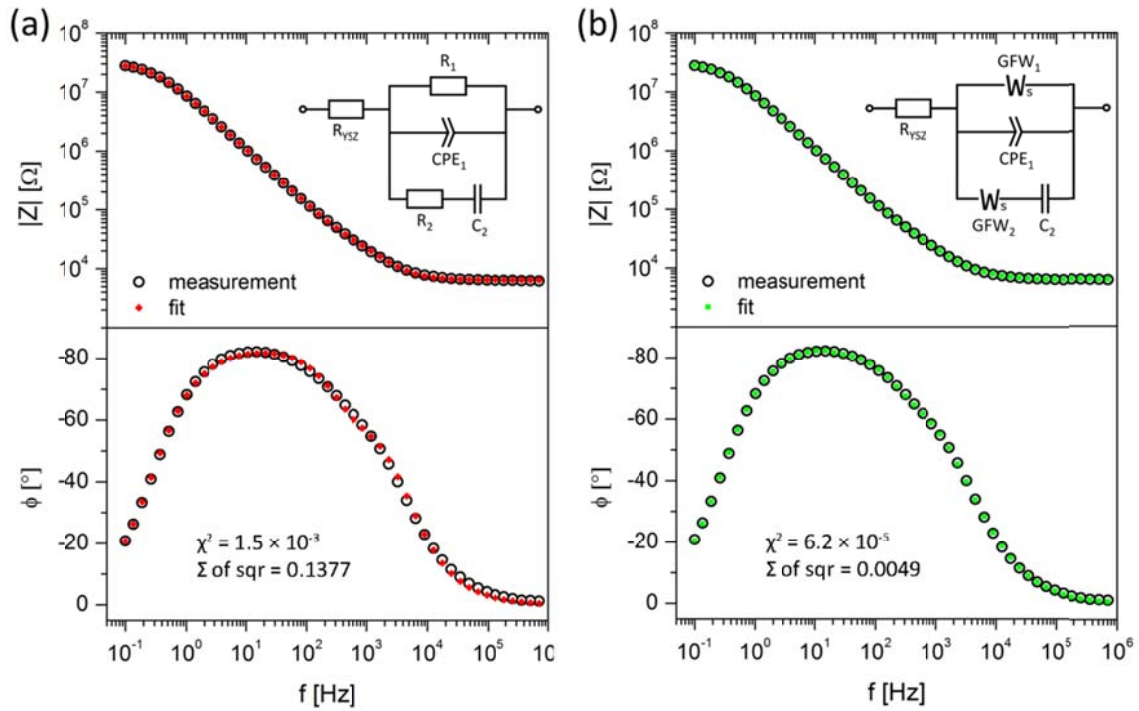
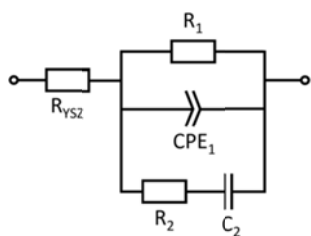
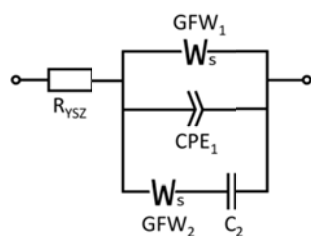


Figure 57: Bode plots of the measured impedance spectra in Fig. 55 (open circles) compared to the fits using two different equivalent circuits (depicted as inserts): (a) Equivalent circuit from Fig. 19. (b) Improved equivalent circuit considering diffusion limitation as discussed throughout the text.

results in Sec. 4.2.5. The suggested rate limiting diffusion step through an impurity “rim” at the TPB, however, would also be in accordance with the results of the earlier studies. Hence, the path sketched in Fig. 56a indeed seems to be the most realistic one to explain both the previous results in literature and the diffusion limited elementary process close to the TPB of the Pt model electrodes in the present thesis.

The constant phase element (CPE_1) in parallel to the diffusion limited TPB-process can be interpreted as a kind of double layer capacitor [31]. Because of the elements in parallel to CPE_1 a calculation of a capacitance from the fit parameters and Eq. 51 is not straightforward. A fit with an ideal capacitor (for the cost of less fit quality; graph not shown) yielded a value of $51 \mu\text{F}/\text{cm}^2$ which is close to that obtained for the simplified circuit applied in Sec. 4.1.

Table 10: Comparison of CNLS-fit results obtained from fits of the spectrum in Fig. 55 with two different equivalent circuits. The Bode plots of both fits are shown in Fig. 57.

					
fit-parameter	value	fit-error [%]	fit-parameter	value	fit-error [%]
χ^2	$1.53 \cdot 10^{-3}$	—	χ^2	$6.21 \cdot 10^{-5}$	—
Σ of sqr	0.1376	—	Σ of sqr	0.0049	—
R_{YSZ} [Ω]	6409	0.46	R_{YSZ} [Ω]	6288	0.16
R_1 [Ω]	$3.13 \cdot 10^7$	0.99	GFW_{1-R} [Ω]	$3.11 \cdot 10^7$	0.26
			GFW_{1-t}	$3.72 \cdot 10^{-2}$	6.27
			GFW_{1-p}	0.6451	2.78
CPE_{1-Q}	$1.58 \cdot 10^{-8}$	1.51	CPE_{1-Q}	$1.38 \cdot 10^{-8}$	1.00
CPE_{1-n}	0.9098	0.18	CPE_{1-n}	0.8950	0.15
R_2 [Ω]	86216	5.20	GFW_{2-R} [Ω]	57481	4.41
			GFW_{2-t}	$6.02 \cdot 10^{-4}$	5.72
			GFW_{2-p}	0.4391	2.11
C_2 [F]	$3.88 \cdot 10^{-9}$	3.08	C_2 [F]	$5.47 \cdot 10^{-9}$	1.84

Finally, a possible explanation for a diffusive element in the capacitively blocked path in parallel to the TPB-process should be briefly mentioned: Existence of PtO_x as a potential source for an electrochemical process at the Pt|YSZ interface was already mentioned in several studies dealing with Pt electrodes on YSZ [12, 42, 67, 95] and in Sec. 4.1. In Ref. [12] a diffusion controlled process was suggested for anodic growth of a PtO_x “phase” at the interface. Assuming the existence of such a PtO_x “phase” also around equilibrium conditions, a capacitively blocked GFW element instead of a resistor would indeed be an appropriate model to describe diffusion limited oxygen stoichiometry variations in this phase. In this case the blocking capacitor is a chemical capacitance and its value of $70 \mu\text{F}/\text{cm}^2$ seems to be reasonable when assuming an interfacial PtO_x “phase” with a significant stoichiometry range. However, it should be not-

ed, that from the data available so far the existence of PtO_x at the interface cannot be proven unambiguously. Moreover, it should be mentioned that the capacitively blocked GFW element could also only exhibit an appropriate simplification of a much more complex circuit [128]. Hence, the physical meaning of the respective fit parameters is still open for discussion. Also the geometry dependence of the individual CNLS-fit parameters for differently sized Pt electrodes has not been analyzed yet (cf. Sec. 4).

6.5 Consequences of dc results on the interpretation of ^{18}O tracer experiments

In Sec. 5.2 it was shown by means of ^{18}O tracer experiments that the electrochemically active region of oxygen incorporation into YSZ at relatively high cathodic overpotentials (~ -2 V) and low temperatures (~ 300 °C) consists of two contributions: a frame shaped zone close to the TPB and a homogeneous zone along the entire Pt|YSZ interface (cf. Secs. 5.2.1 and 5.2.5). Owing to the high cathodic polarization values (which were necessary for a sufficiently high incorporation current) it could not be concluded from these tracer experiments, if the TPB-near process (leading to the frame shaped incorporation zone) was of the same nature as that close to equilibrium conditions. In the present dc experiments two different surface paths were identified. An extrapolation of the currents expected from Eqs. 46 and 47 to low temperatures could thus possibly show which path was responsible for the frame shaped incorporation zone in the ^{18}O distribution images. In Fig. 58a an Arrhenius plot of both polarization resistances identified in dc measurements (i.e. the inverse derivative of Eqs. 46 and 47 at $\eta = 0$ V) is shown, considering a temperature range of 275 – 900 °C. This graph clearly indicates that close to equilibrium conditions the path with a rate limiting diffusion process close to the TPB is the dominating surface path in the entire plotted temperature range. In Figs. 58b-f Arrhenius plots of the dc currents calculated by Eqs. 46 and 47 are shown for different polarizations. Up to cathodic polarizations of -1.0 V the diffusion limited Pt surface path is still dominating (cf. Figs. 58b-d). At higher cathodic polarization (ca. -1.5 V; Fig. 58e), however, the YSZ surface path starts to exceed the Pt surface path. A further increase in polarization to -2.0 V leads to a situation where the

YSZ surface path is carrying an orders of magnitude higher current over the entire temperature range (Fig. 58f).

From these results it can be concluded that the TPB process visualized in the ^{18}O tracer experiments in Sec. 5.2.1 was almost exclusively related to the YSZ surface path. Owing to the additional Pt bulk path, which is connected in parallel to both surface paths (cf. Sec. 4.2.5), also a significant homogeneous tracer incorporation in YSZ underneath the entire dense Pt electrode was found in Sec. 5.2.5. The currents via the TPB and via the Pt bulk path were calculated by Eq. 45 and a ratio of $I_{\text{dc,TPB}} : I_{\text{dc,Pt|YSZ}} = 1 : 4$ resulted for the electrode with -1.99 V polarization (cf. Tab. 9). In Fig. 58f the current contribution of the bulk path (corrected for circular $100\ \mu\text{m}$ electrodes) is shown by the blue cross at $308\ ^\circ\text{C}$ and a ratio $I_{\text{dc,TPB}} : I_{\text{dc,Pt|YSZ}} \approx 1 : 1$ is yielded from Fig. 58f. This in acceptable agreement with the current ratio obtained in Sec. 5.2.5 and further supports the result that the electrochemically active zone visualized in the ^{18}O experiments was related to the YSZ surface path. (It should be noted that only a slight change in the activation energy of the process on the YSZ surface – $3.72\ \text{eV}$ instead of $3.65\ \text{eV}$ – yields almost exactly the current ratio of $1 : 4$ obtained from Eq. 45 for electrode 1 in Sec. 5.2.5. This somewhat higher activation energy value, however, is still within the statistical scatter of the value obtained for I_0 in Fig. 53: $3.65 \pm 0.36\ \text{eV}$)

This result seems to contradict the result in Sec. 5.2 that the oxygen incorporation zone close to the TPB is located underneath the Pt electrode. However, a PtO_x “phase” could lead to a situation with a diffusion limited path in parallel to a path with electron supply via YSZ and oxygen incorporation beneath Pt. Further data are needed to finally clarify this point.

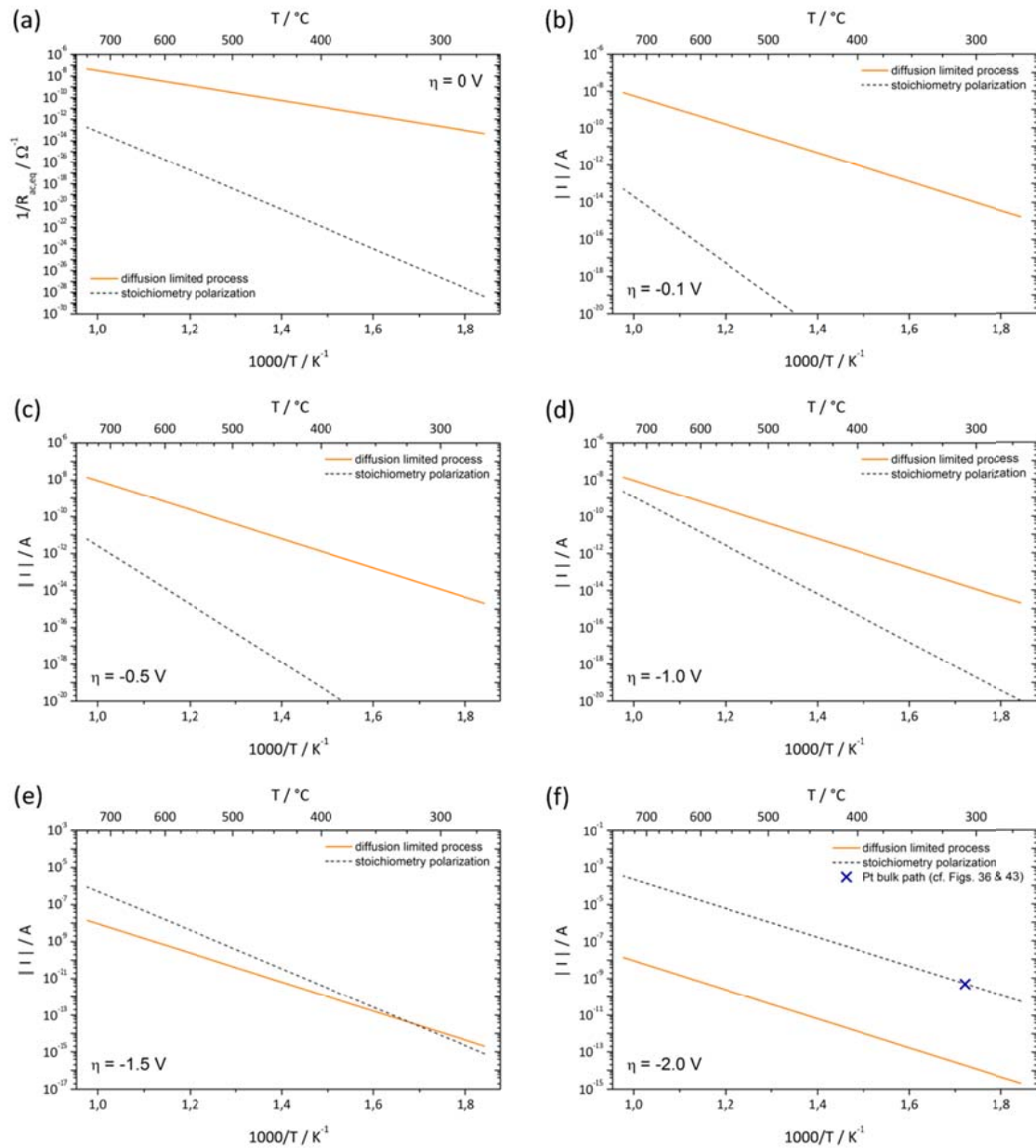


Figure 58: Arrhenius plots for the two processes identified in dc experiments and extrapolated to lower temperatures. The orange continuous line reflects the diffusion limited Pt surface path, whereas the gray dashed line represents the path with an exponential I - η relation. All values correspond to circular electrodes with $100\ \mu\text{m}$ in diameter. (a) Inverse polarization resistance at equilibrium conditions. (b) Current at $-0.1\ \text{V}$ overpotential. (c) Current at $-0.5\ \text{V}$ overpotential. (d) Current at $-1.0\ \text{V}$ overpotential. (e) Current at $-1.5\ \text{V}$ overpotential. (f) Current at $-2.0\ \text{V}$ overpotential. The blue cross indicates the current measured during ^{18}O incorporation at the “lowest” polarized electrode (electrode no. 1, $\eta = -1.99\ \text{V}$) in Sec. 5.2.1.

7 Complete Picture of Reaction Paths

Altogether from the results of this thesis it is possible to identify and separate five different electrochemical pathways of the system Pt|YSZ, three faradaic ones and two being capacitively blocked. A sketch is given in Fig. 59.

- i) Path (a) is usually referred to as Pt surface path. This path was extensively studied in the past and a number of different rate determining steps have been suggested. In the present thesis oxygen diffusion through an impurity phase at the TPB was concluded to be the kinetically slowest step of the Pt surface path. At moderate polarization (of few hundred millivolts) and at temperatures above 600°C it was found to be the electrochemically fastest among the faradaic pathways.
- ii) The path (b) represents a faradaic bulk path through platinum. The rate limiting elementary step of this pathway is most probably diffusion of oxygen along Pt grain boundaries. Around equilibrium conditions and below 400 °C this path was found to exhibit the lowest resistance among the faradaic paths and an area-related polarization resistance resulted. The emergence of this bulk path might be attributed to the extreme aspect ratio of the thin film electrodes used in this study (300 - 500 nm thickness, 50 - 200 µm diameter) and the small grain size of low temperature deposited Pt films.
- iii) A third faradaic path – the YSZ surface path sketched in (c) – was shown to become relevant at very high cathodic polarization (e.g. 300 °C: -1.5 V; 900 °C: -1 V). At these conditions path (c) carries the highest dc current and the rate limiting step was shown to lead to an exponential current-overpotential relationship and a very high activation energy. Most likely this is due to a stoichiometry polarization with oxygen reduction on the free YSZ surface and electron supply via the electrolyte being rate limiting.
- iv) A capacitively blocked reaction pathway (d) in parallel to the double layer capacitor was interpreted in terms of the electrochemical reaction of an oxygen containing “phase” at the Pt|YSZ interface. This “phase” was assumed to be related

to cavities filled with O_2 , PtO_x or a non-stoichiometric impurity phase. The blocking capacitor can be interpreted as the chemical capacitance of the interfacial “phase”.

- v) Finally the fifth path is purely capacitive via the “double layer capacitor” at the interface; indicated in Fig. 59 as path (e). At 700 °C the interfacial capacitance was in the range of 50 – 70 $\mu F/cm^2$.

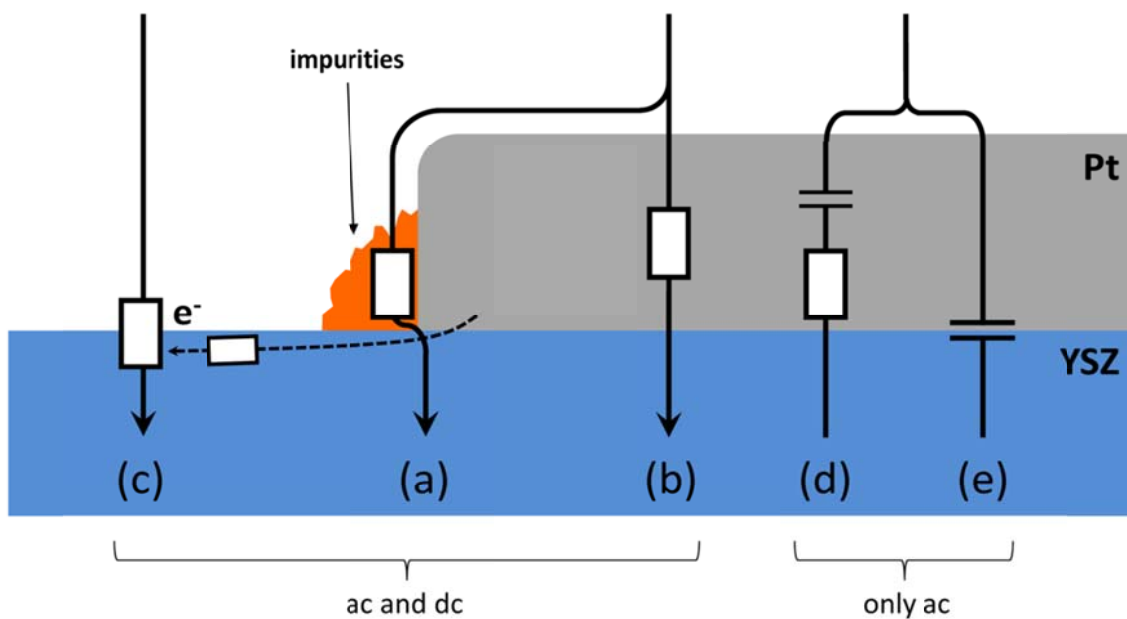


Figure 59: Different electrical pathways available for Pt electrodes on YSZ. Reaction pathways offering the possibility of a faradaic reaction are indicated by an arrowhead. (a) Pt surface path with diffusion through an impurity phase at the TPB being rate limiting. (b) Bulk path through the Pt electrode; most probably via diffusion of oxygen along Pt grain boundaries. (c) Electrolyte surface path with reduction of O_2 on the free YSZ surface which is most likely rate limited by electron supply via the electrolyte. (d) Reaction path via an oxygen containing “phase” at the Pt|YSZ interface which is capacitively blocked by the finite amount of oxygen stored in it. (e) Capacitive path via the interfacial double layer capacitor.

8 Summary of Scientific Achievements

8.1 Sample preparation and measurement techniques

Dense Pt microelectrodes were successfully prepared by means of two different preparation procedures: The first method was sputter-deposition of a platinum thin film onto a heated (~ 700 °C) YSZ substrate followed by standard photolithography, etching in aqua regia, and a subsequent annealing step (48 h at $700 - 750$ °C) to obtain sufficiently stable thin film model electrodes [21]. The second method was low temperature Pt sputter-deposition (without additional heating of the sample) followed by lift-off photolithography for micro-patterning and short time annealing (2 h) at 750 °C. By using these methods it was possible to prepare electrodes which exhibited a sufficiently stable geometry (i.e. shape and TPB length) up to temperatures of 900 °C (high temperature prepared) or 750 °C (low temperature prepared).

Owing to the special geometry of microelectrode samples (electrodes on top, heating from the bottom) and due to the contact by the tip, a temperature gradient across the YSZ electrolyte is generated. This temperature gradient had two distinct effects in electrochemical measurements on microelectrodes and on the analysis of the recorded data. Firstly, the temperature of the measured electrode differed from the set temperature and the effective electrode temperatures were different for differently sized microelectrodes. To account for these thermal deviations a procedure was developed to calculate the true temperature from the spreading resistance of ion conduction in YSZ and the known relation of YSZ ionic conductivity and temperature. The second effect of the temperature gradient was the generation of a thermovoltage, which can lead to a polarization of the electrode resulting in a non-equilibrium situation even without an external dc bias. To overcome this effect a quasi four-wire method with an additional blocking capacitor was suggested and implemented into impedance measurements.

Moreover, in the framework of this thesis the experimental technique of ^{18}O tracer incorporation as a tool for the visualization of the electrochemically active zone of

oxygen exchange was adapted to Pt microelectrodes. In contrast to previous experiments (where the entire sample was surrounded by the tracer gas), the technique employed in the present thesis is based on a local supply of the $^{18}\text{O}_2$ gas only to the few microelectrodes of interest. This modification offers several advantages: First, it allows investigating both a polarized microelectrode and a reference microelectrode (without an electrochemical treatment) in one and the same ToF-SIMS measurement. Hence, SIMS-artifacts resulting from changes between two different measurements can be excluded. Second, it is possible to conduct several experiments on one sample, which minimizes deviations between different tracer experiments on different electrodes due to slightly different preparation conditions. Finally, this technique is also attractive from an economic point of view since the amount of consumed tracer gas is much lower than in case of the macroscopic technique. The drawback of this method is, that the tracer concentration in the atmosphere is unknown and a quantification of oxygen exchange rates from the surface concentrations of the tracer is thus not possible.

8.2 Electrochemical impedance measurements

In impedance measurements at temperatures between 700 and 900 °C on high temperature deposited electrodes four fundamental electrode processes – two resistive and two capacitive ones – were identified. The resistance of the rate determining step was found to be TPB length dependent with an electrode “conductivity” value of $6.6 \pm 0.9 \cdot 10^{-7} \Omega^{-1}\text{cm}^{-1}$ at 700 °C and an activation energy of 1.36 ± 0.11 eV. Compared to earlier studies in literature the relation between TPB length and polarization resistance was less ambiguous. This result further supports the already well accepted model that – at least in the investigated temperature range – the oxygen exchange reaction at Pt electrodes on YSZ proceeds via the surface path with a rate determining step close to the TPB. Hence, oxygen adsorption/dissociation on the entire Pt microelectrode surface can be excluded as the rate limiting step of the O_2 reduction reaction between 700 and 900 °C. One capacitive process was identified as the interfacial “double layer” capacitance with a value of 50 –70 $\mu\text{F}/\text{cm}^2$ at 700 °C. In parallel to this capacitance and to the TPB-related faradaic path an additional current path with resistive and capacitive contributions leads to a high frequency shoulder in the impedance spectrum. Both, resistance and capacitance scale with the electrode area. This feature is suggested to be

caused by a finite oxygen reservoir between platinum and YSZ. Provided that such a reservoir can be modified via an electrochemical process it represents a chemical capacitor and the related interfacial oxygen could either be stored in oxygen filled cavities or as “chemisorbed” oxygen at the Pt|YSZ interface (e.g. PtO_x).

The oxygen exchange kinetics of low temperature sputter-deposited platinum electrodes on YSZ could be successfully investigated by means of impedance spectroscopy at temperatures between 300 and 700 °C. By varying the size of geometrically well-defined electrodes again the geometry dependence of the polarization resistance was analyzed. In the higher temperature range (550 – 700 °C) a TPB length dependent rate limiting step with an activation energy of about 1.6 eV was successfully observed. This is in good agreement with the results obtained on the high temperature deposited electrodes mentioned above as well as with previous results from literature [22, 41, 42, 46, 50, 51]. The electrode “conductivity” in this TPB-related regime was about one order of magnitude higher than in case of the high temperature deposited electrodes. This was discussed to be probably related to the different thermal history of the electrodes. Surprisingly at lower temperatures (300 – 400 °C), another reaction regime was found exhibiting an area-related rate limiting step with very low activation energy of about 0.2 eV. From the shape of the entire Arrhenius curve it could be concluded that close to equilibrium conditions two parallel reaction paths have to be involved on these electrodes. A more detailed discussion of kinetic situations yielded two possible combinations of TPB- and area-related elementary steps explaining the experimentally obtained Arrhenius plot and geometry dependence: i) Oxygen diffusion through the Pt thin film – most likely via Pt grain boundaries – as area-related process in parallel to oxygen diffusion through an impurity phase at the TPB. ii) Oxygen diffusion through the Pt thin film in parallel to co-limitation of oxygen diffusion and charge transfer along the Pt|YSZ interface with a short decay length being responsible for the TPB-related polarization resistance.

8.3 Tracer incorporation experiments

By means of ¹⁸O tracer incorporation experiments on high temperature deposited Pt thin film microelectrodes followed by ToF-SIMS analysis it was possible to not only visualize but for the first time also quantify the zone where oxygen incorporation into

YSZ is taking place. The position and shape of this electrochemically active region strongly depended on the polarization of the respective electrode. In case of the “lowest” polarization used in this study oxygen incorporation exclusively took place beneath the platinum electrode in a narrow zone close to the TPB. With increasing polarization, the active zone extended along the free YSZ surface as well. For very high polarization a distinct change in the shape of the oxygen incorporation zone was observed, which could be explained by high electron concentration in the electrolyte leading to a change of YSZ properties from a pure electrolyte to a mixed-conductor [25, 26, 97] thus acting itself as a “cathode”.

The width of the incorporation zone was determined from lateral ^{18}O concentration profiles. Neglecting the highest polarization, the estimated TPB widths were all between 1.0 and 1.3 μm . These values do not contain any contributions of ^{18}O mass transport in YSZ since it was possible to subtract broadening effects caused by ^{18}O bulk diffusion with a diffusion length of about 0.5 μm . Such small diffusion lengths, however, required rather low temperatures (300 – 330 °C) and thus quite high polarization voltages had to be applied to incorporate measurable amounts of ^{18}O . Moreover, an anomalous high concentration of the tracer along the entire Pt|YSZ interface was discussed in terms of an electrochemical path of oxygen through the Pt bulk competing with the surface path via the TPB. This is in agreement with results of the impedance measurements at comparable temperature. Hence, oxygen transport via a bulk path through platinum grain boundaries was clearly proven to substantially contribute to the oxygen reduction current of polycrystalline Pt thin film electrodes at certain temperatures and voltages.

8.4 Current-overpotential characteristics

In a dc study on Pt model electrodes it was finally demonstrated that at low cathodic polarization a slow mass transport is the rate limiting elementary step. At sufficiently high cathodic polarization a process in parallel to the first one was observed, which showed an exponential dependence of the current on the overpotential. Such a situation is quite uncommon and has not been reported so far for the system Pt|YSZ.

The limiting mass transport at lower cathodic polarization was discussed to be caused by oxygen diffusion probably through or along an additional (impurity) phase

at the TPB of the Pt electrodes. Both, the resulting differential resistance around equilibrium and the activation energy (1.57 ± 0.17 eV) of the diffusion limiting current were in reasonable agreement with results of previous studies on Pt|YSZ [22, 41, 42, 46, 50, 51]. As a consequence an equivalent circuit for the CNLS-fit of impedance data, taking diffusion limited kinetics at the TPB into account, was suggested.

The exponential part of the I - η curve could be related to an oxygen reduction process on the free YSZ surface and was interpreted in terms of stoichiometry polarization of YSZ. This conclusion is also in accordance with the similar activation energies of the electrochemical process (3.65 ± 0.36 eV) and the electronic conductivity in YSZ. Moreover, from the extrapolation of dc results to lower temperatures it was possible to relate the TPB process observed in ^{18}O incorporation experiments to the YSZ surface path with oxygen reduction on the free electrolyte surface. This completed the picture of three different faradaic reaction paths on the Pt(O₂)|YSZ system assumed in this thesis: Depending on temperature, electrode preparation or sample history, and overpotential these paths may or may not contribute to the data measured in impedance and dc studies. Accordingly, oxygen exchange kinetics on Pt|YSZ is definitely more complex than often assumed in literature.

9 List of Symbols

A	area of electrochemically active YSZ surface	$d_{ME,set}$	nominal diameter of circular microelectrodes
A_{ME}	surface area of a microelectrode	E_a	activation energy
B	sample length (Wagner-Hebb polarization)	E_{diff}	activation energy of a diffusion process
b	fitting parameter of I_{exp}	E_s	activation energy of the sticking coefficient
b_{eff}	diffusion corrected total FWHM	e_0	elementary charge
$b_{freeYSZ}$	FWHM of lateral ^{18}O profiles on the free YSZ surface	f	frequency
b_{tot}	total FWHM of lateral ^{18}O profiles	f^*	characteristic frequency
b_{TPB}	TPB width	f_c	correlation factor
C	capacitance	H	width of an electrode stripe (co-limited kinetics)
C_{no_dc}	variable capacitor in pseudo 4-point impedance measurements	h	Pt film thickness
C_{int}	interfacial capacitance	I_0	fitting parameter of I_{exp}
$c(^{18}O)$	tracer concentration	I_{dc}	total dc current
$c_{O(gb)}$	equilibrium concentration of the diffusing oxygen species in the Pt grain boundary next to the surface	I_{diff}	diffusion current
D	diffusion coefficient	I_{eff}	resulting current in case of rate limiting adsorption
D'	pre-exponential factor of D	I_{eq}	exchange current of a charge transfer reaction
D^*	tracer diffusion coefficient	I_{exp}	dc current exponentially depending on η
d_{ME}	diameter of circular microelectrodes	I_{lim}	limiting current of diffusion limited kinetics
$d_{ME,meas}$	true (measured) diameter of circular microelectrodes	i	imaginary unit

i_{dc}	electric current density	Q	charge
int	intensity of the signal measured by SIMS	R	resistance / polarization resistance
K	equilibrium constant (mass action constant)	$R_{ad,eq}$	polarization resistance due to adsorption
K'	pre-exponential factor of K	R_{co}	polarization resistance of co-limited electrode kinetics
K''	modified pre-exponential factor of K ($K'' = K' \cdot e^{\frac{\Delta F S}{k_B}}$)	R_{diff}	polarization resistance of a diffusion limited electrode reaction
k_{-a}	rate constant of reaction from the atomically adsorbed state into the molecularly adsorbed state	R_{GFW}	fit parameter of a GFW element (diffusion interpretation: dc diffusion resistance)
k_B	Boltzmann constant	R_{ode}	polarization resistance of the electrode reaction
k_{cath}	rate constant of cathodic reaction	R_{rds}	polarization resistance of the rate determining step
L	diffusion length (GFW)	R_{samp}	dc resistance of the sample
L_{diff}	tracer diffusion length	R_{YSZ}	spreading resistance of ion conduction in YSZ
L_{TPB}	TPB length	$R_{YSZ,bias}$	YSZ spreading resistance under a dc bias voltage
M	mass of an oxygen molecule	r_a	rate of dissociation of molecularly adsorbed oxygen into atomic oxygen per unit area
N	number of oxygen molecules within the volume V	$r_{a,eq}$	equilibrium adsorption rate of dissociatively bound atomic oxygen per unit area
N_{O_2}	number of oxygen molecules in pores at the Pt YSZ interface	r_{-a}	rate of reaction from the atomically adsorbed state per unit area
n	fitting parameter of a CPE element (exponent)	r_{eff}	effective (net) reaction rate of the rate limiting dissociation step
n_{ion}	number of oxygen ions in YSZ per unit of volume ($5.7 \cdot 10^{22} \text{ cm}^{-3}$ in case of 9.5 mol% YSZ)	r_{ME}	radius of circular microelectrodes
P_{tot}	impinging rate per unit area at which the adsorptive (O_2) strikes the surface	S	sticking coefficient
p_{O_2}	partial pressure of oxygen	T	temperature
Q_{CPE}	fitting parameter of a CPE element		

t	time	$ Z_{KK} $	magnitude of the KK-transform.
t_{GFW}	fit parameter of a GFW element	z	number of transferred charges
U_{set}	dc set voltage (dc bias)	Z_{diff}	number of charges transferred by diffusion
U_{therm}	thermovoltage	$\Delta_{re,i}$	relative difference between measured impedance and KK transform of the real part
V	gas volume	$\Delta_r g$	Gibb's free reaction enthalpy
V_{pore}	volume of pores at the Pt YSZ interface	$\Delta_r h$	reaction enthalpy
w	weighting function	$\Delta_r s$	reaction entropy
X_{perp}	constant quantifying the kinetics of the process perpendicular to a diffusion process (co-limited kinetics)	η	electrode overpotential/polarization/ overpotential
Y	inverse resistance	Θ	coverage of atomically adsorbed oxygen
Y^0	pre-exponential factor of Y	Θ_{eq}	equilibrium coverage of atomically adsorbed oxygen
Z	complex impedance	$\sigma_{eon,eq}$	electronic conductivity of YSZ at equilibrium conditions
Z_{CPE}	complex impedance of a constant phase element	σ_{ion}	ionic conductivity
Z_{GFW}	impedance of a generalized finite Warburg element	σ_0	pre-exponential factor of σ_{ion}
Z_{im}	imaginary part of the impedance	σ_{lat}	lateral "conductivity" (co-limited kinetics)
$Z_{im,i}$	imaginary part of the measured impedance	φ	Galvani potential difference across the Pt YSZ interface
$Z_{im, KK}$	imaginary part of the KK-transform	ω	angular frequency
Z_{re}	real part of the impedance	ω^*	characteristic angular frequency
$Z_{re,i}$	real part of the measured impedance		
$Z_{re, KK}$	real part of the KK-transform		

10 List of Figures

- 1 Three possible reaction pathways of oxygen exchange on solid oxide ion conductors. (a) Electrode surface path with oxygen adsorption on the electrode surface, diffusion along the surface to the TPB, and reduction as well as incorporation of oxygen into YSZ at the TPB. (b) Electrolyte surface path with adsorption and diffusion on the electrolyte surface. The electron transfer occurs via the electrolyte. (c) Bulk path in case of a mixed ionic electronic conducting electrode with the elementary steps adsorption and charge transfer on the electrode surface, diffusion of oxide ions through the electrode bulk and oxygen incorporation along the entire electrode|electrolyte interface..... 3
- 2 Three possible locations of the electrochemically active zone of oxygen incorporation into YSZ: (a) Incorporation zone only extends along the free electrolyte surface. (b) Active zone sited beneath the platinum electrode (at the Pt|YSZ interface). (c) Situation combining the zones in (a) and (b). 9
- 3 (a) Optical micrograph of circular Pt thin film electrodes on a YSZ (100) single crystal. Nominal electrode sizes are (from top to bottom): 200, 100, 80, 50, 20, and 10 μm . The dark dots on the surface of the Pt electrodes were neither pores nor pinholes but bubbles which evolved during the annealing process (see also Figs. 14d and e). (b) 3D image of a 100 μm electrode measured by confocal microscopy; the height information is color-coded with blue indicating low and red indicating high values (note that the height axis is strongly exaggerated). The “spikes” in the image were bubbles. The red plane across the electrode indicates the cross section plane for height profiling – the corresponding height profile is given in (c)..... 15
- 4 (a) Sketch of the experimental setup for two-point impedance measurements. (b) View through the microscope with one 100 μm electrode being contacted. The spots on the other electrodes were caused by the contacting tip during earlier measurements..... 17
- 5 Sketch of the setup used for pseudo four-point impedance measurements. The notations of the connectors of the impedance analyzer CE, WE and RE denote counter electrode, working electrode and reference electrode, respectively. The meaning of capacitor $C_{\text{no_dc}}$ is explained throughout the text (Sec. 2.2.2)..... 18
- 6 Plot of the thermovoltage measured between a 100 μm microelectrode and the counter electrode versus the set temperature..... 19

-
- 7 Impedance spectra (Nyquist plot) measured on one single circular 200 μm Pt electrode (686 $^{\circ}\text{C}$). The numbers in brackets in the caption denote the chronological order of the respective measurement. (a) The dominating electrode feature is clearly affected by introducing the blocking capacitor $C_{\text{no_dc}}$ (which was 10 μF in this case): The measurements done without $C_{\text{no_dc}}$ yield a polarization resistance $\sim 20\%$ larger than the measurements done with the blocking capacitor. (Please note that the absolute values are not really comparable to the results in Sec. 4 since these test electrodes had quite different thermal history) (b) Magnification of the high frequency part of the spectrum exhibiting the same YSZ bulk resistance value for all measurements. 21
- 8 Current-voltage measurements obtained on the same electrode as the impedance spectra in Fig. 7 together with a fit curve (see Sec. 6.1). The voltage shift of the curve is caused by a thermovoltage (10 mV in this case). The red and the black arrow indicate the point of impedance measurements in equilibrium (with $C_{\text{no_dc}}$) and of short circuited impedance measurements (without $C_{\text{no_dc}}$), respectively. The difference in the slope at these two-points is about 20 %..... 21
- 9 (a) Sketch of the dc-measurement setup. The labels of the connectors on the potentiostat denote working electrode and counter electrode, respectively. (b) View through the microscope with a 100 μm microelectrode contacted by a tip (black wedge on the right hand side). 22
- 10 Measured current (left y-axis) and voltage (right y-axis) plotted as a function of time for a corrected temperature of 681 $^{\circ}\text{C}$. (a) Interval between the start of the experiment and a cathodic polarization of -0.9 V. The holding time at each set voltage was 200 s. (b) Magnification of three I-t characteristics (at three voltage set points) showing the typical relaxation characteristics of R-C elements (i.e. charging of the interfacial capacitance). The green boxes denote the current values, which were averaged to obtain I- η curves..... 23
- 11 Sketch of the setup used for ^{18}O incorporation experiments. The thickness of the YSZ was 0.5 mm; the total thickness of the samples (YSZ + counter electrode + sapphire) was in the range of 1 mm. 25
- 12 SEM images of high temperature deposited circular Pt thin film electrodes on YSZ. (a) Electrodes with varying diameters after preparation (48 h annealing at 700 $^{\circ}\text{C}$). Nominal diameters (from top to bottom): 200, 100, 80, 50, 20, and 10 μm – due to experimental reasons only the four upper rows were used in electrochemical measurements. (b) 100 μm electrode after measurements at temperatures up to 950 $^{\circ}\text{C}$; the pinholes evolved only at the highest temperature of 950 $^{\circ}\text{C}$, the damage in the center was caused by the contact tip. (c) Higher magnification of the platinum surface after electrode preparation; grain boundaries but no pores are visible. (d) Cross-section of an electrode (before electrochemical measurements) prepared by a focused ion beam.

	Cavities at the interface of Pt and YSZ are marked with arrows. The vertical grooves are artifacts due to preparation.	28
13	SEM images of the high temperature deposited Pt electrodes used in ^{18}O tracer experiments: (a) Rectangular shaped ($50 \times 100 \mu\text{m}^2$) electrodes. (b) Higher magnification of the surface of a Pt electrode in (a). Neither cracks nor pores but grain boundaries are visible.	29
14	(a) SEM image of the virgin low temperature sputter-deposited Pt film on YSZ (100). The average crystallite size was between 20 and 30 nm. (b) Pt film after a two hour heat treatment at $750 \text{ }^\circ\text{C}$. The crystallite size was increased but neither cracks nor pores were visible. (c) Pt film after electrochemical measurements. Further crystal growth and some surface roughening were obvious. (d) Lower magnification of a Pt film comparable to that in (c) indicating bubble formation. The bubbles persisted also during electrochemical experiments. (e) Higher magnification of one single bubble. (f) Collapsed bubble.	30
15	Diffraction patterns of Pt films/electrodes on a YSZ (100) substrate directly after high temperature sputtering and after annealing for 48 h at $700 \text{ }^\circ\text{C}$. Neglecting K_β reflexes almost only signals corresponding to Pt (111) and YSZ (100) orientation were detected. The blank measurement was performed on an identical YSZ single crystal without platinum electrodes.	31
16	(a) Diffraction pattern of the virgin low temperature deposited Pt thin film (without any thermal treatment) and the corresponding Rietveld refinement as well as the pattern of the YSZ blank (mirrored). (b) Diffraction pattern of the annealed Pt film together with its Rietveld refinement and the pattern of the blank YSZ (mirrored).	33
17	(a) Comparison of the measurements shown in Fig. 16. The reflexes corresponding to the Pt thin film are indicated by an asterisk. (b) Comparison of two simulated diffraction patterns: The simulation of an ideal Pt (111) diffraction pattern is shown by the upper orange graph, whereas the lower light blue graph depicts the simulated pattern of slightly inclined Pt (111).	34
18	(a) Impedance spectra (Nyquist plots) measured on $100 \mu\text{m}$ electrodes at five different set temperatures. The magnification below shows the high frequency part of the spectra and visualizes the axis intercept due to the electrolyte spreading resistance and a shoulder-like feature. (b) Comparison of the $700 \text{ }^\circ\text{C}$ spectrum from (a) with the fit result using the equivalent circuit in Fig. 19 (filled symbols).	36
19	Equivalent circuit used for the CNLS fits of impedance measurements between 700 and $900 \text{ }^\circ\text{C}$ on high temperature deposited Pt microelectrodes. The fit elements are explained throughout the text (cf. Sec. 4.1.3).	36

20	Arrhenius plot of the ionic conductivity of an YSZ (100) single crystal. The measurement was performed with “conventional” i.e. extended, symmetric Pt electrodes. The red line represents an Arrhenius fit of the linear region at high temperatures (denoted HT) and the blue line represents an Arrhenius fit of the linear region at low temperatures. The fit results ($E_{a,HT}$ and $\sigma_{o,HT}$ as well as $E_{a,LT}$ and $\sigma_{o,LT}$) are given within the figure and the activation energy values are in acceptable agreement with data from literature [97, 102].	38
21	Arrhenius plots of the resistor R_1 representing the rate determining step. In (a) the raw data is given as $1/R_1$ whereas in (b) and (c) TPB length and area-related data are plotted, respectively. Obviously in (b) all lines fall together and a specific electrode “conductivity” results.	41
22	Arrhenius plots of the resistor R_2 which corresponds to the high frequency shoulder in the Nyquist Plot. (a) Raw data, (b) TPB length related values, (c) area-related values; Contrary to R_1 (Fig. 21) the area-related lines fall together.	42
23	Inverse values of R_1 (representing the rate determining step) plotted versus the TPB length. The data points were calculated from the linear equations of the regression lines in Fig. 21a.	44
24	Arrhenius plots of the capacitance C_1 . (a) Raw data, (b) TPB length related values, (c) area-related values.	45
25	Arrhenius plots of parameter C_2 . (a) Raw data, (b) TPB length related values, (c) area-related values.	46
26	Comparison of three representative impedance spectra measured on 200 μm electrodes at three different temperatures (corrected values) with the results of the Kramers Kronig tests: (a) 615 $^\circ\text{C}$, (b) 510 $^\circ\text{C}$, (c) 424 $^\circ\text{C}$. On the right hand side of each impedance spectrum the respective residual plot is shown (cf. Eq. 20): (d) 615 $^\circ\text{C}$, (e) 510 $^\circ\text{C}$, (f) 424 $^\circ\text{C}$.	54
27	Equivalent circuit used for parameterization of impedance spectra measured at intermediate and low temperatures. R_{rds} represents the resistance of the rate determining step. The elements R_B and CPE_B were used to obtain satisfying fit results only.	55
28	Impedance spectra measured at different temperatures on 200 μm electrodes compared with the results of the CNLS fit using the equivalent circuit in Fig. 27. (a) Measured impedance data at 615 $^\circ\text{C}$ electrode temperature (open diamonds) compared to the fit result (solid green line). The fit was extrapolated to very low frequencies (dotted green line) to indicate the dc resistance at this temperature. (b) Comparison of the measured data (open diamonds) with the extrapolated fit result (dotted blue line) when using only a reduced frequency range of the spectrum in the CNLS-fit (red filled circles). (c) Magnification of the medium frequency part of the spectrum in (b) indicat-	

- ing the reduced fit range. (d) Low frequency part of the spectrum measured at 424 °C (open circles) as well as the fit result (solid orange line). The extrapolation of the fit is shown in (e) with the orange dotted line. 57
- 29 Capacitance C_A calculated by Eq. 10 from the constant phase element CPE_A , which in the equivalent circuit is in parallel to the resistance representing the rate determining step. Values were determined from the impedance data of 200 μm (black diamonds) and 50 μm electrodes (blue circles)..... 58
- 30 Arrhenius plot of the inverse polarization resistance representing the rate determining step. (a) Raw data of 200 μm (black squares) and 50 μm electrodes (blue triangles). Further the resulting fit curves using Eq. 21 are shown – 200 μm : solid black line; 50 μm : dashed blue line. (b) Fit results of 200 μm and 50 μm data related to the TPB length of the electrodes. Obviously at higher temperatures the steeper branches of the curves fall together. (c) Plot of area-related fit results; in this case the shallow branches fall together. 61
- 31 (a) Equivalent circuit describing two parallel resistive electrochemical processes (capacitive processes not shown). Resistor 1 represents the surface path with a rate determining step located close to the TPB. Resistor 2 symbolizes an area-related rate determining process of the pathway through the Pt electrode. (b) Equivalent circuit with two slow serial electrochemical processes (capacitances again neglected). (c) Expected Arrhenius diagram for the situations in (a) and (b) assuming different activation energies for the two processes..... 62
- 32 (a) Schematic illustration of two electrode processes potentially leading to a co-limited polarization resistance. (b) Equivalent circuit corresponding to the situation in (a) – capacitances were neglected. (c) Arrhenius diagram of the conductances of the two individual processes and the resulting co-limitation with the lateral diffusion process having a higher activation energy than the perpendicular reaction ($E_{a,lat} > E_{a,perp}$). (d) Resulting Arrhenius diagram with $E_{a,lat} < E_{a,perp}$ 63
- 33 (a) Possible reaction pathways assuming fast Pt surface diffusion and negligible oxygen reduction/incorporation on free YSZ. The gray dotted path along the Pt|YSZ interface would only be accessible in case of fast interface diffusion. (b) Reaction pathways in (a) with oxygen adsorption on Pt being the area-related rate limiting step and co-limitation of adsorption and surface diffusion on YSZ (with a short decay length) being the slowest TPB-related elementary step. (c) Situation with oxygen diffusion through Pt (along grain boundaries) being the area-related rate determining step in parallel to co-limitation of oxygen diffusion along the interface and charge transfer at the interface with a short decay length being the TPB-related rate limiting step. (d) Alternative to the situation in (c) with diffusion of an adsorbed oxygen species through an impurity phase as the TPB-related rate limiting process..... 65

34	Sketch of the possible reaction steps of oxygen adsorption on Pt (111) – cf. Ref. [112]: (a) Physisorbed molecular species. (b) Chemisorbed molecular species (e.g. superoxo or peroxy species). (c) Dissociatively chemisorbed oxygen.	66
35	Distribution images (intensity plots) obtained by ToF-SIMS showing impurities on the YSZ surface after removing the Pt thin film electrode in nitrohydrochloric acid. The electrode in the center was strongly polarized (overpotential $\eta = -2.22$ V at 303 °C for 10 min), the neighboring electrodes – above and below – were not polarized during the experiment. (a) Accumulation of Si at the TPB of the polarized electrode. (b) Calcium distribution on YSZ.....	71
36	Comparison of the Arrhenius curves from the present thesis with electrode “conductivities” from literature. The terms LT Pt and HT Pt denote low temperature deposited and high temperature deposited Pt electrodes, respectively.	73
37	Impedance spectra measured under equilibrium conditions (open symbols) compared to those measured under dc bias (closed symbols). The solid lines show fit results using two serial R-CPE elements as an equivalent circuit. (a) The size of the low frequency arc and thus the polarization resistance of O ₂ reduction strongly decreases with increasing bias. (b) High frequency part of the spectra in (a): the bias voltage has no effect on the YSZ bulk resistance at “lower” bias values. (c) In case of the highest polarization (-2.50 V) the bulk resistance shows a slight decrease which indicates an increase in electron concentration due to some reduction of YSZ.....	76
38	Time dependence of the dc current I_{dc} during incorporation experiments. (a) Current-time behavior of electrodes at polarizations where a significant YSZ reduction was not observed. The arrows indicate the point when ¹⁸ O incorporation was started. (b) Comparison of the curves in (a) with I_{dc} -t characteristics of the electrode with highest polarization. The increase in current during the first 50 seconds of polarization can be explained by reduction of YSZ.....	78
39	¹⁸ O distribution images (intensity plots) of differently polarized electrodes. The ¹⁸ O intensity is color-coded (see the vertical bar on the left – black: low intensity, white: high intensity); the size of each image is 200 × 200 μm ² . Images in the first line were recorded with the electrode still remaining on the YSZ (a-e), those in the second line were measured after removing the Pt thin film electrode (f-j).....	81
40	(a) Lateral ¹⁸ O distribution image (x-y-plane) of electrode 3b ($\eta = -2.17$ V) after removing the platinum electrode. (b) Tracer depth distribution in YSZ (x-z-plane) for the same electrode. Note the different scale of lateral (x/y) and depth directions (z) – the z-direction is strongly exaggerated. (c) ¹⁸ O depth profile (tracer concentration plotted versus depth; green line) compared to a lateral profile (blue line) obtained for electrode 3a.	84

-
- 41 (a) ^{18}O distribution image focusing on one corner of electrode 1 after removing the Pt thin film (image size $30 \times 30 \mu\text{m}^2$). The area inside the blue dotted box was used for determining the lateral profile. (b) Concentration plot calculated from the box in (a) showing the lateral distribution of ^{18}O along the Pt|YSZ interface and the free YSZ surface..... 85
- 42 (a) ^{18}O distribution image of one corner of electrode 3a with the Pt electrode still remaining on the YSZ single crystal and (b) after removing the Pt thin film (image sizes $30 \times 30 \mu\text{m}^2$ each). (c) Lateral distribution of ^{18}O (concentration plot) calculated from the areas inside the dotted boxes in (a): red and (b): blue. A shift of the peak position towards the region initially covered by Pt is obvious..... 85
- 43 (a) ^{18}O distribution image of one corner of electrode 4 with the Pt electrode still remaining on the YSZ single crystal and (b) after removing the Pt thin film (image sizes $30 \times 30 \mu\text{m}^2$ each). (c) Lateral distribution of ^{18}O (concentration plot) calculated from the areas inside the dotted boxes in (a): red and (b): blue. Peak positions are almost identical. Only the left shoulder of the peak was initially covered by the platinum electrode..... 86
- 44 (a) ^{18}O distribution image of one corner of electrode 5 with the Pt electrode still remaining on the YSZ single crystal and (b) after removing the Pt thin film (image sizes $30 \times 30 \mu\text{m}^2$ each). The rhomboid shape of the integration areas accounts for the slightly tilted position of the sample. (c) Lateral distribution of ^{18}O (concentration plot) calculated from the areas inside the dotted boxes in (a): red and (b): blue. Peak positions and shapes are virtually identical..... 86
- 45 (a) Distribution of ^{18}O in YSZ at electrode 3b ($\eta = -2.17 \text{ V}$, $T = 326 \text{ }^\circ\text{C}$). The green frame-shaped area reflects high intensities of ^{18}O close to the TPB (cf. Fig. 39h). The dotted boxes indicate different integration areas. (b) The integrated intensity was converted into a concentration (Eq. 43) and plotted versus the sputter depth (z -direction) to obtain depth profiles. The orange depth profile corresponds to the orange integration area in (a) whereas the dashed green depth profile of the TPB region corresponds to the difference of white minus orange integration area. 90
- 46 (a) ^{18}O distribution image of electrode 3a (cf. Fig. 39h) with the integration area for the calculation of the profile in (b) where the concentration (calculated by means of Eq. 43) is plotted versus the lateral position. (c) Equivalent circuit reflecting oxygen incorporation via two parallel paths i.e. two parallel resistive processes..... 91
- 47 (a) Current-overpotential curves measured on $100 \mu\text{m}$ electrodes at $639 \text{ }^\circ\text{C}$ (dark blue diamonds), $661 \text{ }^\circ\text{C}$ (light blue squares), and $681 \text{ }^\circ\text{C}$ (green triangles). The given temperatures represent corrected values (cf. Sec. 4.1.1) (b) Magnification of the less polarized part of the curves in (a). 94

48	(a) Current-overpotential curves measured on 100 μm electrodes at 701 $^{\circ}\text{C}$ (red circles), and 721 $^{\circ}\text{C}$ (orange crosses). The given temperatures represent corrected values (cf. Sec. 4.1.1) (b) Magnification of the less polarized part of the curves in (a).....	95
49	The 661 $^{\circ}\text{C}$ curve from 43 together with its fit curve according to Eq. 49. (a) Entire measured voltage range. (b) Diffusion dominated part at lower polarization.....	98
50	The 701 $^{\circ}\text{C}$ curve from Fig. 48 together with its fit curve according to Eq. 49. (a) Entire measured voltage range. (b) Diffusion dominated part at lower polarization.....	99
51	Fit parameters corresponding to the diffusion process (cf. Eq. 46). (a) Arrhenius plot of the limiting current I_{lim} (absolute values) including linear regression lines. Different symbols correspond to different electrodes. (b) Plot of z_{diff} values versus temperature.	101
52	Comparison of TPB length related inverse polarization resistances (obtained from the slopes of the fit curves – cf. Eq. 50) with results of impedance data from Sec. 4.1.2.1 (Fig. 21); the red line shows the Arrhenius fit of impedance measurements on 100 μm electrodes.....	102
53	Fit parameters corresponding to Eq. 47 for different electrodes. (a) Arrhenius plot of fit parameter I_0 . Taking the data of all electrodes into account the grey dashed fit line is obtained; the corresponding activation energy is 3.65 ± 0.36 eV (b) Plot of b values versus temperature; the average value of all data points was 1.05 ± 0.07 (gray dash-dotted line).	104
54	High frequency part of impedance spectra measured without an additional dc bias (open circles) and at -1.5 V bias (closed squares). The high frequency intercept is virtually the same indicating no noteworthy electronic current path within YSZ.....	106
55	Impedance spectrum (Nyquist plot) of a 100 μm electrode measured at 639 $^{\circ}\text{C}$ (real temperature). (a) Low frequency part of the spectrum showing the dominating arc. (b) High frequency part exhibiting a real axis intercept and a shoulder-like feature.	109
56	Sketch of the discussed parallel electrochemical pathways (capacitances are not shown): (a) Pt surface path with diffusion of oxygen through an impurity phase at the TPB being rate limiting. (b) Electrochemical oxygen reduction process on the free YSZ surface with electron supply via the electrolyte. (c) Capacitively blocked path via an interfacial “phase”.....	110
57	Bode plots of the measured impedance spectra in Fig. 55 (open circles) compared to the fits using two different equivalent circuits (depicted as inserts): (a) Equivalent circuit from Fig. 19. (b) Improved equivalent circuit considering diffusion limitation as discussed throughout the text.	112
58	Arrhenius plots for the two processes identified in dc experiments and extrapolated to lower temperatures. The orange continuous line reflects the diffusion limited Pt sur-	

- face path, whereas the gray dashed line represents the path with an exponential $I-\eta$ relation. All values correspond to circular electrodes with 100 μm in diameter. (a) Inverse polarization resistance at equilibrium conditions. (b) Current at -0.1 V overpotential. (c) Current at -0.5 V overpotential. (d) Current at -1.0 V overpotential. (e) Current at -1.5 V overpotential. (f) Current at -2.0 V overpotential. The blue cross indicates the current measured during ^{18}O incorporation at the "lowest" polarized electrode (electrode no. 1, $\eta = -1.99$ V) in Sec. 5.2.1..... 116
- 59 Different electrical pathways available for Pt electrodes on YSZ. Reaction pathways offering the possibility of a faradaic reaction are indicated by an arrowhead. (a) Pt surface path with diffusion through an impurity phase at the TPB being rate limiting. (b) Bulk path through the Pt electrode; most probably via diffusion of oxygen along Pt grain boundaries. (c) Electrolyte surface path with reduction of O_2 on the free YSZ surface which is most likely rate limited by electron supply via the electrolyte. (d) Reaction path via an oxygen containing "phase" at the Pt|YSZ interface which is capacitively blocked by the finite amount of oxygen stored in it. (e) Capacitive path via the interfacial double layer capacitor..... 118

11 List of Tables

1	Influence of temperature and time on the diffusion length of ^{18}O tracer in YSZ.	11
2	Crystallite sizes and Pt lattice parameters of sputtered and annealed platinum films.	32
3	Geometrical properties of the circular microelectrodes used.	40
4	Summary of the results deduced from the impedance measurements	47
5	Activation energies of the processes responsible for the rate determining step of the electrode reaction obtained by fitting the measured data in Fig. 30a using Eq. 21.	62
6	Sample temperatures calculated from the averaged YSZ spreading resistance (\bar{R}_{YSZ}).	75
7	Calculation of the cathodic overpotentials η from the applied voltage U_{set} by subtracting the voltage drop in the electrolyte (Eq. 42). The nominally identical η for set voltages of -2.25 and -2.50 V may be due to some measurement or fitting inaccuracies.	79
8	The width b of the electrochemically active zone of differently polarized electrodes: FWHM values $b_{\text{free YSZ}}$ and b_{tot} were determined from Figs. 41 – 44 with the electrode still remaining and after removal of the Pt electrode, respectively. The corrected values ($b_{\text{eff}} = b_{\text{tot}} - 2 \cdot L_{\text{diff}}$) were obtained after subtraction of the contribution caused by diffusion. In case of electrode 5 the TPB width determined from the FWHM is not comparable to the others, since the shape of the lateral profile is more complex.....	88
9	Comparison of amounts of tracer incorporated via the surface (TPB) or the bulk path (Pt YSZ interface) of the Pt thin film electrodes.	92
10	Comparison of CNLS-fit results obtained from fits of the spectrum in Fig. 55 with two different equivalent circuits. The Bode plots of both fits are shown in Fig. 57.....	113

12 References

- 1 C. H. Hamann & W. Vielstich. *Electrochemistry*. 3rd edn, (Wiley-VCH, 1998).
- 2 J. Riegel, H. Neumann & H. M. Wiedenmann. *Solid State Ionics* **152-153** (2002), p.783-800.
- 3 E. Ivers-Tiffée, K. H. Härdtl, W. Menesklou & J. Riegel. *Electrochim. Acta* **47** (2001), p.807-814.
- 4 S. B. Adler. *Chem. Rev.* **104** (2004), p.4791-4844.
- 5 N. Q. Minh. *J. Am. Ceram. Soc.* **76** (1993), p.563-588.
- 6 N. Q. Minh. *Solid State Ionics (Solid State Ionics Dokiya Memorial Special Issue)* **174** (2004), p.271-277.
- 7 H. Huang, M. Nakamura, P. Su, R. Fasching, Y. Saito & F. B. Prinz. *J. Electrochem. Soc.* **154** (2007), p.B20-B24.
- 8 A. Evans, A. Bieberle-Hutter, L. J. Bonderer, P. Chen, D. Hodel, J. L. Rupp & L. J. Gauckler. *ECS Transactions* **25** (2009), p.989-993.
- 9 C. G. Vayenas, S. Bebelis & S. Ladas. *Nature* **343** (1990), p.625-627.
- 10 C. G. Vayenas, S. Bebelis, V. Yentekakis, P. Tsiakaras & H. Karasali. *Platinum Metals Review* **34** (1990), p.122-130.
- 11 N. Kotsionopoulos & S. Bebelis. *Journal of Applied Electrochemistry* **35** (2005), p.1253-1264.
- 12 C. Falgoutte & G. Fóti. *Catalysis Today* **146** (2009), p.274-278.
- 13 A. Damjanovic, M. A. Genshaw & J. O. M. Bockris. *J. Electrochem. Soc.* **114** (1967), p.1107-1112.
- 14 J. O. M. Bockris & R. Abdu. *Journal of Electroanalytical Chemistry* **448** (1998), p.189-204.
- 15 S. Strbac. *Electrochim. Acta* **56** (2011), p.1597-1604.
- 16 R. Adzic. in *Electrocatalysis, Frontiers of Electrochemistry* (Wiley-Vch, Inc, 1998) p. 197-242.
- 17 N. Markovic, H. Gasteiger & P. N. Ross. *J. Electrochem. Soc.* **144** (1997), p.1591-1597.
- 18 J. Fleig. *Annual Review of Materials Research* **33** (2003), p.361-382.
- 19 J. Janek, B. Luerßen, E. Mutoro, H. Fischer & S. Günther. *Topics in Catalysis* **44** (2007), p.399-407.
- 20 L. R. Velho & R. W. Bartlett. *Metallurgical Transactions* **3** (1972), p.65-&.
- 21 G. Beck, H. Fischer, E. Mutoro, V. Srot, K. Petrikowski, E. Tchernychova, M. Wuttig, M. Ruhle, B. Luerßen & J. Janek. *Solid State Ionics* **178** (2007), p.327-337.
- 22 R. Radhakrishnan, A. V. Virkar & S. C. Singhal. *J. Electrochem. Soc.* **152** (2005), p.A927-A936.
- 23 J. Van Herle & A. J. McEvoy. *Journal of Physics and Chemistry of Solids* **55** (1994), p.339-347.

- 24 V. Brichzin, J. Fleig, H.-U. Habermeier, G. Cristiani & J. Maier. *Solid State Ionics* **152-153** (2002), p.499-507.
- 25 B. A. Boukamp. *Solid State Ionics* **136-137** (2000), p.75-82.
- 26 W. C. Chueh, W. Lai & S. M. Haile. *Solid State Ionics* **179** (2008), p.1036-1041.
- 27 J. Jamnik & J. Maier. *Phys. Chem. Chem. Phys.* **3** (2001), p.1668-1678.
- 28 J. Jamnik. *Solid State Ionics* **157** (2003), p.19-28.
- 29 L. Wang, R. Merkle & J. Maier. *J. Electrochem. Soc.* **157** (2010), p.B1802-B1808.
- 30 F. S. Baumann. *Oxygen reduction kinetics on mixed conducting SOFC model cathodes* Dissertation thesis, Fakultät für Chemie der Universität Stuttgart, (2006).
- 31 F. S. Baumann, J. Fleig, H. U. Habermeier & J. Maier. *Solid State Ionics* **177** (2006), p.1071-1081.
- 32 J. Januschewsky, M. Ahrens, A. Opitz, F. Kubel & J. Fleig. *Advanced Functional Materials* **19** (2009).
- 33 R. Schmiedl, V. Demuth, P. Lahnor, H. Godehardt, Y. Bodschwinn, C. Harder, L. Hammer, H. P. Strunk, M. Schulz & K. Heinz. *Applied Physics a-Materials Science & Processing* **62** (1996), p.223-230.
- 34 K. Sreenivas, I. Reaney, T. Maeder, N. Setter, C. Jagadish & R. G. Elliman. *Journal of Applied Physics* **75** (1994), p.232-239.
- 35 R. Stumpf, C.-L. Liu & C. Tracy. *Applied Physics Letters* **75** (1999), p.1389-1391.
- 36 T. Ryll, H. Galinski, L. Schlagenhauf, P. Elser, J. L. M. Rupp, A. Bieberle-Hutter & L. J. Gauckler. *Advanced Functional Materials* **21** (2011), p.565-572.
- 37 T. Horita, K. Yamaji, N. Sakai, H. Yokokawa, T. Kawada & T. Kato. *Solid State Ionics* **127** (2000), p.55-65.
- 38 R. Radhakrishnan, A. V. Virkar & S. C. Singhal. *J. Electrochem. Soc.* **152** (2005), p.A210-A218.
- 39 W. H. Nernst. *Zeitschrift für Elektrochemie* **6** (1899), p.41-43.
- 40 T. Jacobsen & L. Bay. *Electrochim. Acta* **47** (2002), p.2177-2181.
- 41 R. Baker, J. Guindet & M. Kleitz. *J. Electrochem. Soc.* **144** (1997), p.2427-2432.
- 42 M. W. Breiter, K. Leeb & G. Fafilek. *Journal of Electroanalytical Chemistry* **434** (1997), p.129-137.
- 43 A. Mitterdorfer & L. J. Gauckler. *Solid State Ionics* **117** (1999), p.187-202.
- 44 T. Kawada, T. Horita, N. Sakai, H. Yokokawa, M. Dokiya & J. Mizusaki. *Solid State Ionics* **131** (2000), p.199-210.
- 45 H. Kishimoto, N. Sakai, K. Yamaji, T. Horita, M. E. Brito, H. Yokokawa, K. Amezawa & Y. Uchimoto. *Solid State Ionics* **179** (2008), p.347-354.
- 46 J. L. Hertz & H. L. Tuller. *J. Electrochem. Soc.* **154** (2007), p.B413-B418.
- 47 M. J. Verkerk & A. J. Burggraaf. *J. Electrochem. Soc.* **130** (1983), p.78-84.
- 48 D. Y. Wang & A. S. Nowick. *J. Electrochem. Soc.* **126** (1979), p.1166-1172.
- 49 E. Mutoro, S. Günther, B. Luerßen, I. Valov & J. Janek. *Solid State Ionics* **179** (2008), p.1835-1848.
- 50 J. Hertz, A. Rothschild & H. Tuller. *J. Electroceram.* **22** (2009), p.428-435.

- 51 S. Koc, G. J. la O', T. Golfinopoulos & Y. Shao-Horn. *ECS Transactions* **7** (2007), p.1271-1277.
- 52 J. Mizusaki, K. Amano, S. Yamauchi & K. Fueki. *Solid State Ionics* **22** (1987), p.313-322.
- 53 J. Mizusaki, K. Amano, S. Yamauchi & K. Fueki. *Solid State Ionics* **22** (1987), p.323-330.
- 54 E. Mutoro, B. Luerssen, S. Günther & J. Janek. *Solid State Ionics* **179** (2008), p.1214-1218.
- 55 G. Fóti, A. Jaccoud, C. Falgairrette & C. Comninellis. *J. Electroceram.* **23** (2009), p.175-179.
- 56 J. Nielsen & T. Jacobsen. *Solid State Ionics* **178** (2007), p.1001-1009.
- 57 S. N. Shkerin. *Russian Journal of Electrochemistry* **39** (2003), p.863-866.
- 58 J. Van Herle, A. J. McEvoy & K. Ravindranathan Thampi. *Electrochim. Acta* **39** (1994), p.1675-1680.
- 59 M. J. Verkerk, M. W. J. Hammink & A. J. Burggraaf. *J. Electrochem. Soc.* **130** (1983), p.70-78.
- 60 K. Sasaki, J. Tamura & M. Dokiya. *Solid State Ionics* **144** (2001), p.223-232.
- 61 D. Y. Wang & A. S. Nowick. *J. Electrochem. Soc.* **126** (1979), p.1155-1165.
- 62 J. L. Hertz & H. L. Tuller. *Solid State Ionics* **178** (2007), p.915-923.
- 63 A. Jaccoud, C. Falgairrette, G. Fóti & C. Comninellis. *Electrochim. Acta* **52** (2007), p.7927-7935.
- 64 B. K. Lee, Y. H. Yu, B. S. So, S. M. Kim, J. Kim, H. W. Lee, J. H. Lee & J. H. Hwang. *J. Electroceram.* **17** (2006), p.735-739.
- 65 B. Luerßen, J. Janek & R. Imbihl. *Solid State Ionics* **141** (2001), p.701-707.
- 66 B. Luerßen, E. Mutoro, H. Fischer, S. Günther, R. Imbihl & J. Janek. *Angewandte Chemie International Edition* **45** (2006), p.1473-1476.
- 67 V. Stancovski, S. Sridhar & U. B. Pal. *J. Electroceram.* **3** (1999), p.279-299.
- 68 S. P. Yoon, S. W. Nam, S.-G. Kim, S.-A. Hong & S.-H. Hyun. *Journal of Power Sources* **115** (2003), p.27-34.
- 69 B. Zachau-Christiansen, T. Jacobsen, L. Bay & S. Skaarup. *Solid State Ionics* **113** (1998), p.271-277.
- 70 N. L. Robertson & J. N. Michaels. *J. Electrochem. Soc.* **137** (1990), p.129-135.
- 71 A. Mitterdorfer & L. J. Gauckler. *Solid State Ionics* **120** (1999), p.211-225.
- 72 C. Schwandt & W. Weppner. *J. Electrochem. Soc.* **144** (1997), p.3728-3738.
- 73 T. Kenjo & N. Shiroichi. *Electrochim. Acta* **42** (1997), p.3461-3470.
- 74 J. Fleig. *Solid State Ionics* **161** (2003), p.279-289.
- 75 J. Fleig, F. S. Baumann, V. Brichzin, H.-R. Kim, J. Jamnik, G. Cristiani, H.-U. Habermeier & J. Maier. *Fuel Cells* **6** (2006), p.284-292.
- 76 B. Luerßen, E. Mutoro, H. Fischer, S. Günther, R. Imbihl & J. Janek. *Angewandte Chemie* **118** (2006), p.1501-1504.
- 77 J. Fleig, F. Noll & J. Maier. *Berichte der Bunsengesellschaft/Physical Chemistry Chemical Physics* **100** (1996), p.607-615.
- 78 A. Bieberle, L. P. Meier & L. J. Gauckler. *J. Electrochem. Soc.* **148** (2001), p.A646-A656.

- 79 Y. B. Kim, C.-M. Hsu, S. T. Connor, T. M. Gur, Y. Cui & F. B. Prinz. *J. Electrochem. Soc.* **157** (2010), p.B1269-B1274.
- 80 W. G. Bessler, M. Vogler, H. Stormer, D. Gerthsen, A. Utz, A. Weber & E. Ivers-Tiffée. *Phys. Chem. Chem. Phys.* (2010).
- 81 A. Mitterdorfer & L. J. Gauckler. *Solid State Ionics* **117** (1999), p.203-217.
- 82 D. Kek, N. Bonanos, M. Mogensen & S. Pejovnik. *Solid State Ionics* **131** (2000), p.249-259.
- 83 J. Fleig. *Journal of Power Sources* **105** (2002), p.228-238.
- 84 J. Fleig. *Zeitschrift Fur Physikalische Chemie-International Journal of Research in Physical Chemistry & Chemical Physics* **221** (2007), p.1149-1159.
- 85 T. Horita, K. Yamaji, N. Sakai, H. Yokokawa & T. Kato. *J. Electrochem. Soc.* **148** (2001), p.J25-J30.
- 86 T. Horita, K. Yamaji, N. Sakai, Y. Xiong, T. Kato, H. Yokokawa & T. Kawada. *Journal of Power Sources* **106** (2002), p.224-230.
- 87 J. Fleig. *Phys. Chem. Chem. Phys.* **11** (2009), p.3144-3151.
- 88 J. Fleig, A. Schintlmeister, A. Opitz & H. Hutter. *Scripta Materialia* **65** (2011), p.78-83.
- 89 J. Maier. *Physical Chemistry of Ionic Materials - Ions and Electrons in Solids*. (John Wiley & Sons, Ltd, 2004).
- 90 H. Mehrer. *Diffusion in Solids*. (Springer, 2007).
- 91 E. Ahlgren & F. Willy Poulsen. *Solid State Ionics* **70-71** (1994), p.528-532.
- 92 V. Brichzin. *Sauerstoffreduktionskinetik in Hochtemperaturbrennstoffzellen mit Mikroelektroden* Ph.D. thesis, Universität Stuttgart, (2002).
- 93 K. V. Jensen, R. Wallenberg, I. Chorkendorff & M. Mogensen. *Solid State Ionics* **160** (2003), p.27-37.
- 94 T. Jacobsen, K. V. Hansen & E. Skou. *J. Electrochem. Soc.* **152** (2005), p.A2203-A2206.
- 95 E. Mutoro, B. Luerßen, S. Günther & J. Janek. *Solid State Ionics* **180** (2009), p.1019-1033.
- 96 T. Stephan, J. Zehnpfenning & A. Benninghoven. *Journal of Vacuum Science & Technology a - Vacuum Surfaces and Films* **12** (1994), p.405-410.
- 97 J. H. Park & R. N. Blumenthal. *J. Electrochem. Soc.* **136** (1989), p.2867-2876.
- 98 P. Ramminger. *Structural high temperature investigations of nanocrystalline chromium-oxynitride thin films* PhD thesis, Vienna University of Technology, (2003).
- 99 F. L. Jones. in *The Physics of Electrical Contacts*, (Clarendon Press, 1957) p. 15.
- 100 R. Holm. *Electric Contacts Handbook*. 3rd edn, (Springer-Verlag, 1958).
- 101 J. Newman. *J. Electrochem. Soc.* **113** (1966), p.501-502.
- 102 X. Guo & R. Waser. *Progress in Materials Science* **51** (2006), p.151-210.
- 103 J. Fleig. *Solid State Ionics* **150** (2002), p.181-193.
- 104 M. Mogensen, K. V. Jensen, M. J. Jørgensen & S. Primdahl. *Solid State Ionics* **150** (2002), p.123-129.
- 105 M. de Ridder, R. G. van Welzenis, H. H. Brongersma & U. Kreissig. *Solid State Ionics* **158** (2003), p.67-77.

- 106 M. de Ridder, A. G. J. Vervoort, R. G. van Welzenis & H. H. Brongersma. *Solid State Ionics* **156** (2003), p.255-262.
- 107 M. Hendriks, J. E. ten Elshof, H. J. M. Bouwmeester & H. Verweij. *Solid State Ionics* **146** (2002), p.211-217.
- 108 M. Hendriks, J. E. ten Elshof, H. J. M. Bouwmeester & H. Verweij. *Solid State Ionics* **154** (2002), p.467-472.
- 109 J. R. Macdonald. *Impedance Spectroscopy*. (John Wiley & Sons, 1987).
- 110 B. A. Boukamp. *J. Electrochem. Soc.* **142** (1995), p.1885-1894.
- 111 B. A. Boukamp. *Solid State Ionics* **169** (2004), p.65-73.
- 112 C. T. Rettner & C. B. Mullins. *The Journal of Chemical Physics* **94** (1991), p.1626-1635.
- 113 A. C. Luntz, M. D. Williams & D. S. Bethune. *J.Chem.Phys.* **89** (1988), p.4381-4395.
- 114 J. L. Gland & V. N. Korchak. *Surface Science* **75** (1978), p.733-750.
- 115 P. D. Nolan, B. R. Lutz, P. L. Tanaka, J. E. Davis & C. B. Mullins. *The Journal of Chemical Physics* **111** (1999), p.3696-3704.
- 116 P. W. Atkins. *Physikalische Chemie*. 3. edn, (Wiley-VCH, 2001).
- 117 E. Mutoro, N. Baumann & J. Janek. *The Journal of Physical Chemistry Letters* (2010), p.2322-2326.
- 118 J. Fleig, B. Rahmati, S. Rodewald & J. Maier. *Journal of the European Ceramic Society* **30** (2010), p.215-220.
- 119 J. Janek & C. Korte. *Solid State Ionics* **116** (1999), p.181-195.
- 120 B. Hagenhoff. *Microchimica Acta* **132** (2000), p.259-271.
- 121 R. A. De Souza, J. Zehnpfenning, M. Martin & J. Maier. *Solid State Ionics* **176** (2005), p.1465-1471.
- 122 I. Sakaguchi & H. Haneda. *Journal of Solid State Chemistry* **124** (1996), p.195-197.
- 123 R. A. De Souza & M. Martin. *Phys. Chem. Chem. Phys.* **10** (2008), p.2356-2367.
- 124 J. Maier. in *Physical Chemistry of Ionic Materials - Ions and Electrons in Solids*, Ch. 7.3.4.b, (John Wiley & Sons, Ltd, 2004) p. 454-457.
- 125 L. Heyne, N. M. Beekman & E. N. Philips Research Labs. *Proceedings of the British Ceramic Society* **19** (1971), p.229.
- 126 J. Fleig. *Phys. Chem. Chem. Phys.* **7** (2005), p.2027-2037.
- 127 J. R. Macdonald. in *Impedance Spectroscopy*, (John Wiley & Sons, 1987) p. 88.
- 128 J. Jamnik & J. Maier. *J. Electrochem. Soc.* **146** (1999), p.4183-4188.
- 129 W. Haas. *Der Knochenmann*. (Rowohlt, 1997).